Modeling and characterization of materials and nanostructures for photovoltaic application

Zuzana Mrazkova

université PARIS-SACLAY

NNT : 2017SACLX121

Thèse de doctorat

Modélisation et caractérisation de matériaux et nanostructures pour les applications photovoltaïques

Thèse de doctorat de VŠB - Technical University of Ostrava
et de l'Université Paris-Saclay, préparée à l'Ecole Polytechnique

Ecole doctorale n°573 Interfaces : approches interdisciplinaires, fondements, applications et innovation (Interfaces)
Spécialité de doctorat : Physique

Thèse présentée et soutenue à Ostrava, le 24 Novembre 2017, par

MME. ZUZANA MRAZKOVA

Composition du Jury :

Jaromír Pištora Professeur, VŠB - Technical University of Ostrava, Czech Republic	Président
Kurt Hingerl Professeur, Johannes Kepler Universität Linz, Austria	Rapporteur
Morten Kildemo Professeur, Norwegian University of Science and Technology, Norway	Rapporteur
Janez Krč Professeur, University of Ljubljana, Slovenia	Rapporteur
Jean-Paul Kleider Professeur, Université Paris-Saclay, France	Examinateur
Pere Roca i Cabarrocas Professeur, Université Paris-Saclay, France	Directeur de thèse
Kamil Postava Professeur associé, VŠB - Technical University of Ostrava, Czech Republic	Directeur de thèse
Martin Foldyna Chargé de Recherche, Université Paris-Saclay, France	Co-directeur de thèse

École Polytechnique, Université Paris-Saclay
Laboratoire de Physique des Interfaces et des Couches Minces

and

VŠB - Technical University of Ostrava
University Study Programmes
Nanotechnology Centre

Modeling and characterization of materials and nanostructures for photovoltaic applications

Thesis

Author: Ing. Zuzana Mrázková
Supervisor in France: Prof. Dr. Pere Roca i Cabarrocas
Co-supervisor in France: Ing. Martin Foldyna, Ph.D.
Supervisor in Czech Republic: Doc. Dr. Mgr. Kamil Postava

2017 Ostrava

I declare I elaborated this thesis by myself. All literary sources and publications I have used had been cited.

Acknowledgements

I have done my PhD study in a frame of a student sharing programme "co-tutelle" in collaboration between two laboratories: Nanotechnology Centre at VŠB-Technical University of Ostrava in Czech Republic and Laboratoire de Physique des Interfaces et des Couches Minces, CNRS, École Polytechnique, Université Paris-Saclay in France. During this exceptional four-year period of my life I have met many kind colleagues and friends both in Czech Republic and in France. I would like to thank to each of you for all experiences we have shared. Each one has been important for me, nevertheless it was in the lab or office, during group meetings, coffe-breaks or lunch times...

I thank to directors of both involved laboratories, Jaromír Pištora and Pere Roca i Cabarrocas, who have enabled me to work in their labs, provided me financial support from projects and grants, and helped me to at least draw with if not directly to beat the bureaucracy.

I thank to supervisors of my thesis, Kamil, Pere, and Martin, for your guidance, advices and support. I have learned a lot of things of you. I appreciate your help with the scientific stuff and also with solving non-scientific issues. I am grateful for financial support from your projects as well as for the administration of my join PhD study which has required a lot of paperwork. Thank you for guiding me through the exciting world of science.

Many thanks to my friends and colleagues who prepared samples for me and helped me with measurements. Thank you Igor, Soumyadeep, Mutaz, Letian, Jian, Ileana, Jean-Luc, and Ronan.

Tibor, Lukáš, Radek, Ondra, and Robin, thank you for being my friends to a disaster, for providing me an IT support and for having patience with my never-ending questions.

Many thanks to all my friends and colleagues from PVSiXT, Nanowire Team, and RP4 Supercomputing for Nanotechnologies research groups for being my friends and colleagues.

Especially thanks to my family and to my Martin for supporting me, rejoicing my successes and comforting me when things go wrong. Thank for always being here for me.

Résumé

La recherche sur le photovoltaïque vise à réduire le prix par watt de puissance électrique générée. Des efforts considérables sont menés pour rechercher de nouveaux matériaux et des conceptions qui repoussent les limites des cellules solaires existantes. Le développement récent de matériaux et nanostructures complexes pour les cellules solaires nécessite des efforts plus importants pour mener à bien leur caractérisation et leur modélisation. Cette thèse porte sur la caractérisation optique, la modélisation et l'optimisation de la conception d'architectures de cellules solaires de pointe.

La texturation des surfaces des cellules solaires est souvent utilisée pour améliorer le piégeage de la lumière, et donc améliorer le rendement de conversion. Les textures pyramidales sont les plus utilisés pour le silicium cristallin, en raison de leur faible coût et leur facilité de fabrication. Leurs propriétés de piégeage de la lumière sont également bien documentées. Une autre approche pour améliorer l'absorption lumineuse et augmenter le rendement de conversion est d'incorporer des nanostructures dans la conception des cellules. Les cellules solaires à base de jonction radiale de nanofils de silicium donnent une nouvelle perspective pour les devices à couches minces nanostructurés, grâce à un piégeage de la lumière amélioré et le découplage entre la direction d'absorption de la lumière et celle dans laquelle les porteurs de charges sont collectés.

L'objectif de cette thèse est la caractérisation optique, la modélisation, et l'optimisation des structures des cellules solaires fabriquées au Laboratoire de Physique des Interfaces et des Couches Minces (LPICM). Cela inclut des études sur des cellules solaires fabriqués sur des wafers à texture pyramidale et sur des cellules solaires à jonction radiale de nanofils de silicium orientés aléatoirement. Nous démontrerons que les méthodes optiques sont bénéfiques pour la caractérisation à la fois des textures pyramidales, et des nanofils de silicium.

Les mesures optiques sont utilisées pour la caractérisation rapide et non destructive des échantillons texturés pour les applications photovoltaïques. Les textures de surface améliorent le piégeage de la lumière et sont donc souhaitées pour améliorer les performances des cellules solaires. D'autre part, ces textures rendent la caractérisation optique plus difficile et des efforts plus importants sont nécessaires non seulement pour la mesure optique elle-même mais également pour la modélisation et l'interprétation ultérieure des données obtenues. Dans ce travail, nous démontrons que nous sommes en mesure d'utiliser des méthodes optiques pour étudier les textures pyramidales très répandues ainsi que les réseaux de nanofils de silicium à orientation aléatoire dont l'analyse est très difficile.

Premièrement, nous nous sommes concentrés sur l'étude optique de diverses surfaces pyramidales et de leur impact sur les performances des cellules silicium à hétérojonction. Nous avons constaté que les angles au sommet des pyramides,

préparées à l'aide de différentes conditions de texturation, diffèrent de la valeur théorique de $70.52°$ attendue pour le silicium cristallin. Cette modification de l'angle au sommet est expliquée par la présence, sur les facettes pyramidales, de terrasses monoatomiques régulières, observées par microscopie électronique à transmission de résolution atomique. L'impact d'une variation de l'angle au sommet sur les épaisseurs des couches minces déposées est étudié et les conséquences sur l'efficacité des cellules solaires résultantes sont discutées. Un modèle optique développé pour le calcul de la réflectance et de l'absorption des couches minces en multicouches sur surfaces pyramidales a permis l'optimisation de la conception de la cellule solaire pour un angle au sommet pyramidal donné.

L'ellipsométrie matricielle Mueller a été utilisée in-situ pour caractériser les six premières minutes du processus de croissance - par méthode vapeur-liquide-solide activée par plasma - des nanofils de silicium. Les fonctions optiques du ZnO et de Sn ont été déterminées à partir de mesures optiques et de modèles des échantillons de référence. Nous avons développé un modèle optique facile à utiliser de la croissance sur des couches minces de ZnO de 1 μm d'épaisseur déposée sur du verre Corning, qui, à notre connaissance, est le premier modèle utilisant des données ellipsométriques expérimentales pour contrôler le procédé de croissance, en phase vapeur-liquide-solide assisté par plasma, des nanofils. La dépendance linéaire observée du dépôt de matériau de silicium avec le temps de dépôt nous permet de suivre le processus de fabrication in situ et de contrôler la qualité du matériau.

Mots clés: propriétés optiques ; ellipsométrie spectroscopique ; polarimétrie matricielle Mueller in-situ ; modèles optiques multicouches ; cellules solaires silicium à hétérojonction ; textures pyramidales ; nanofils de silicium ; cellules solaires à jonction radiale

Abstract

Research in photovoltaics aims at lowering the price per watt of generated electrical power. Substantial efforts aim at searching for new materials and designs which can push the limits of existing solar cells. The recent development of complex materials and nanostructures for solar cells requires more effort to be put into their characterization and modeling. This thesis focuses on optical characterization, modeling, and design optimization of advanced solar cell architectures.

Optical measurements are used for fast and non-destructive characterization of textured samples for photovoltaic applications. Surface textures enhance light-trapping and are thus desired to improve the solar cell performance. On the other hand, these textures make optical characterization more challenging and more effort is required for both, the optical measurement itself and subsequent modeling and interpretation of obtained data. In this work, we demonstrate that we are able to use optical methods to study the widely used pyramidal textures as well as very challenging randomly oriented silicon nanowire arrays.

At first, we focused on the optical study of various pyramidal surfaces and their impact on the silicon heterojunction solar cell performance. We have found that vertex angles of pyramids prepared using various texturing conditions vary from the theoretical value of $70.52°$ expected from crystalline silicon. This change of the vertex angle is explained by regular monoatomic terraces, which are present on pyramid facets and are observed by atomic resolution transmission electron microscopy. The impact of a vertex angle variation on the thicknesses of deposited thin films is studied and the consequences for resulting solar cell efficiency are discussed. A developed optical model for calculation of the reflectance and absorptance of thin film multi-layers on pyramidal surfaces enabled a solar cell design optimization, with respect to a given pyramid vertex angle.

In-situ Mueller matrix ellipsometry has been applied for monitoring the silicon nanowire growth process by plasma-enhanced vapor-liquid-solid method. We have developed an easy-to-use optical model, which is to our knowledge a first model fitting the experimental ellipsometric data for process control of plasma-assisted vapor-liquid-solid grown nanowires. The observed linear dependence of the silicon material deposition on the deposition time enables us to trace the fabrication process in-situ and to control material quality.

Keywords: optical properties; spectroscopic ellipsometry; in-situ Mueller matrix polarimetry; multi-layer optical models; silicon heterojunction solar cells; pyramidal texture; silicon nanowires; radial junction solar cells

Abstrakt

Cílem výzkumu v oblasti fotovoltaiky je snížit cenu za watt vyrobené elektrické energie. Značné úsilí se věnuje hledání nových materiálů a struktur, které umožní posunout hranice stávajících solárních článků. Neustálý pokrok ve vývoji materiálů a nanostruktur pro solární články zvyšuje nároky také na jejich charakterizaci a modelování. Tato práce se zaměřuje na optickou charakterizaci, modelování a optimalizaci návrhů pokročilých struktur solárních článků.

Optické metody jsou vhodné k rychlé a nedestruktivní charakterizaci texturovaných vzorků pro fotovoltaické aplikace. Povrchové textury, které umožňují lepší zachycení světla a jsou proto žádoucí pro zlepšení účinnosti solárních článků, bohužel znesnadňují optickou charakterizaci. Je tedy zapotřebí většího úsilí jak pro realizaci samotných optických měření, tak pro následné modelování a interpretaci získaných dat. V této práci demonstrujeme, že jsme schopni použít optické metody ke studiu široce používaných pyramidálních textur, tak i méně obvyklých, na charakterizaci náročných, náhodně orientovaných křemíkových nanodrátků.

Nejprve jsme se zaměřili na optické studium různých pyramidálních povrchových textur a jejich vlivu na účinnost solárních článků s křemíkovým heteropřechodem. Zjistili jsme, že vrcholové úhly pyramid připravených různými texturovacími procesy se liší od teoretické hodnoty $70.52°$ vycházející z krystalografie křemíku. Tuto změnu vrcholového úhlu vysvětlujeme přítomností pravidelných monoatomických teras na stěnách pyramid, které jsme pozorovali pomocí transmisní elektronové mikroskopie s atomovou rozlišovací schopností. Provedli jsme studii vlivu změny vrcholového úhlu na tloušťky nanesených tenkých vrstev a diskutovali jsme možné důsledky pro výslednou účinnost solárních článků. Vyvinuli jsme optický model pro výpočet odrazivosti a absorpce tenkovrstevných systémů na pyramidách, jenž nám umožnil optimalizaci vrstev na povrchu solárních článků s ohledem na vrcholový úhel daných pyramid.

In-situ elipsometrie Muellerovy matice byla použita pro sledování růstu křemíkových nanodrátků metodou plasma-assisted vapor-liquid-solid. Vyvinuli jsme snadno použitelný optický model, který je, pokud víme, prvním modelem pro analýzu ellipsometrických dat měřených přímo v reaktoru během růstu náhodně orientovaných křemíkových nanodrátků. Pozorovaná lineární závislost depozice křemíku na čase nám umožňuje in-situ monitorování výrobního procesu a kontrolu kvality materiálu.

Klíčová slova: optické vlastnosti; spektrální elipsometrie, in-situ polarimetrie Muellerovy matice; multivrstevné optické modely; solární články s křemíkovým heteropřechodem; pyramidální textury; křemíkové nanodrátky; solární články s radiálním polovodičovým přechodem

Contents

List of symbols

AR	Anti-Reflective, Anti-Reflection
AR-MMP	Angle-Resolved Mueller Matrix Polarimetry
B-EMA	Bruggeman Effective Medium Approximation
CVD	Chemical Vapor Deposition
FTO	Fluorine-doped Tin Oxide
IPA	Isopropyl Alcohol
ITO	Indium Tin Oxide
JV	current density-voltage
LPICM	Laboratoire de Physique des Interfaces et des Couches Minces
NIR	Near-Infrared
NW	Nanowire
PECVD	Plasma-Enhanced Chemical Vapor Deposition
PV	Photovoltaic
SE	Spectroscopic Ellipsometry
SEM	Scanning Electron Microscopy
SHJ	Silicon Heterojunction
SiNW	Silicon Nanowire
STEM-BF	Scanning Transmission Electron Microscopy in Bright-Field
STEM-HAADF	Scanning Transmission Electron Microscopy in High-Angle Annular Dark-Field
TCO	Transparent Conducting Oxide
TEM	Transmission Electron Microscopy
TMB	Trimethylboron
UV	Ultraviolet
Vis	Visible
VLS	Vapor-Liquid-Solid method

a-Si:H	hydrogenated amorphous silicon
a-SiC:H	hydrogenated amorphous silicon carbide
(i)a-Si:H	intrinsic hydrogenated amorphous silicon
(i)a-SiC:H	intrinsic hydrogenated amorphous silicon carbide
(n+)a-Si:H	n-type hydrogenated amorphous silicon
(p)a-Si:H	p-type hydrogenated amorphous silicon with low doping level
(p++)a-Si:H	p-type hydrogenated amorphous silicon with high doping level
c-Si	crystalline silicon
(n)c-Si	n-type crystalline silicon
uc-Si	microcrystalline silicon
uc-Si:H	hydrogenated microcrystalline silicon

$\times$	cross product
$\nabla\cdot$	divergence operator
$\nabla\times$	curl operator
$\langle . \rangle$	time period average
$\Re$	real part
$\Im$	imaginary part
i	imaginary unit
*	complex conjugate
$\otimes$	Kronecker product

$\mathbf{A}$	amplitudes vector
$\mathbf{A}^{(i)}$	amplitudes vector in i-th layer
A	absorptance
A_C, B_C, C_C	fitting parameters of Cauchy transparent model
A_L	oscillator amplitude
$AM1.5G$	global standard solar spectrum at the Earth's surface
AOI	angle of incidence
$\mathbf{B}(\mathbf{r}, t)$	magnetic flux density
C	oscillator broadening
c	light speed in free space
$\mathbf{D}(\mathbf{r}, t)$	electric displacement
$\mathbf{D}^{(i)}$	dynamic matrix of i-th layer
d	distance, thickness
$\mathbf{E}(\mathbf{r}, t)$	electric field vector
$\mathbf{E}_\omega(\mathbf{r})$	complex amplitude of electric field
$\mathbf{E}_0$	electric field complex envelope
E	photon energy
E_g	energy band gap
E_p	plasma energy
$E_{L,0}$	oscillator position
$\mathbf{e}$	electric field polarization vector
FF	fill factor
f_j	volume fraction of j-th material
$\mathbf{H}(\mathbf{r}, t)$	magnetic field vector
$\mathbf{H}_\omega(\mathbf{r})$	complex amplitude of magnetic field
$\mathbf{H}_0$	magnetic field complex envelope
$\mathbf{h}$	magnetic field polarization vector
$\widehat{\mathbb{I}}$	identity matrix
I	optical intensity
I_C, I_S	ellipsometric parameters

$\mathbf{J}$	Jones matrix
$J_{ph\,loss}$	loss in photo-generated current density
J_{SC}	short-circuit current density
$\mathbf{j}(\mathbf{r},t)$	current density vector
k	imaginary part of refractive index
L	layer thickness
$\mathbf{M}$	Mueller matrix
M	total matrix of thin film system
$\mathbf{M}(\mathbf{r},t)$	magnetization vector
M	number of spectral points
N	number of fitting parameters
N_x, N_y, N_z	propagating constants
NA	numerical aperture
n	real part of refractive index
$\tilde{n}$	complex refractive index
$\widehat{n}$	complex tensor of refractive index
$\mathbf{P}(\mathbf{r},t)$	polarization vector
$\mathbf{P}^{(i)}$	propagation matrix of i-th layer
$\mathcal{P}$	Cauchy principal value
P	pyramid geometrical factor
P_D	depolarization index
p	thickness of gradient p-type layer
q	electron charge
R	reflectance
r	amplitude reflection coefficient
$\mathbf{r}$	space position vector
S	Stokes vector
S	Poynting vector
S_ω	complex Poynting vector
T	transmittance
t	time, amplitude transmission coefficient
$\mathbf{u}$	unit normal vector
V_{OC}	open circuit voltage
v	light speed in medium
x, y, z	space coordinates
z_i	i-th interface

α	pyramid vertex angle, absorption coefficient
β	pyramid side angle
Γ_D	collision frequency of free carriers
γ	emerging angle
γ_L	oscillator damping
γ_S	factor related to a screening and a shape of inclusions
Δ	ellipsometric phase angle
δ	absolute phase change
ε	electric permitivity, dielectric function
$\widehat{\varepsilon}$	electric permitivity tensor
$\tilde{\varepsilon}$	complex electric permitivity
$\varepsilon^{(i)}$	complex relative permitivity of i-th medium
ε_r	relative electric permitivity
$\widehat{\varepsilon}_r$	relative permitivity tensor
$\tilde{\varepsilon}_r$	complex relative permitivity
ε_0	free space electric permitivity
ε_1	real part of complex relative permitivity
ε_2	imaginary part of complex relative permitivity
ε_∞	high-frequency dielectric constant
η	impedance of medium
η_0	impedance of free space
θ	phase shift
ϑ	polar angle
$\boldsymbol{\kappa}$	wave vector
κ	wavenumber
$\tilde{\kappa}$	complex wavenumber
κ_0	wavenumber in free space
λ	wavelength
μ	magnetic permeability
$\widehat{\mu}$	magnetic permeability tensor
μ_r	relative magnetic permeability
$\widehat{\mu}_r$	relative permeability tensor
μ_0	free space magnetic permeability
ν	frequency
$\rho(\mathbf{r}, t)$	charge volume density
ρ_S	degree of light polarization
σ	electric conductivity
$\widehat{\sigma}$	electric conductivity tensor
σ_{SD}	standard deviation
$\sigma_{i,k}$	estimated measurement error

φ	angle of incidence, angle of propagation
ϕ	azimuthal angle
χ_e	electric susceptibility
$\widehat{\chi}_e$	electric susceptibility tensor
χ_m	magnetic susceptibility
$\widehat{\chi}_m$	magnetic susceptibility tensor
χ^2	fitting error function
Ψ	ellipsometric amplitude angle
ω	angular frequency

1 Introduction

Outline

Energy is an essential element to ensure human life needs. We need energy to produce and supply food and clean water. We need it for heating, to ensure health care and security. We use energy every day to improve our life well-being. Figure 1.1 shows the world consumption of primary energy per capita in tonnes of oil equivalent in 2014.

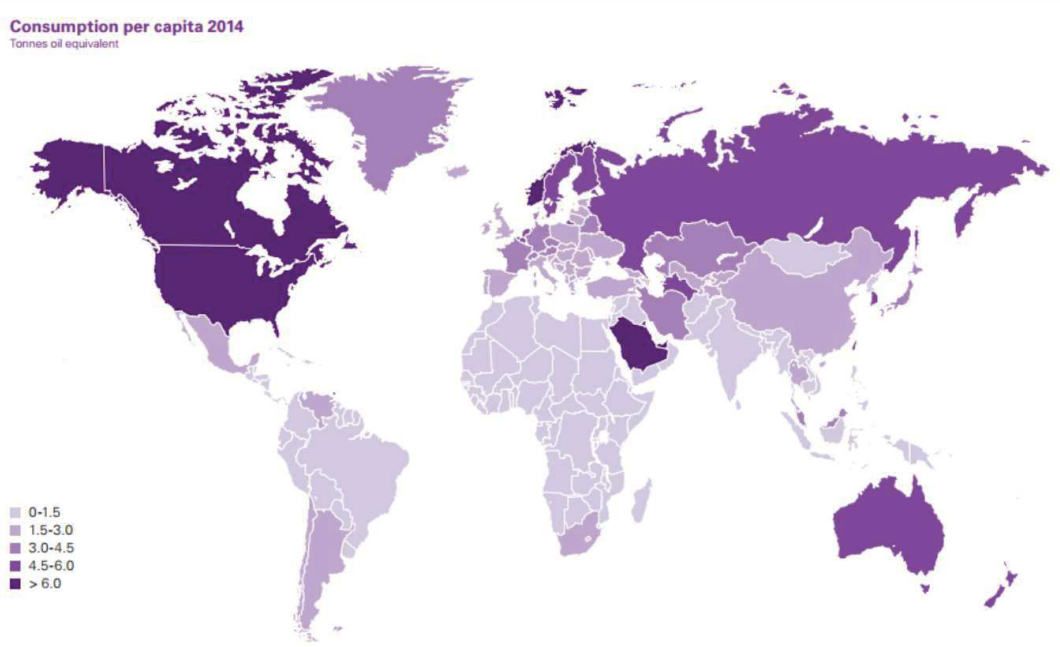

Figure 1.1 – World primary energy consumption per capita in tonnes of oil equivalent in 2014. This figure was adapted from Ref. 1.

World energy consumption is driven by two divergent driving forces. Rapid growth and improving prosperity mean the growth in energy demand mainly in fast developing economies, particularly in Asia. On the contrary, improvement of energy efficiency thanks to technological developments decelerates the increase of global energy consumption. As a result, energy consumption still grows but the growth has slowed down in recent years. The growth was only 1 % or less during last three years [2]. Furthermore, the energy mix is shifting towards cleaner, lower carbon fuels. This trend is driven by environmental needs and allowed by technological advances. The shift is well-documented by a sharp decrease of coal consumption in two last consecutive years (-1.7 % in 2016 [2]) and by a strong increase in renewable energy use. Renewable power, led by wind (increased by 15.6 %, 131 TWh in 2016) and solar (increase of 29.6 %, 77 TWh in 2016), is the fastest growing energy source (increase of 12 % in 2016 [2]), accounting for almost a third of the increase in primary energy, despite having a share of only 4 % of it [2].

Renewable energy is now a key element of sustainable development strategies which, among others, address climate change and provide health benefits compared with fossil fuels [3]. Unlike fossil fuels, renewable energy sources such as solar or wind energy are virtually unlimited. The advantage of using the solar energy stands from its presence anywhere in the world, without limitations or the dependence imposed by the strategic location of scarce fossil or nuclear fuels.

The current trend of harvesting the energy from the Sun tends towards the photovoltaic (PV) devices which can directly convert the solar energy into electricity. Photovoltaics has already accounted for about 2 % of global electricity in 2016 [3]. Moreover, the integration of PV into electricity system has reached 10-20 % in some countries such as Germany, Italy or Samoa [3]. The PV is the fastest growing sector of electricity generated from renewable sources. Its power capacity increased by 31.5 % and reached 295 GW in 2016 which accounts for 44 % of the increase in total electric capacity from renewable sources [4]. PV now represents more than half of all investment in the renewable energy sector [3].

The rapid diffusion of PV is supported by new technologies which make better performance available at lower cost. The cost reduction was dramatic in few past years and PV became cost-competitive with electricity from conventional sources. The levelized cost of electricity for utility-scale PV was typically between 6 and 10 US cents (USD 0.06-0.10) per kilowatt-hour (kWh) in Europe, China, India, South Africa and USA in 2015. Record low prices below USD 0.06/kWh were set in 2015 in United Arab Emirates (USD 0.0584/kWh), Peru (USD 0.048/kWh), and Mexico (USD 0.045/kWh) [3]. The price under three cents (USD 0.0299/kWh) was achieved in Dubai in 2016 [3]. Figure 1.2 shows prices of utility-scale solar PV in key markets in 2015. In comparison, the electricity production from coal- and gas-fired power stations was in the range of USD 0.05-0.10/kWh in 2015 [3]. Morover, there is also a big expansion in rooftop PV installations, which can provide electric power at lower cost than the grid in many countries.

Not only the cost of electricity but also the cost of building PV plant is nowadays close to or lower than that of conventional power plant [3]. Building utility-scale PV system can thus be cheaper and much faster than building new gas- or coal-fired power stations.

Another often mentioned draw-back, the energy pay-back (the time needed for a PV panel to produce energy used for its fabrication), has also been addressed. The energy pay-back has been reduced down to 2 years or less [3] (depending on location) by improvements in resource use, manufacturing process and efficiency.

The significant cost reduction is certainly the primary driver for PV diffusion. However, there are also other aspects. The transfer of PV technology is not limited by strict security restrictions in contrast with nuclear power. Furthermore, the expansion of PV has contributed significantly to reduction of CO_2 emissions

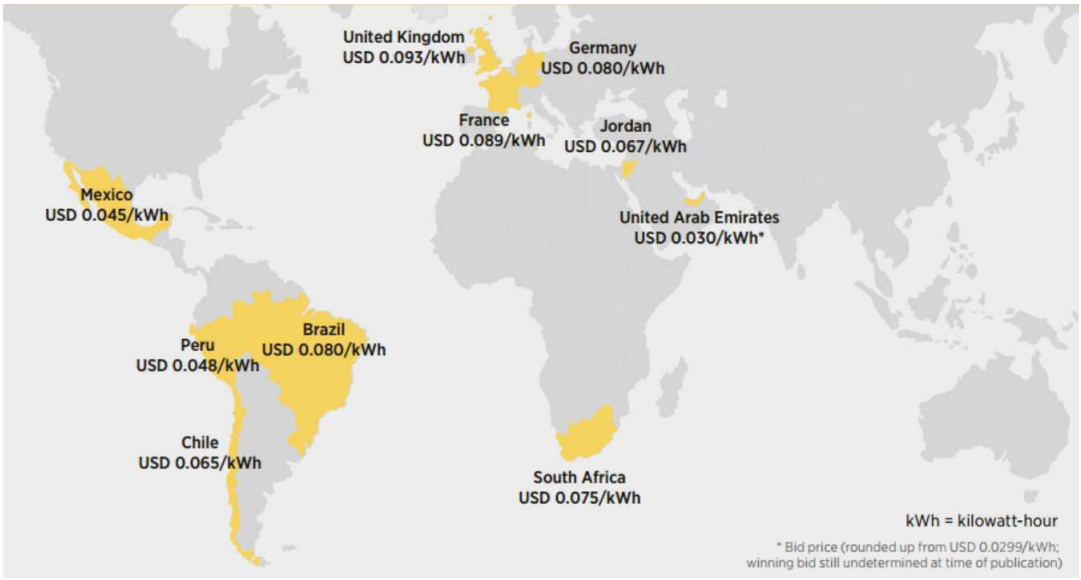

Figure 1.2 – Prices of utility-scale solar PV in key markets in 2015. This figure was adapted from Ref. 3.

by 200-300 million tonnes per year [3]. Photovoltaics together with other renewables provide major health benefits compared to fossil fuels.

1.1 Photovoltaic applications

Large area power plants usually come into the mind first when thinking about PV systems. However, the PV applications are much broader. Apart from the utility-scale PV stations, rooftop PV systems, building integrated PV and rural electrification of areas that are off grid, there are many other areas in which PV is used. Examples of various PV applications are illustrated in Fig. 1.3.

There is a long tradition of using PV for spacecraft applications. In fact this was one of the earliest PV applications. PV panels are installed on satellites, probes and on the International Space Station. They provide power for sensors, heating and cooling, communication systems etc. The crucial parameters for spacecraft systems are the power generated per kilogram and stability under extreme space conditions. Therefore high-efficiency but more expensive panels based on advanced designs and III-V semiconductors are preferred [5].

Photovolatic panels can also be integrated to vehicles such as cars, boats and even airplanes. They can be used to charge the electric vehicles or just as an additional power supply for smaller systems, for example air-conditioning. The cost and efficiency are usually the most important parameters of PV panels for

these applications, as well as the weight, durability, and flexibility which allows the integration of panels.

Various PV modules and mini-modules are used in solar powered standalone devices. There are plenty of them from well-known calculators and watches, through solar lamps, temporary traffic signs, parking meters, to water pumps or remote sensors of environment. The price plays the key role for these applications, while the generated power and size can be smaller.

Another field of applications is represented by solar chargers reaching from large charging stations for vehicles through portable standalone devices of various sizes to chargers integrated to bags or clothes.

Figure 1.3 – Examples of PV applications. Sources of particular images are indicated within the figure.

Various applications have various demands on PV module properties such as cost, efficiency, weight, size, durability, flexibility, mobility etc. Fortunately, there are many different PV technologies to choose from according to preferred properties.

The PV market is dominated by crystalline silicon (c-Si) technology. It accounts for about 90% [6] of market and it is usually the choice for utility-scale PV power plants and rooftop systems. It has undergone a long evolution and it approaches its theoretical efficiency limit of about 29% [3]. Thin film technologies such as hydrogenated amorphous silicon (a-Si:H), cadmium telluride, or copper indium gallium selenide benefit from reduced thickness ($0.6 - 3\,\mu$m in contrast to $180\,\mu$m thick c-Si wafers). This leads to material and cost savings and opens

new set of applications. Then, there are low-cost alternatives such as perovskites which exhibit reasonable good efficiency (22.1% [7]) but their problems with environmental stability and sensitivity to moisture have to be solved. The lower efficiency of organic (11.5% [7]) and dye-sensitised (11.9% [7]) PV cells is compensated by their lightweight, flexibility and relatively cheap production.

1.2 State of the art

The research in photovoltaics aims at lowering the price per watt of generated electrical power. This can be achieved by increasing the conversion efficiency of solar cells and by lowering their fabrication cost. Substantial efforts aim towards searching for new materials and designs which can push the limits of existing solar cells.

Surface texturing of solar cells is usually used to enhance light trapping and thus improves the conversion efficiency. The most widely used textures for crystalline silicon are pyramidal ones, since they are easy to fabricate at relatively low cost, while exhibiting well-documented light-trapping properties [8, 9].

Silicon heterojunction (SHJ) solar cells are an example of advanced architectures built on pyramidal textured wafers. They combine high efficiencies (24.7 % achieved already in 2014 [10]) with relatively low-cost fabrication thanks to the process temperatures below 200 °C. The SHJ structure was further improved by adding a thin intrinsic buffer layer leading to the heterojunction with intrinsic thin layer structure [11]. Panasonic pushed the limit to 25.6 % in 2014 by combining the SHJ concept with the interdigitated back-contact architecture [12]. A new efficiency record of 26.6 % for a practical size crystalline silicon solar cell has been achieved by Kaneka in 2016 [13], thanks to a combination of heterojunction technology using high-quality amorphous silicon, a low resistance electrode technology, and a back-contact structure that captures more light.

Another approach to enhance light absorption and to increase the conversion efficiency is incorporating nanostructures into the solar cell design. Silicon nanowire (SiNW) based radial junction solar cells open a new direction for nanostructured thin film devices due to their enhanced light trapping and decoupling of the direction in which light is absorbed from that in which charge carriers are collected [14, 15]. Radial junction devices can be fabricated using thin film deposition (forming radial junction) on the top of SiNW arrays grown by plasma-assisted vapor-liquid-solid (VLS) process [16]. This allows the use of thinner active layers [light trapping is strongly dependent on nanowire (NW) lengths] and the reduction of the carrier collection path (small radius of radial junctions). Because of the used low-melting point Sn as a catalyst, this method allows the fabrication of devices in a one-pump-down process with temperatures not exceeding

425 °C. This reduces the fabrication cost and opens the possibility to use low-cost substrates such as glass, flexible foils or even plastics [15]. An efficiency of 9.2 % was demonstrated for radial junction solar cells built over VLS-grown SiNWs with 100 nm thick intrinsic hydrogenated amorphous silicon [(i)a-Si:H] absorber on glass substrates [17].

The most recent development of complex materials and nanostructures for solar cells requires more effort to be put into their characterization and modeling. Optical methods are powerful characterization techniques, since they are fast, non-destructive, and non-invasive. Moreover, they can provide a lot of valuable information not only about the sample optical properties but also about their structure. Some optical measurements can be carried out even in-situ in the reactor and enable thus real-time monitoring of the sample during the fabrication process.

Monocrystalline silicon wafers are most commonly textured in an alkaline etching solution leading to a random array of upright pyramids on the etched surface [18–20]. The final morphology of the features has various implications for the performance of silicon solar cells. Front-surface reflectance, light-trapping capacity, module performance and surface recombination may all be affected [21].

Studies on pyramidal textured wafers (for example see [19, 22]) typically expect the pyramid vertex angle $\alpha = 70.52^\circ$ and base angle $\beta = 54.74^\circ$ as a result of ideal $\{111\}$ facet intersection. In contrast, careful examination of the features often reveals otherwise [23, 24]. Base angle of the texture depends on the etching solution and varies in the range of $49^\circ - 52^\circ$ [21, 25]. However, relatively few conclusions have been transferred into the analysis of surface texture in silicon solar cell applications.

The deviation from the ideal morphology is given to relation with the limited etching selectivity [26], but the precise mechanism remains questionable. Two proposed contributors are as follows: (i) the exposure of a convex corner of the growing feature results in the etching of higher index beveling planes that eventually intersect to form a stable bowed facet, and (ii) the formation of terrace-like structures on the pyramid facet as etching proceeds [23, 24, 27–29]. Given that the texture morphology evolves as the composition of an etch bath changes, a method for characterization of the evolving morphology is a critical requirement for the precise process control [21].

Pyramid geometry is particularly critical to the modeling and performance of the textured solar cells. The deviation from the ideal structure has numerous implications for silicon solar cell design, characterisation and modelling. Analyses of anti-reflection, light trapping, photogeneration and surface recombination properties of textured surfaces should take this feature morphology into account [21].

Computationally intensive analyses based on application of the 3-dimensional

ray-tracing calculus [30] are typically applied to describe reflection of incident light from pyramidal textured samples. Another approach for the calculation of reflectance and transmittance of textured silicon were introduced in [31]. It is based on the general expression for the reflectance of a pyramidal texture deduced from identification of discrete paths of the reflection and the fraction of reflected light that follows each of these paths. The fractions were determined again by geometrical ray-tracing. The analysis was extended to determine also the transmittance of the structure to allow optimization of the thickness of anti-reflective coatings. This approach still involves rather complex calculations and is far from an easy-to-apply method. In addition, the analysis doesn't take into account the real geometry of pyramids but employs the ideal one.

The precise control of thickness of deposited films (passivating and doped layers, anti-reflective coatings etc.) is crucial to obtain the designed solar cell architecture. Spectroscopic ellipsometry is a suitable method for film thickness characterization, since it is non-destructive, high-precision and extremely sensitive to the properties of interfaces and thin films. However, reduced reflectivity and high scattering of the textured surfaces which are desired for PV applications make the ellipsometric characterization rather challenging.

Spectroscopic ellipsometry measurements of pyramidal textured samples require an increased light source intensity and specific measurement configuration to obtain ellipsometric signal with a good signal to noise ratio [8]. Saenger et al. [9] proposed a method for spectroscopic ellipsometry measurements of SiN_x anti-reflective coatings on pyramidal textured wafers. They tilted the sample to align pyramid facets perpendicularly to the plane of incidence. Conventional flat optical model can be used for data analysis thanks to the measurement of the specular reflection from inclined pyramid facets. Watanabe et al. [32] applied this technique for thickness characterization of hydrogenated amorphous silicon on pyramids for silicon heterojunction solar cells. Matsuki et al. [33] used this technique for characterization of multi-layers on pyramids. They were able to determine not only the thicknesses but also the hydrogen content in a-Si:H film and carrier properties in indium tin oxide layer from ellipsometric data.

Spectroscopic reflectometry and ellipsometry are also suitable techniques to monitor processes during solar cell fabrication. Real-time spectroscopic ellipsometry is advantageously used for the monitoring and study of the growth of amorphous and microcrystalline silicon thin films [34–38]. However, using these methods for characterization of SiNW growth is much more challenging.

An in-situ spectroscopic ellipsometer module integrated in a plasma-enhanced chemical vapor deposition (PECVD) reactor was used by Yu et al. [39] to monitor in real time the optical response evolution of the SiNW structure. They traced the evolution of the intensity of light reflected from the sample surface and assessed the decrease in the reflected intensity to the enhanced light-trapping effect

during the growth of SiNW structure. However, they didn't model the ellipsometric data and a complete optical model representing the complex SiNW structure is still needed.

1.3 Objective of the work

The objective of this thesis is optical characterization, modeling, and structure optimization of advanced solar cell architectures fabricated in Laboratoire de Physique des Interfaces et des Couches Minces (LPICM). This includes study of silicon heterojunction solar cells fabricated on pyramidal textured wafers and radial junction solar cells built on randomly oriented silicon nanowires. We will demonstrate that optical methods are beneficial for characterization of both, widely used pyramidal textures as well as very challenging silicon nanowires.

Optimization of multi-layers in the heterojunction and fine tuning of pyramidal texture by etching processes is often performed by trial-and-error, without detailed analysis of the reasons for improved or reduced optical performance. Moreover, the geometry of pyramids is usually not verified and the ideal one resulting from the crystalography of silicon is assumed. This thesis focuses on a deeper study and understanding of the differences between various pyramidal textures and their impact on the solar cell design, fabrication, and performance.

The control of the SiNW growth process is essential for further improvement of the radial junction solar cell performance. The quality of deposition can be controlled by the characterization of materials and nanostructures during the growth process using an in-situ ellipsometry. Development of models able to describe and characterize the structure during the growth is highly desired. The model for the in-situ characterization is not always straight-forward, because some material properties as well as surfaces of deposited materials change during the growth. In this thesis, data obtained during SiNW sample fabrication will be analyzed to monitor the deposition process. The ultimate goal is the design of a model for the quality control of the growth process by means of in-situ ellipsometry.

To sum up, the focus of this thesis is on developing optical models adapted for the characterization of the photovoltaic devices, the quantitative criteria for the control of the quality of materials from different fabrication steps, and investigation of novel materials and nanostructures used to increase energy conversion efficiency of solar cells.

1.4 Organization of the thesis

The thesis is organized into following chapters:

Chapter 2 provides information on the preparation of studied samples. The fabrication of silicon heterojunction solar cells by plasma-enhanced chemical vapor deposition is described together with the etching processes used to create pyramidal textures on silicon wafers. The radial junction solar cell fabrication is introduced, including the description of plasma-assisted vapor-liquid-solid method for growth of randomly oriented silicon nanowires.

Chapter 3 introduces methods used for sample characterization. Measurement set-up for total reflectance and transmittance measurements as well as for various ellipsometric techniques are described.

Chapter 4 provides the theoretical background for the optical modeling. First, the electromagnetic theory of light is introduced. Then, the formalism describing light propagation in thin film systems is derived from the electromagnetic theory. Finally, principles of ellipsometric techniques are described and data analysis based on optical modeling of thin film systems is explained.

Chapter 5 summarizes results for pyramidal textured samples. The impact of various pyramidal textures on the total reflectance is studied. An easy-to-use model for reflectance from pyramidal surface is designed. Analysis of angles of real pyramids is performed, an explanation for the origin of the deviation from the ideal values is proposed, and consequences for thin film deposition and solar cell performance are discussed. The spectroscopic ellipsometry is employed for precise characterization of thicknesses of thin films on pyramids and an optical model for the optimization of thin-film systems on pyramidal textured wafers is designed. The importance of a precise control of the deposited film thicknesses is demonstrated on JV characteristic of final device.

Chapter 6 shows results of a study of silicon nanowire growth. First, the characterization of used materials is performed and obtained optical functions are adapted to correspond to the conditions in the reactor during fabrication process. Then, characterization of substrate before nanowire growth is carried out and suitable optical model is designed and verified. Finally, silicon nanowire growth is studied using ellipsometric data measured in-situ during the process. Multilayer optical model is designed and evolved to describe changing structure of the sample. Trends obtained from data modeling are analyzed.

2 Sample preparation

Outline

Samples of silicon heterojunction solar cells on pyramidal textured wafers were prepared in Laboratoire de Physique des Interfaces et des Couches Minces using plasma-enhanced chemical vapor deposition. Randomly oriented silicon nanowires which act as basis for radial junction solar cells were grown by plasma-assisted vapor-liquid-solid method in the same laboratory. I cooperated with my colleagues: Igor Sobkowicz, Soumyadeep Misra, Mutaz Al-Ghzaiwat, and Letian Dai, who processed the samples and did depositions, while I worked on sample characterization and processing and modeling of measured data.

2.1 Silicon heterojunction solar cells

Figure 2.1 shows the structure of a SHJ solar cell built on a pyramidal textured crystalline silicon wafer and the sample with finalized SHJ solar cells. N-type textured c-Si (n)c-Si wafers of thickness around $230\ \mu$m and resistivity of $2.6\ \Omega \cdot$cm were used as substrates. The fabrication of SHJ solar cells includes the deposition of intrinsic and doped hydrogenated amorphous silicon by low-temperature PECVD, the deposition of indium tin oxide (ITO) by magnetron sputtering at 180 °C, and the evaporation of silver contacts.

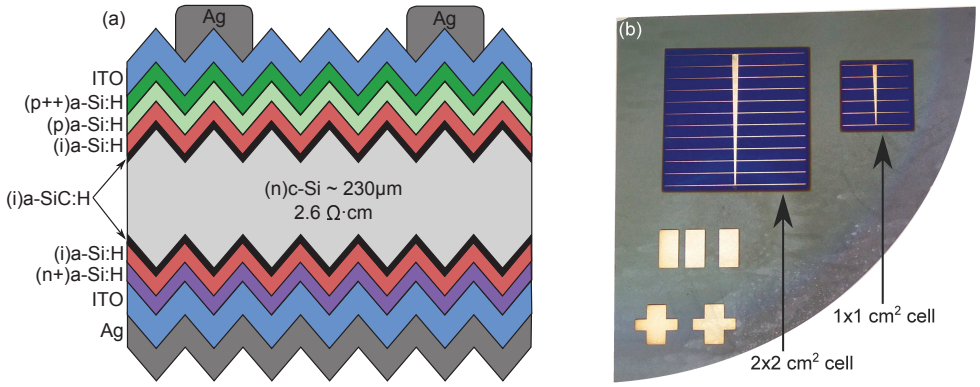

Figure 2.1 – Single heterojunction solar cells built on a pyramidal textured c-Si wafer. (a) Schematic drawing (the structure is not drawn to scale) and (b) photo of a sample with 2x2 cm^2 and 1x1 cm^2 SHJ solar cells.

Plasma-enhanced chemical vapor deposition is a process which enables deposition of thin films of various materials from a gas precursors onto substrates at lower temperature than that of a standard chemical vapor deposition (CVD) [40]. In PECVD process electron energy (plasma), instead of thermal energy (heat), is used to start the chemical reaction of gas precursors [41]. Plasma will ionize and decompose reactant gases leading to much lower deposition temperatures (as low as 175 °C [42]) than in thermally activated CVD (temperatures about

$600 - 1200$ °C) [41]. The lower deposition temperatures are critical in many applications, where CVD temperatures could damage the devices being fabricated. Furthermore, low deposition temperatures are desirable for industrial production since they reduce fabrication costs.

Plasma-enhanced chemical vapor deposition of thin films for SHJ devices at 200 °C includes: deposition of thin intrinsic a-Si:H [(i)a-Si:H] films on both sides of the textured wafer, deposition of n-type a-Si:H layer [(n+)a-Si:H] for the back surface field, deposition of gradient p-type a-Si:H layer for front emitter consisting of (p)a-Si:H and (p++)a-Si:H. It is noteworthy that a thin a-SiC:H buffer layer was first deposited directly on the wafer surface to hinder any potential epitaxial growth during the intrinsic a-Si:H layer deposition, according to the findings reported in [43,44]. The deposition conditions of materials for particular layers can be found in [43] and are listed in Table 2.1.

Material	SiH_4 (sccm)	Dopant	Pressure (mTorr)	Power (W)	Thickness (nm)
(i)a-Si:H	50	-	50	1	3.5
(i)a-SiC:H	25	50 sccm CH_4	40	1	1.5
(n+)a-Si:H	50	1 sccm PH_3 (1 % in H_2)	60	1	25
(p)a-Si:H	50	5 sccm TMB (1 % in H_2)	105 (Ar dilution)	1	1.5
(p++)a-Si:H	50	20 sccm TMB (1 % in H_2)	105 (Ar dilution)	2	8.5 - 17.5

Table 2.1 – Deposition conditions of materials produced by PECVD on textured c-Si wafers to obtain silicon heterojunction solar cells. The thicknesses of the films are considered in the normal direction to the pyramid facets.

An indium tin oxide layer, acting as a transparent conducting oxide (TCO) as well as an anti-reflective (AR) coating, was sputtered on both sides of solar cell precursor. The backside (n-side) was fully covered by ITO, whereas a 2x2 cm^2 area was covered on the front side (p-side) as shown in Fig. 2.1(b)). To finalize SHJ solar cells, silver was evaporated on both sides of the solar cell on top of the ITO. A deposition was made on the whole backside ITO surface, whereas an optimized front grid of bus-bar shape was used on the front side to reduce the shading.

2.1.1 Description of textured wafers

The alkali-based anisotropic wet chemical etching of (100)-oriented c-Si wafers results in the formation of regularly-shaped pyramids created by intersections of $\{111\}$ crystallographic planes [45]. These pyramids have the same shapes and facet orientations, but different sizes and randomly distributed locations on the wafer surface [see Fig. 2.2(A1, B1)].

Pyramidal textures were created on both surfaces of 280 μm thick n-type c-Si wafers using the alkaline 1.7 %-dilute KOH etching solution. This texturing process reduces the thickness of wafers to about 230 μm. Two different texturing procedures were applied. In the first solution, that we will name "type A" the isopropyl alcohol (IPA) was used as an additive to the KOH solution, while in the second solution "type B" an industrial surfactant (RenaTex) was added to the KOH solution.

First, the as-cut wafers were dipped for 3 minutes into a 22 %-NaOH solution at 80 °C to remove damages related to the wire cutting of silicon ingots. Next, the wafers were divided into two batches. One batch was textured using a type A solution for 30 minutes, while the second one was textured using a type B solution for 45 minutes. Type A solution gives larger pyramids featuring square basis of 10-15 μm as can be observed in Fig. 2.2(A1). On the other hand, type B solution leads to pyramids with smaller basis, reaching 4-5 μm [see Fig. 2.2(B1)].

In our work, we studied series of three samples of each type (A and B). For each type, there was a pyramidal sample without any additional surface post-treatment (A1 and B1), one sample after short additional surface post-treatment (A2 and B2), and one after long surface post-treatment (A3 and B3) (see Fig. 2.2). The objective of the post-treatment is to transform the sharp V-shaped surface morphology of the valley bottom into smoother U-shaped valleys by CP133 chemical solution at 14-22 °C. CP133 is a mixture of HF (50 % in H_2O), HNO_3 (65 % in H_2O), and CH_3COOH (100 %) in 1:3:3 volume ratio proportions. The short post-treatment of 70 and 40 seconds was used to produce samples A2 and B2, respectively. A 180 s long post-treatment was applied to obtain both A3 and B3 samples. Further details on texturation processes can be found in [43].

2.2 Radial junction solar cells

Radial junction solar cell fabrication consists of a PECVD deposition of intrinsic and n-type a-Si:H layers over p-type silicon nanowire arrays grown by plasma-assisted VLS method, magnetron sputtering of ITO and creating silver contacts. Complete solar cell structure (without Ag contacts) is schematically drawn in Fig. 2.3(a) while an example of sample is shown in Fig. 2.3(b).

The VLS process based on the use of a CVD system with the assistance of

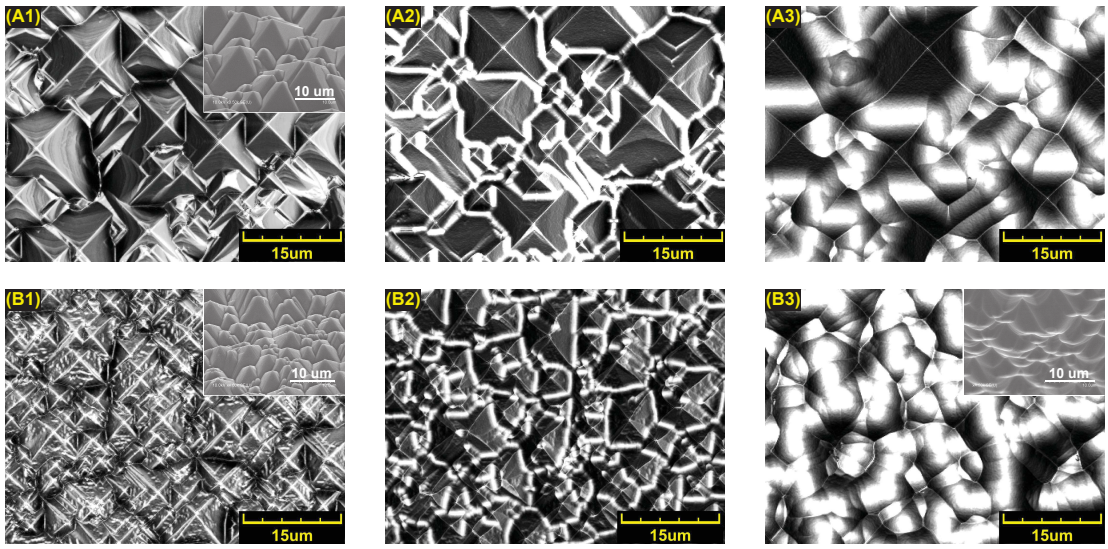

Figure 2.2 – Laser scanning confocal microscopy images of studied samples. (A1) type A without additional surface post-treatment, (A2) type A after short (70 s) surface post-treatment, (A3) type A after long (180 s) surface post-treatment, (B1) type B without surface post-treatment, (B2) type B after short (40 s) surface post-treatment, and (B3) type B after long (180 s) surface post-treatment. Inset figures show scanning electron microscopy (SEM) images of partially tilted samples A1, B1, and B3.

metal catalyst droplets is the most common bottom-up approach to synthesize SiNWs. In this process, the catalyst is heated above its eutectic temperature with Si, while gas precursors such as silane (SiH_4) or silicon tetrachloride ($SiCl_4$) are preferentially adsorbed and decomposed at the surface of the liquid metal droplet. Upon dissolution into the droplet, Si atoms form a liquid eutectic alloy with the catalyst material. Eventually, with the continuous flow of precursor gases, the alloy becomes supersaturated, overcomes the nucleation barrier and Si begins to precipitate at the liquid-solid interface in order to minimize the free energy of the system. As this process goes on, the alloy droplet gets displaced from the substrate leading to the growth of SiNWs [15].

A relatively high process temperature required in CVD (which is not compatible with the use of low-cost substrates) can be reduced by using plasma-assisted VLS method which opens the way to the use of glass [46] and flexible substrates [47]. Furthermore, exploiting the plasma to dissociate gas precursors allows for the use of a wider range of metals which are not able to dissociate process gases by themselves (in contrast with Au) as mediators for SiNWs growth [48].

Combination of plasma-assisted VLS for nanowire growth with PECVD depo-

sition of thin films has the advantage, that a whole radial junction solar cell can be fabricated in just one-pump-down process and is compatible with industrial PECVD reactors.

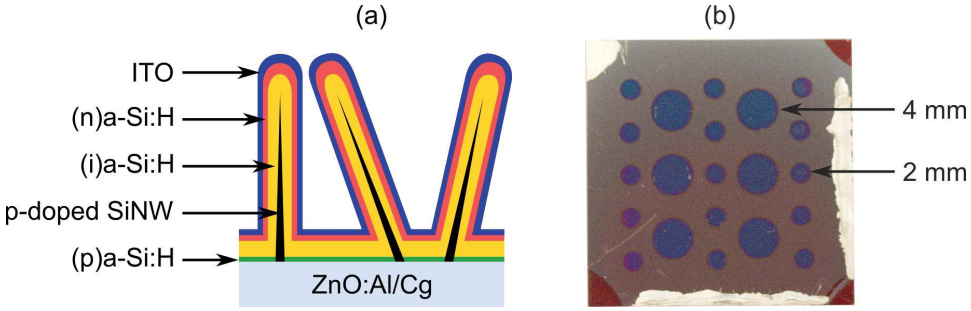

Figure 2.3 – Radial junction solar cells built on silicon nanowire arrays. (a) Schematic drawing (the structure is not drawn to scale) and (b) photo of a sample with solar cells of 2 and 4 mm diameters.

A 100 nm thick absorber layer of (i)a-Si:H is deposited by PECVD over p-type SiNWs. The deposition takes 60 min at 180 °C and the deposition conditions are: 10 sccm SiH_4 flow rate, chamber pressure of 120 mTorr and RF power density of 20 mW/cm^2 [49]. Then, 1 sccm of phosphine (PH_3 1% diluted in H_2) is introduced into the reactor chamber as the dopant gas to deposit (n)a-Si:H layer to complete the PIN radial junction.

The radial junction solar cells are finalized by RF magnetron sputtering of ITO ($In_2O_3 : SnO_2 = 9 : 1$) at 180 °C to create the top contact [49]. A mask with circular openings of 2 mm and 4 mm in diameter is used to define the solar cell areas [see Fig. 2.3(b)]. Finally, the tiny Ag dots are created in the middle of each solar cell to provide a good electrical contact for measuring probes.

2.2.1 Silicon nanowires grown for radial junction solar cells

Random silicon nanowire arrays are grown by plasma-assisted VLS method in a PECVD reactor. Tin was chosen as the metal mediator for SiNW growth [49], since it is abundant, has low melting point (around 232 °C) and doesn't introduce undesirable deep defects in the band gap of Si [50] (in contrast with Au [51]) which increase the recombination rate of photogenerated carriers [52] and are detrimental for the carrier life-time and diffusion length.

The Sn layers with a nominal thickness of 2 nm were thermally evaporated on the 1 mm thick Corning glass substrate of inch by inch area covered by an aluminum doped ZnO (ZnO:Al) film of a nominal thickness of 2 μm. ZnO:Al was chosen to provide back contact, since it has better stability in H_2 plasma en-

vironment than other transparent TCOs such as ITO or fluorine-doped tin oxide SnO_2:F (FTO). It was deposited by RF magnetron sputtering at 180 °C.

Sn layers were exposed to H_2 plasma for 2 min at 180 °C, to remove tin oxide and form Sn droplets. The chamber pressure, the RF power density, and the H_2 flow rate were fixed at 600 mTorr, 25 mW/cm^2 (nominal power of 5 W) and 100 sccm, respectively [49], to obtain well-separated metal droplets with narrow size distributions. Then, the substrate temperature was increased to 400 °C and after 10 min stabilization, 10 sccm of silane (SiH_4) and 1 sccm of trimethylboron (1% TMB diluted in H_2) were introduced to initiate the growth of p-doped SiNWs by plasma-assisted VLS method with 10 mW/cm^2 power density (nominal power 2 W) [16]. The conditions were kept constant during 10 min of SiNW growth resulting in 0.8-1 μm long nanowires with 30-50 nm diameter at their bases and less than 20 nm diameter at their tips. Figure 2.4 shows the crucial steps of the fabrication process.

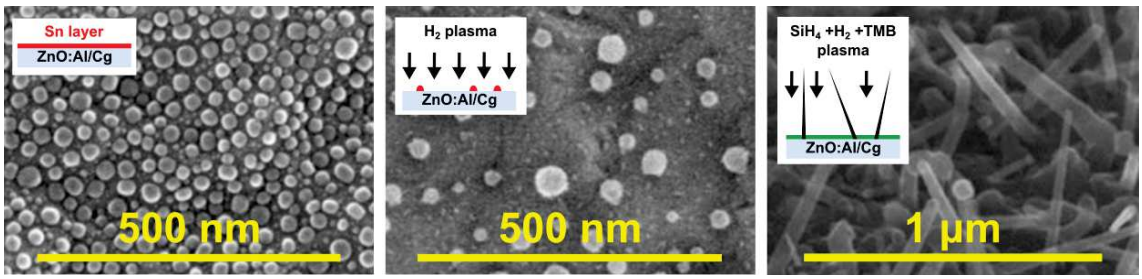

Figure 2.4 – SEM images of (a) Sn deposited on the Corning glass substrate covered by ZnO:Al, (b) Sn droplets formation after 2 min of H_2 plasma treatment, and (c) random silicon nanowires grown by plasma-assisted VLS method for 8 minutes. Insets illustrate schematically the fabrication process steps [49].

3 Characterization methods

Outline

This chapter introduces methods which were used for characterization of studied samples. We have used mainly optical characterization methods as you can see below, since they are fast, non-destructive, and non-invasive and they can provide us a lot of valuable information not only about the sample optical properties but also about their structure. Moreover, some optical measurements can be carried out even in-situ in the reactor and allow us to monitor the sample during the fabrication process.

In Section 3.1 the spectroscopic measurement of total reflectance and transmittance is described. This section is followed by Section 3.2 on standard and Mueller matrix ellipsometry which is further divided into Section 3.2.1 devoted to the spectroscopic ellipsometry, Section 3.2.2 dealing with the in-situ Mueller matrix polarimetry, and Section 3.2.3 on angle-resolved Mueller matrix polarimetry.

3.1 Total reflectance and transmittance measurements

PerkinElmer UV/Vis/NIR spectrophotometer Lambda 950 with a 150 mm integrating sphere has been used to measure the sum of total reflectance and transmittance of the pyramidal textured wafers to assess the impact of the surface texture on the light-trapping properties. The sum of the total specular and diffuse reflectance and transmittance of the sample corresponding to $(R + T = 1 - A)$, where A is the absorptance, has been measured with the sample inside the integrating sphere in the spectral range from 250 to 1100 nm with an increment of 5 nm. All six samples with different surface treatments (see Fig. 2.2) were measured at the normal angle of incidence (AOI) with respect to the plane of the wafer. Second, both types of samples with no additional surface post-treatment (A1 and B1) were also measured at oblique angles of incidence reaching values from 8° to 60°.

3.2 Standard and Mueller matrix ellipsometry

The advantage of using ellipsometric techniques such as standard spectroscopic ellipsometry or Mueller matrix polarimetry is, that in contrast with the spectroscopy presented above in Section 3.1, the ellipsometric techniques measure not only the change of amplitude but also the phase shift of polarized light after its interaction with a sample. This allow us to obtain more information about the studied sample. Following subsections describe measurement set-ups for different types of ellipsometric techniques used for characterization of samples in this thesis. More details on the principles of ellipsometric measurements and the

theory behind data analysis can be find in Section 4.3 of Chapter 4.

3.2.1 Standard spectroscopic ellipsometry

Ex-situ scanning spectroscopic phase modulated ellipsometer measurements (Uvisel 2, Horiba Scientific) of reference samples have been carried out to determine optical functions of used materials. The Uvisel 2 with the 150 W Xenon light source was used to measure reference samples of of a-Si:H, a-SiC:H, (p)a-Si:H, (p++)a-Si:H, ITO, Sn and ZnO:Al thin films on Corning glass substrates. The measurements have been performed in a wide spectral range of 230-2000 nm (0.6-5.4 eV) at the angle of incidence of 70°.

Spectroscopic ellipsometry on pyramidal textures

Reduced reflectivity and high scattering of the pyramidal textured surface require an increased light source intensity and specific measurement configurations for ellipsometric signal with a good signal to noise ratio [8].

Scanning spectroscopic phase modulated ellipsometer UVISEL 2 (Horiba Scientific) with a 150 W Xenon light source has been used to measure spectroscopic ellipsometry data of samples with pyramidal texture. This ellipsometer is equipped with a double monochromator system for the ultraviolet-visible (UV-VIS) range from 190 nm to 880 nm and twin photomultiplier tube detectors for the higher sensitivity and dynamic range. It has a near-infrared (NIR) extension, covering the spectral range up to 2100 nm, consisting of monochromator for NIR range (880-2100 nm) and InGaAs detector. This ellipsometer allows variable angle spectroscopic ellipsometry measurements in the range from 35° to 90°.

The lateral measurement geometry, which is based on aligning the pyramidal facets perpendicular to the plane of incidence, was used for measurements as described in Ref. [9]. An inclination stage has been used to align a sample to the required position in order to obtain specular reflection from the facets (for illustration see Fig. 3.1). First, the angle of incidence, set by a goniometer, was verified by a measurement of the reference flat wafer with a 22.1 nm layer of thermal oxide. Then, the textured sample was mounted on the inclination stage so that one straight edge of the quarter-wafer representing the $[1\bar{1}0]$ direction was parallel to the plane of incidence. The computer controlled XYZ stage was used to adjust the spatial position of the sample. Then, we inclined the sample using the inclination stage to set the $(1\bar{1}\bar{1})$ facets of the pyramids to be in horizontal sample plane. The ideal inclination angle of 54.74° (for ideal pyramids) corresponds to the angle between a facet and a base of a pyramid defined by the geometry of anisotropic wet-etching. The inclination angle of the stage was set to 55° and then tuned manually for particular sample geometry to maximize the brightness

of the spot displayed by the vision system providing a real-time color image of the sample and exact measurement spot using the ellipsometer head.

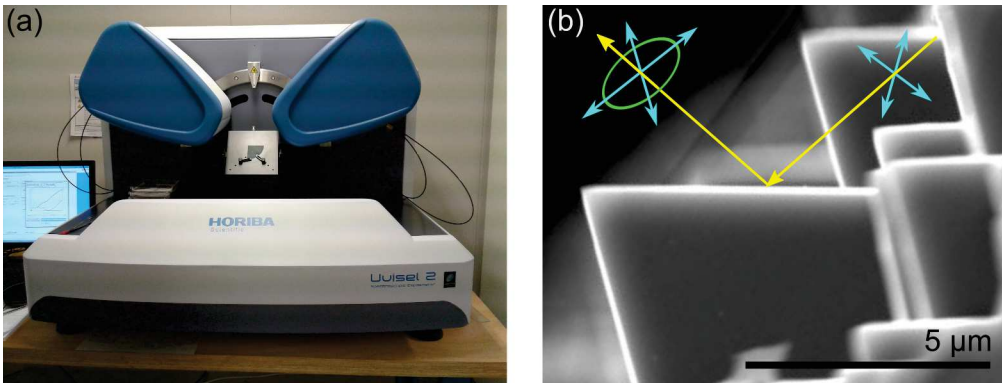

Figure 3.1 – Measurement set-up for samples with pyramidal texture using the inclination stage of UVISEL 2 (Horiba Scientific) (a) and schematic representation of measurement geometry (b).

The accuracy of the sample adjustment was verified by comparison of the angle of incidence acquired from the ellipsometry measurement of the sample with the angle of incidence previously set by the goniometer. If the fitted AOI was not close to that one obtained for the reference sample, the adjusting of the inclination angle and sample height was repeated. All sample measurements were carried out with an integration time of 500 ms and an elliptic spot size of 2×0.7 mm (value corresponding to the angle of incidence of 70°). The angles of modulator and analyzer were set to 0° and +45°, respectively.

3.2.2 In-situ spectroscopic Mueller matrix ellipsometry

We have used a Mueller matrix polarimeter (MM-16, Horiba Scientific) for a fast, non-destructive, large spot characterization of random silicon nanowire arrays during their growth. The MM-16 polarimeter has a liquid crystal based polarization state generator and analyzer allowing for measurements of all 15 elements of normalized Mueller matrices in the spectral range of 450 - 850 nm. Heads of MM-16 are fixed to the PECVD reactor windows (as shown in Fig. 3.2) to enable in-situ measurements during the deposition at the fixed angle of incidence of 71.2°. In-situ ellipsometric data has been measured every 1 min during sample fabrication starting from Sn droplets formation by H_2 plasma treatment and continuing during SiNW growth.

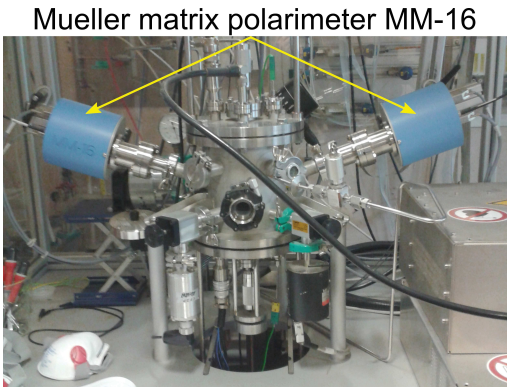

Figure 3.2 – Mueller matrix polarimeter installed on the PECVD reactor Plasfil.

3.2.3 Angle-resolved Mueller matrix ellipsometry

We have used angle-resolved Mueller matrix polarimeter (AR-MMP) with microscope objective of high numerical aperture ($NA = 0.95$) to measure complete Mueller matrices over the range of polar angles ϑ (0-60°) and azimuthal angles ϕ (0-360°). The polarimeter enables measurements of all elements of Mueller matrix in real and Fourier space at the same spot on the sample. A patented calibration [53] of this device is based on the single value decomposition [54]. The spot size diameter can be adjusted from a few micrometers up to $50\,\mu$m using an iris aperture. A halogen lamp was used as the light source. For more information on the measurement setup see Ref. 55. We have used a fine pinhole aperture to select only the near normal angle of incidence from the objective back focal plane.

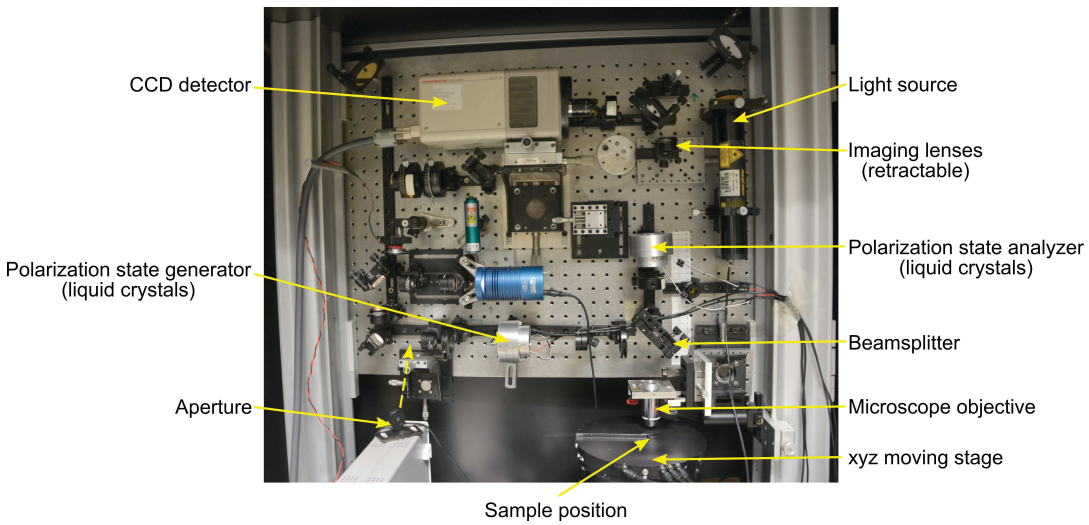

Figure 3.3 – Angle-resolved Mueller matrix polarimetry set-up.

4 Theoretical background for optical modeling

Outline

This chapter is devoted to explain the theoretical background which is essential for optical modeling and characterization of studied samples. First, the electromagnetic theory of light is introduced in Section 4.1. Then, the matrix formalism which is used to solve the light propagation in thin film systems is presented in Section 4.2. Finally, the principles of spectroscopic ellipsometry (SE) and Mueller matrix polarimetry measurements and data analysis are described in Section 4.3.

4.1 Electromagnetic theory of light

Light is an electromagnetic wave phenomenon described by the same theoretical principles that govern all forms of electromagnetic radiation. Optical frequencies occupy a band of electromagnetic spectrum that extends from the infrared through the visible to the ultraviolet [56].

Electromagnetic radiation propagates in the form of two mutually coupled vector waves, an electric-field wave and a magnetic-field wave. An electromagnetic field is then described by two related vector fields: the electric field and the magnetic field [56]. It is advantageous from the computational point of view to introduce the quantities which describe the electromagnetic field in the complex form. Measurable values of these quantities then correspond to their real parts. The electromagnetic field and its interactions with a medium is described by the Maxwell equations.

4.1.1 Maxwell equations in general medium

In a general medium with free charges of a volume density $\rho(\mathbf{r},t)$, and a current density $\mathbf{j}(\mathbf{r},t)$, the Maxwell equations define relations between complex quantities describing the electromagnetic field [the electric and the magnetic field $\mathbf{E}(\mathbf{r},t)$, $\mathbf{H}(\mathbf{r},t)$, the electric flux density (also called the electric displacement) $\mathbf{D}(\mathbf{r},t)$, and the magnetic flux density $\mathbf{B}(\mathbf{r},t)$] as follows [56,57]:

$$\nabla \times \mathbf{H}(\mathbf{r},t) = \frac{\partial \mathbf{D}(\mathbf{r},t)}{\partial t} + \mathbf{j}(\mathbf{r},t), \tag{4.1a}$$

$$\nabla \times \mathbf{E}(\mathbf{r},t) = -\frac{\partial \mathbf{B}(\mathbf{r},t)}{\partial t}, \tag{4.1b}$$

$$\nabla \cdot \mathbf{D}(\mathbf{r},t) = \rho(\mathbf{r},t), \tag{4.1c}$$

$$\nabla \cdot \mathbf{B}(\mathbf{r},t) = 0. \tag{4.1d}$$

Here $\nabla\times$ and $\nabla\cdot$ are the curl and divergence operations, respectively, $\mathbf{r}$ is the space position vector, and t is the time.

Material equations

The relation between the electric displacement $\mathbf{D}(\mathbf{r},t)$ and the electric field $\mathbf{E}(\mathbf{r},t)$ depends on the electric properties of the medium. Similarly, the relation between the magnetic flux density $\mathbf{B}(\mathbf{r},t)$ end the magnetic field $\mathbf{H}(\mathbf{r},t)$ depends on the magnetic properties of the medium. These relations are defined at macro-scale by material equations (also called constitutive relations) [56,57]:

$$\mathbf{D}(\mathbf{r},t) = \varepsilon_0 \mathbf{E}(\mathbf{r},t) + \mathbf{P}(\mathbf{r},t), \tag{4.2a}$$
$$\mathbf{B}(\mathbf{r},t) = \mu_0 \left[\mathbf{H}(\mathbf{r},t) + \mathbf{M}(\mathbf{r},t)\right]. \tag{4.2b}$$

The constants ε_0 and μ_0 are the electric permitivity and magnetic permeability of the free space, respectively. Vectors $\mathbf{P}(\mathbf{r},t)$ and $\mathbf{M}(\mathbf{r},t)$ are the polarization and the magnetization vectors.

Boundary conditions

At the boundary between two dielectric media and in the absence of free charges [$\rho(\mathbf{r},t) = 0$] and currents [$\mathbf{j}(\mathbf{r},t) = 0$], the tangential components of the electric and magnetic fields $\mathbf{E}(\mathbf{r},t)$ and $\mathbf{H}(\mathbf{r},t)$ and the normal components of the electric and magnetic flux densities $\mathbf{D}(\mathbf{r},t)$ and $\mathbf{B}(\mathbf{r},t)$ must be continuous [56]:

$$\mathbf{u}\times(\mathbf{E}_1 - \mathbf{E}_2) = 0, \tag{4.3a}$$
$$\mathbf{u}\times(\mathbf{H}_1 - \mathbf{H}_2) = 0, \tag{4.3b}$$
$$\mathbf{u}\cdot(\mathbf{D}_1 - \mathbf{D}_2) = 0, \tag{4.3c}$$
$$\mathbf{u}\cdot(\mathbf{B}_1 - \mathbf{B}_2) = 0, \tag{4.3d}$$

where $\mathbf{u}$ is the unit normal vector to the boundary and subscripts 1 and 2 number the media.

4.1.2 Classification of material media

According to the nature of parameters such as electric conductivity σ, electric permitivity ε, or magnetic permeability μ, and optical response, the media can be classified as [56]:

Nondispersive: the response of the medium is instantaneous, independent on the frequency and wavelength of the electromagnetic wave, $\varepsilon \neq \varepsilon(\omega,\lambda)$, $\sigma \neq \sigma(\omega,\lambda)$.

Dispersive: the response of the medium depends on the frequency and wavelength of the electromagnetic wave, $\varepsilon = \varepsilon(\omega,\lambda)$, $\sigma = \sigma(\omega,\lambda)$.

Homogeneous: the medium has the same properties at every point, $\varepsilon(\mathbf{r}) = \varepsilon$, $\sigma(\mathbf{r}) = \sigma$, $\mu(\mathbf{r}) = \mu$.

Inhomogeneous: properties of the medium vary with position, $\varepsilon(\mathbf{r})$, $\sigma(\mathbf{r})$, $\mu(\mathbf{r})$.

Isotropic: properties of the medium are uniform in all directions, $\varepsilon(\mathbf{r})$, $\sigma(\mathbf{r})$ and $\mu(\mathbf{r})$ are scalar parameters, independent on the direction of $\mathbf{E}$ and $\mathbf{H}$.

Anisotropic: properties of the medium depend on the direction, $\widehat{\varepsilon}(\mathbf{r})$, $\widehat{\sigma}(\mathbf{r})$, $\widehat{\mu}(\mathbf{r})$ are tensors.

Nonconductive: non-absorbing medium which is not able to conduct an electric current, $\sigma = 0$, $\mathbf{j} = \sigma\mathbf{E} = 0$.

Conductive: the medium absorbs light due to its nonzero conductivity $\sigma \neq 0$, $\mathbf{j} = \sigma\mathbf{E}$.

Linear: vector $\mathbf{P}(\mathbf{r}, t)$ is linearly related to vector $\mathbf{E}(\mathbf{r}, t)$.

Nonlinear: vector $\mathbf{P}(\mathbf{r}, t)$ is nonlinear function of vector $\mathbf{E}(\mathbf{r}, t)$.

In the following text, we will deal only with media without free charges $[\rho(\mathbf{r}, t) = 0[$, since the effects of free charges are already included in the permitivity of media. Further, we will limit our study to linear, homogeneous and non-dispersive media, since these correspond to materials studied in this work.

Maxwell equations for anisotropic medium

The polarization and magnetization vectors $\mathbf{P}(\mathbf{r}, t)$ and $\mathbf{M}(\mathbf{r}, t)$ are in the linear, homogeneous, non-dispersive medium expressed by the relations [56]:

$$\mathbf{P}(\mathbf{r}, t) = \varepsilon_0 \widehat{\chi}_e \mathbf{E}(\mathbf{r}, t), \tag{4.4a}$$

$$\mathbf{M}(\mathbf{r}, t) = \widehat{\chi}_m \mathbf{H}(\mathbf{r}, t), \tag{4.4b}$$

where $\widehat{\chi}_e$ and $\widehat{\chi}_m$ are the second rank tensors of relative electric and magnetic susceptibility, respectively. The substitution of the relations (4.4) into (4.2) allows to write the material equations in the form:

$$\mathbf{D}(\mathbf{r}, t) = \widehat{\varepsilon}\mathbf{E}(\mathbf{r}, t), \tag{4.5a}$$

$$\mathbf{B}(\mathbf{r}, t) = \widehat{\mu}\mathbf{H}(\mathbf{r}, t). \tag{4.5b}$$

Here $\widehat{\varepsilon}$ and $\widehat{\mu}$ are the tensors of electric permitivity and magnetic permeability, which are defined by the relations:

$$\widehat{\varepsilon} = \varepsilon_0 \left(\widehat{\mathbb{I}} + \widehat{\chi}_e\right) = \varepsilon_0 \widehat{\varepsilon}_r, \tag{4.6a}$$

$$\widehat{\mu} = \mu_0 \left(\widehat{\mathbb{I}} + \widehat{\chi}_m\right) = \mu_0 \widehat{\mu}_r, \tag{4.6b}$$

using the identity matrix $\widehat{\mathbb{I}}$, relative permitivity tensor $\widehat{\varepsilon}_r$, and relative permeability tensor $\widehat{\mu}_r$.

The current density vector $\mathbf{j}(\mathbf{r}, t)$ can be expressed using the electric conductivity tensor $\widehat{\sigma}$ as:

$$\mathbf{j}(\mathbf{r}, t) = \widehat{\sigma}\, \mathbf{E}(\mathbf{r}, t), \tag{4.7}$$

Assuming a medium without free charges $\rho(\mathbf{r}, t) = 0$ and applying (4.5) and (4.7) leads to the Maxwell equations for linear, nondispersive, homogenous, anisotropic medium in the following form:

$$\nabla \times \mathbf{H}(\mathbf{r}, t) = \widehat{\varepsilon}\, \frac{\partial \mathbf{E}(\mathbf{r}, t)}{\partial t} + \widehat{\sigma}\, \mathbf{E}(\mathbf{r}, t), \tag{4.8a}$$

$$\nabla \times \mathbf{E}(\mathbf{r}, t) = -\widehat{\mu}\, \frac{\partial \mathbf{H}(\mathbf{r}, t)}{\partial t}, \tag{4.8b}$$

$$\nabla \cdot [\widehat{\varepsilon}\, \mathbf{E}(\mathbf{r}, t)] = 0, \tag{4.8c}$$

$$\nabla \cdot \mathbf{H}(\mathbf{r}, t) = 0. \tag{4.8d}$$

Maxwell equations for isotropic medium

For isotropic media, the tensors $\widehat{\chi}$, $\widehat{\varepsilon}$, $\widehat{\mu}$, and $\widehat{\sigma}$ are simplified to the scalar constants χ, ε, μ and σ.

The electric permitivity ε and magnetic permeability μ are then expressed as:

$$\varepsilon = \varepsilon_0 (1 + \chi_e), \tag{4.9a}$$

$$\mu = \mu_0 (1 + \chi_m), \tag{4.9b}$$

where χ_e and χ_m are the electric and magnetic susceptibility, respectively. The ratios

$$\varepsilon_r = \frac{\varepsilon}{\varepsilon_0}, \tag{4.10a}$$

$$\mu_r = \frac{\mu}{\mu_0}, \tag{4.10b}$$

are the relative electric permitivity and magnetic permeability. Usual media studied in this thesis are not magneticaly active for optical frequencies resulting in $\mu = \mu_0$ and $\mu_r = 1$.

Maxwell equations (4.8) then simplify to the form:

$$\nabla\times\mathbf{H}(\mathbf{r},t)=\varepsilon\frac{\partial\mathbf{E}(\mathbf{r},t)}{\partial t}+\sigma\mathbf{E}(\mathbf{r},t), \tag{4.11a}$$

$$\nabla\times\mathbf{E}(\mathbf{r},t)=-\mu_0\frac{\partial\mathbf{H}(\mathbf{r},t)}{\partial t}, \tag{4.11b}$$

$$\nabla\cdot\mathbf{E}(\mathbf{r},t)=0, \tag{4.11c}$$

$$\nabla\cdot\mathbf{H}(\mathbf{r},t)=0. \tag{4.11d}$$

4.1.3 Electromagnetic waves in non-absorbing medium

In the non-absorbing, isotropic (ε and μ are scalar constants), nonconductive [$\sigma(\mathbf{r},t)=0$, $\mathbf{j}(\mathbf{r},t)=0$], homogeneous, nondispersive, linear medium with no free charges [$\rho(\mathbf{r},t)=0$], the Maxwell equations (4.11) are in the form:

$$\nabla\times\mathbf{H}(\mathbf{r},t)=\varepsilon\frac{\partial\mathbf{E}(\mathbf{r},t)}{\partial t}, \tag{4.12a}$$

$$\nabla\times\mathbf{E}(\mathbf{r},t)=-\mu\frac{\partial\mathbf{H}(\mathbf{r},t)}{\partial t}, \tag{4.12b}$$

$$\nabla\cdot\mathbf{E}(\mathbf{r},t)=0, \tag{4.12c}$$

$$\nabla\cdot\mathbf{H}(\mathbf{r},t)=0. \tag{4.12d}$$

By applying the curl operation $\nabla\times$ to (4.12b), using the vector identity $\nabla\times\nabla\times\mathbf{E}(\mathbf{r},t)=\nabla[\nabla\cdot\mathbf{E}(\mathbf{r},t)]-\Delta\mathbf{E}(\mathbf{r},t)$, and then using (4.12a) and (4.12c), we can derive the wave equation for $\mathbf{E}(\mathbf{r},t)$:

$$\Delta\mathbf{E}(\mathbf{r},t)-\frac{1}{v^2}\frac{\partial^2\mathbf{E}(\mathbf{r},t)}{\partial t^2}=0. \tag{4.13}$$

This equation describes the propagation of electromagnetic waves with the speed

$$v=\frac{1}{\sqrt{\varepsilon\mu}}. \tag{4.14}$$

The ratio of the speed of light in the free space $c=\frac{1}{\sqrt{\varepsilon_0\mu_0}}$ to that in the medium defines the refractive index:

$$n=\frac{c}{v}=\sqrt{\varepsilon_r\mu_r}, \tag{4.15a}$$

$$\text{and}\quad n=\sqrt{\varepsilon_r}\quad\text{for non-magnetic media}\ (\mu_r=1). \tag{4.15b}$$

Monochromatic waves

The electromagnetic wave is monochromatic when all components of the electric and magnetic fields are harmonic functions of the time at the same frequency:

$$\mathbf{E}(\mathbf{r},t) = \mathbf{E}_\omega(\mathbf{r})\exp(\mathrm{i}\omega t)\,, \tag{4.16a}$$
$$\mathbf{H}(\mathbf{r},t) = \mathbf{H}_\omega(\mathbf{r})\exp(\mathrm{i}\omega t)\,, \tag{4.16b}$$

where $\mathbf{E}_\omega(\mathbf{r})$ and $\mathbf{H}_\omega(\mathbf{r})$ are the complex amplitudes of the electric and magnetic field, respectively, $\omega = 2\pi\nu$ is the angular frequency, and ν is the frequency.

Substituting equations (4.16) into (4.12) and applying $\frac{\partial}{\partial t} \longrightarrow \mathrm{i}\omega$ leads to Maxwell equations in the time independent form:

$$\nabla \times \mathbf{H}_\omega(\mathbf{r}) = \mathrm{i}\omega\varepsilon\mathbf{E}_\omega(\mathbf{r})\,, \tag{4.17a}$$
$$\nabla \times \mathbf{E}_\omega(\mathbf{r}) = -\mathrm{i}\omega\mu\mathbf{H}_\omega(\mathbf{r})\,, \tag{4.17b}$$
$$\nabla \cdot \mathbf{E}_\omega(\mathbf{r}) = 0, \tag{4.17c}$$
$$\nabla \cdot \mathbf{H}_\omega(\mathbf{r}) = 0. \tag{4.17d}$$

Applying the monochromatic waves (4.16), the wave equation (4.13) transforms into the form:

$$\Delta\mathbf{E}_\omega(\mathbf{r}) + \kappa^2\mathbf{E}_\omega(\mathbf{r}) = 0. \tag{4.18}$$

This equation is called the Helmoltz equation, in which

$$\kappa = \frac{\omega}{v} = \omega\sqrt{\varepsilon\mu} = n\frac{\omega}{c} = n\kappa_0. \tag{4.19}$$

Here κ is the wavenumber and $\kappa_0 = \frac{\omega}{c} = \frac{2\pi}{\lambda}$ is the wavenumber in the free space for wavelength λ.

Plane monochromatic waves

One of the possible solutions of the Helmholtz equation are plane monochromatic waves in the form:

$$\mathbf{E}_\omega(\mathbf{r}) = \mathbf{E}_0\exp[-\mathrm{i}\boldsymbol{\kappa}\mathbf{r}]\,, \tag{4.20a}$$
$$\mathbf{H}_\omega(\mathbf{r}) = \mathbf{H}_0\exp[-\mathrm{i}\boldsymbol{\kappa}\mathbf{r}]\,, \tag{4.20b}$$

where $\mathbf{E}_0$ and $\mathbf{H}_0$ are the complex envelopes of the wave, and $\boldsymbol{\kappa}$ is the wave vector of magnitude $\kappa = n\kappa_0$.

Substituting the plane monochromatic waves (4.20) into (4.17) and applying $\nabla \longrightarrow -\mathrm{i}\boldsymbol{\kappa}$ the Maxwell equations get the form:

$$\boldsymbol{\kappa} \times \mathbf{H}_0 = -\omega\varepsilon\mathbf{E}_0, \tag{4.21a}$$
$$\boldsymbol{\kappa} \times \mathbf{E}_0 = \omega\mu\mathbf{H}_0, \tag{4.21b}$$
$$\boldsymbol{\kappa} \cdot \mathbf{E}_0 = 0, \tag{4.21c}$$
$$\boldsymbol{\kappa} \cdot \mathbf{H}_0 = 0. \tag{4.21d}$$

It follows from (4.21a) that $\mathbf{E}_0$ is normal to both $\mathbf{H}_0$ and $\boldsymbol{\kappa}$, and equation (4.21b) implies that $\mathbf{H}_0$ is normal to both $\mathbf{E}_0$ and $\boldsymbol{\kappa}$. Thus $\mathbf{E}_0$, $\mathbf{H}_0$, and $\boldsymbol{\kappa}$ have to be mutually orthogonal for isotropic medium. Since $\boldsymbol{\kappa}$ determines the direction of wave propagation, $\mathbf{E}_0$ and $\mathbf{H}_0$ lie in the plane normal to the direction of propagation.

4.1.4 Electromagnetic waves in absorbing medium

In the isotropic (ε, μ, σ are scalar constants), absorbing medium [$\sigma(\mathbf{r},t) \neq 0$, $\mathbf{j}(\mathbf{r},t) \neq 0$] with no free charges [$\rho(\mathbf{r},t) = 0$] the Maxwell equations have the form:

$$\nabla \times \mathbf{H}(\mathbf{r},t) = \varepsilon \frac{\partial \mathbf{E}(\mathbf{r},t)}{\partial t} + \sigma\,\mathbf{E}(\mathbf{r},t), \tag{4.22a}$$
$$\nabla \times \mathbf{E}(\mathbf{r},t) = -\mu \frac{\partial \mathbf{H}(\mathbf{r},t)}{\partial t}, \tag{4.22b}$$
$$\nabla \cdot \mathbf{E}(\mathbf{r},t) = 0, \tag{4.22c}$$
$$\nabla \cdot \mathbf{H}(\mathbf{r},t) = 0. \tag{4.22d}$$

We use the same approach to derive the wave equation for $\mathbf{E}(\mathbf{r},t)$ as in Section 4.1.3. Applying the curl operation $\nabla\times$ to (4.22b), using the vector identity $\nabla \times (\nabla \times \mathbf{E}(\mathbf{r},t)) = \nabla(\nabla \cdot \mathbf{E}(\mathbf{r},t)) - \Delta\mathbf{E}(\mathbf{r},t)$, and then using (4.22a) and (4.22c), leads to the wave equation for $\mathbf{E}(\mathbf{r},t)$ in the absorbing medium:

$$\Delta\mathbf{E}(\mathbf{r},t) - \varepsilon\mu \frac{\partial^2 \mathbf{E}(\mathbf{r},t)}{\partial t^2} - \mu\sigma \frac{\partial \mathbf{E}(\mathbf{r},t)}{\partial t} = 0. \tag{4.23}$$

Monochromatic waves in absorbing medium

Substituting the monochromatic waves (4.16) into the Maxwell equations for conductive medium (4.22) leads to:

$$\nabla \times \mathbf{H}_\omega(\mathbf{r}) = \mathrm{i}\omega\varepsilon\mathbf{E}_\omega(\mathbf{r}) + \sigma\mathbf{E}_\omega(\mathbf{r})\,, \tag{4.24a}$$
$$\nabla \times \mathbf{E}_\omega(\mathbf{r}) = -\mathrm{i}\omega\mu\mathbf{H}_\omega(\mathbf{r})\,, \tag{4.24b}$$
$$\nabla \cdot \mathbf{E}_\omega(\mathbf{r}) = 0, \tag{4.24c}$$
$$\nabla \cdot \mathbf{H}_\omega(\mathbf{r}) = 0. \tag{4.24d}$$

Using the complex permitivity

$$\tilde{\varepsilon} = \varepsilon - \mathrm{i}\frac{\sigma}{\omega} \tag{4.25}$$

leads to Maxwell equations in the same form as those for non-absorbing medium (4.17).

Applying the monochromatic waves (4.16) and using $\frac{\partial}{\partial t} \longrightarrow \mathrm{i}\omega$, the wave equation (4.23) transforms into the Helmholtz equation for absorbing medium:

$$\Delta\mathbf{E}_\omega + \tilde{\kappa}^2\mathbf{E}_\omega = 0, \tag{4.26}$$

where

$$\tilde{\kappa} = \omega\sqrt{\left(\varepsilon - \mathrm{i}\frac{\sigma}{\omega}\right)\mu} = \omega\sqrt{\tilde{\varepsilon}\mu} = \tilde{n}\frac{\omega}{c} = \tilde{n}\kappa_0, \tag{4.27}$$

Here $\tilde{\kappa}$, $\tilde{\varepsilon}$, and $\tilde{n}$ are the complex wavenumber, the complex permitivity and the complex refractive index, respectively.

The complex permitivity is

$$\tilde{\varepsilon} = \varepsilon - \mathrm{i}\frac{\sigma}{\omega} = \varepsilon_0\left(\varepsilon_r - \mathrm{i}\frac{\sigma}{\varepsilon_0\omega}\right) = \varepsilon_0\tilde{\varepsilon_r}. \tag{4.28}$$

Here $\tilde{\varepsilon_r}$ is the complex relative permitivity with the real ε_1 and imaginary ε_2 parts, for which stands:

$$\tilde{\varepsilon_r} = \varepsilon_1 - \mathrm{i}\varepsilon_2. \tag{4.29}$$

The complex refractive index is

$$\tilde{n} = \sqrt{\tilde{\varepsilon_r}} = \sqrt{\left(\varepsilon_r - \mathrm{i}\frac{\sigma}{\varepsilon_0\omega}\right)} = n - \mathrm{i}k, \tag{4.30}$$

with the real and imaginary part n and k, respectively.

Plane monochromatic waves in absorbing medium

Substituting the plane monochromatic waves (4.20) into (4.24), using the complex permitivity $\tilde{\varepsilon}$ (4.29) and applying $\nabla \longrightarrow -\mathrm{i}\boldsymbol{\kappa}$, the Maxwell equations for plane monochromatic wave in absorbing medium get the form:

$$\boldsymbol{\kappa} \times \mathbf{H}_0 = -\omega\varepsilon_0\tilde{\varepsilon_r}\mathbf{E}_0, \tag{4.31a}$$
$$\boldsymbol{\kappa} \times \mathbf{E}_0 = \omega\mu_0\mu_r\mathbf{H}_0, \tag{4.31b}$$
$$\boldsymbol{\kappa} \cdot \mathbf{E}_0 = 0, \tag{4.31c}$$
$$\boldsymbol{\kappa} \cdot \mathbf{H}_0 = 0. \tag{4.31d}$$

The complex amplitude of the plane monochromatic wave propagating along the z axis has then form:

$$\mathbf{E}_\omega = \mathbf{E}_0 \exp[-\mathrm{i}\tilde{\kappa}z] = \mathbf{E}_0 \exp[-\mathrm{i}\tilde{n}\kappa_0 z] = \mathbf{E}_0 \exp[-\mathrm{i}\kappa_0\Re(\tilde{n})\, z] \exp[-\kappa_0\Im(\tilde{n})\, z]\,, \tag{4.32}$$

where $\Re$ and $\Im$ denote the real and imaginary part, respectively

The intensity of the plane monochromatic wave in the absorbing medium then exponentially decreases with the distance d_z according to the Beer-Lambert law:

$$I\,(z) = I_0 \exp[-2\kappa_0\Im(\tilde{n})\, d_z] = I_0 \exp[-\alpha\, d_z]\,, \tag{4.33}$$

where $\alpha = 2\kappa_0\Im(\tilde{n})$ is the absorption coefficient. Note, that the Beer-Lambert law does not take into account effect of interfaces and interference in thin films.

Media are classified according to the imaginary part of their refractive index [$\Im\,(n)$] in the convention of monochromatic wave $\exp[\mathrm{i}\omega t]$ as follows:

$\Im\,(n) > 0$, $\Im\,(\tilde{\varepsilon}) > 0$ **:** absorbing medium,

$\Im\,(n) = 0$, $\Im\,(\tilde{\varepsilon}) = 0$ **:** non-absorbing medium,

$\Im\,(n) < 0$, $\Im\,(\tilde{\varepsilon}) < 0$ **:** gaining medium (for example lasers).

4.2 Light propagation in thin film systems

Although the solar cell concepts studied in this thesis are based on different textures (pyramidal texture for silicon heterojunction solar cells and randomly oriented silicon nanowires for radial junction solar cells), both these designs contain thin films. Therefore, a model of the propagation of light through multilayers is necessary to characterize and to optimize the architecture of studied samples.

4.2.1 Yeh's matrix formalism

There are several approaches to solve the propagation of electromagnetic waves in a thin film system. Yeh's approach [58, 59] is based on solving the Helmholtz equation derived from Maxwell equations (4.31) for plane monochromatic wave in each homogeneous medium (which can be in general anisotropic and absorbing i.e. described by complex tensor $\widehat{\varepsilon}_r$) of thin film system:

$$\kappa_0^2 \widehat{\varepsilon}_r \mathbf{E_0} - \boldsymbol{\kappa}^2 \mathbf{E_0} + \boldsymbol{\kappa} \left[\boldsymbol{\kappa} \cdot \mathbf{E_0} \right] = 0. \tag{4.34}$$

Here $\boldsymbol{\kappa}$ is the eigen-mode wave vector for which:

$$\boldsymbol{\kappa} = \kappa_x \mathbf{x} + \kappa_y \mathbf{y} + \kappa_z \mathbf{z} = \kappa_0 \left(N_x \mathbf{x} + N_y \mathbf{y} + N_z \mathbf{z} \right). \tag{4.35}$$

Consider a structure consisting of a system of K homogeneous anisotropic thin films situated between the semi-infinite substrate (medium index $K+1$) and the semi-infinite superstrate (medium index 0) as shown in Fig. 4.1. The coordinate system is chosen so that wave vector components are without loosing a generality as follows:

$$N_x = 0, \tag{4.36a}$$

$$N_y = \widehat{n}_0 \sin \varphi_0 \tag{4.36b}$$

where $\widehat{n}_0$ is in general the complex tensor of refractive index of superstrate (usually air) and φ_0 is the angle of incidence.

Then, the Helmholtz equation (4.34) for each medium can be written in the matrix form for all components of the electric field using the elements of complex relative permitivity tensor $\widehat{\varepsilon}_r$:

$$\underbrace{\begin{pmatrix} \tilde{\varepsilon}_{xx} - N_y^2 - N_z^2 & \tilde{\varepsilon}_{xy} & \tilde{\varepsilon}_{xz} \\ \tilde{\varepsilon}_{yx} & \tilde{\varepsilon}_{yy} - N_z^2 & \tilde{\varepsilon}_{yz} + N_y N_z \\ \tilde{\varepsilon}_{zx} & \tilde{\varepsilon}_{zy} + N_y N_z & \tilde{\varepsilon}_{zz} - N_y^2 \end{pmatrix}}_{\clubsuit} \begin{bmatrix} E_{0x} \\ E_{0y} \\ E_{0z} \end{bmatrix} = 0. \tag{4.37}$$

The system of linear equations (4.37) has the nontrivial solution following the condition:

$$\det\left(\clubsuit\right) = 0. \tag{4.38}$$

The equation (4.38) is called the characteristic equation. By solving this condition, we can find four solutions with corresponding propagating constants $N_{z,j}$, where $N_{z,1}$, $N_{z,3}$ are the forward modes propagation constants (representing the eigen-modes propagating downward the structure on Fig. 4.1), while $N_{z,2}$ and $N_{z,4}$ are the backward modes propagating constants (representing the eigen-modes propagating upward through the structure). The eigen-modes of polarization system

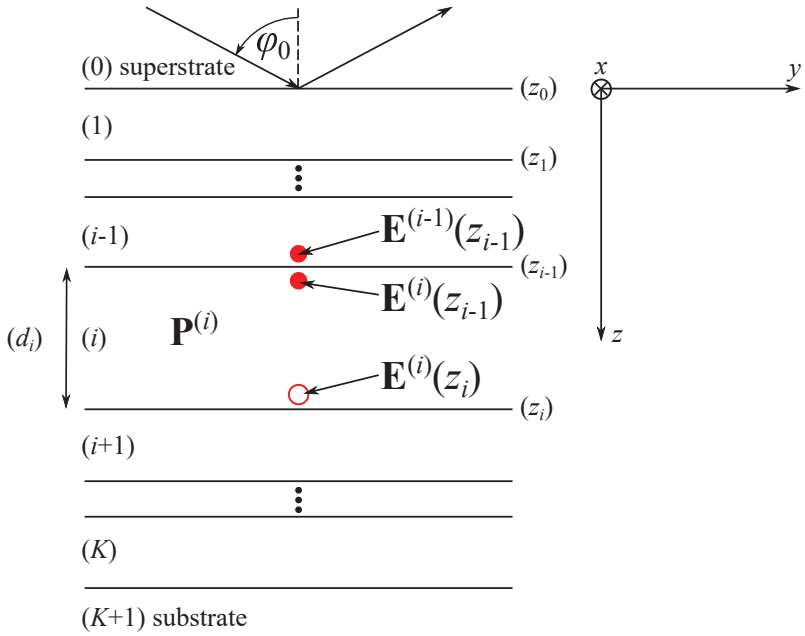

Figure 4.1 – Schematic representation of the thin film system consisting of K thin films situated between the substrate (medium $K+1$) and superstrate (medium 0). The interfaces between media are marked by z_i, where $i = 0, \ldots K$. Angle of incidence on the interface z_0 is φ_0 and the thickness of i-th layer is d_i. Matrix $\mathbf{P}^{(i)}$ is the propagation matrix of i-th layer and $\mathbf{E}$ denotes the vector of electric intensity.

are the states of polarization that are not changed when the wave is transmitted through the system.

In the isotropic medium, the complex relative permitivity tensor is substituted by:

$$\widehat{\varepsilon}_r = \begin{pmatrix} \tilde{\varepsilon}_{xx} & \tilde{\varepsilon}_{xy} & \tilde{\varepsilon}_{xz} \\ \tilde{\varepsilon}_{yx} & \tilde{\varepsilon}_{yy} & \tilde{\varepsilon}_{yz} \\ \tilde{\varepsilon}_{zx} & \tilde{\varepsilon}_{zy} & \tilde{\varepsilon}_{zz} \end{pmatrix} = \begin{pmatrix} \tilde{\varepsilon}_r & 0 & 0 \\ 0 & \tilde{\varepsilon}_r & 0 \\ 0 & 0 & \tilde{\varepsilon}_r \end{pmatrix}. \tag{4.39}$$

Substituting (4.39) into (4.37) and solving the characteristic equation (4.38) give the propagation constants of eigen-modes:

$$N_{z,1} = N_{z,3} = \sqrt{\tilde{\varepsilon}_r - N_y^2} = \tilde{n}\cos\varphi, \tag{4.40a}$$

$$N_{z,2} = N_{z,4} = -\sqrt{\tilde{\varepsilon}_r - N_y^2} = -\tilde{n}\cos\varphi, \tag{4.40b}$$

where $\tilde{\varepsilon}_r$ and $\tilde{n}$ are the complex relative permitivity and the complex refractive index of the medium, and φ is the propagation angle in the medium.

Each eigen-mode can be written in the form:

$$\mathbf{E}_{0,j} = A_j \mathbf{e}_j, \tag{4.41a}$$

$$\mathbf{H}_{0,j} = \frac{1}{\omega\mu_0}\boldsymbol{\kappa} \times \mathbf{E}_{0,j} = \sqrt{\frac{\varepsilon_0}{\mu_0}}\mathbf{h}_j, \tag{4.41b}$$

where A_j is the amplitude of the j-th eigen-mode and $\mathbf{e}_j$, $\mathbf{h}_j$ are the complex eigen-polarization vectors for electric and magnetic field of each mode, respectively.

Eigen-mode vectors representing the *s*- and *p*-polarized waves, can be written in the form:

$$\mathbf{e_1} = \begin{bmatrix} 1 \\ 0 \\ 0 \end{bmatrix}, \qquad \mathbf{h_1} = \begin{bmatrix} 0 \\ N_{z,1} \\ -N_y \end{bmatrix}, \tag{4.42a}$$

$$\mathbf{e_2} = \begin{bmatrix} 1 \\ 0 \\ 0 \end{bmatrix}, \qquad \mathbf{h_2} = \begin{bmatrix} 0 \\ N_{z,2} \\ -N_y \end{bmatrix}, \tag{4.42b}$$

$$\mathbf{e_3} = \frac{1}{\sqrt{\tilde{\varepsilon}_r}} \begin{bmatrix} 0 \\ N_{z,3} \\ -N_y \end{bmatrix}, \qquad \mathbf{h_3} = \begin{bmatrix} -\sqrt{\tilde{\varepsilon}_r} \\ 0 \\ 0 \end{bmatrix}, \tag{4.42c}$$

$$\mathbf{e_4} = \frac{1}{\sqrt{\tilde{\varepsilon}_r}} \begin{bmatrix} 0 \\ -N_{z,4} \\ N_y \end{bmatrix}, \qquad \mathbf{h_4} = \begin{bmatrix} \sqrt{\tilde{\varepsilon}_r} \\ 0 \\ 0 \end{bmatrix}. \tag{4.42d}$$

Here (4.42a) and (4.42b) represent the s-polarized waves propagating downwards and upwards, respectively, while (4.42c) and (4.42d) correspond to the p-polarized waves propagating downwards and upwards through the structure, respectively.

The eigen-modes and their propagation constants will be used to solve the propagation of light in the multi-layer system shown in Fig. 4.1. First, the formula solving the propagation of light though a layer will be described. Then, the principle of solving the transmission of light through an interface between two media using the boundary conditions will be introduced. Finally, the formalism solving the light propagation in multi-layer system will be derived.

Propagation through a layer

Propagation of light through an i-th layer formed by a homogeneous medium must be solved using the vector of amplitudes $\mathbf{A}^{(i)}$. The propagation of light from the interface (z_{i-1}) to the interface (z_i) (see Fig. 4.1) is described by the propagation matrix $\mathbf{P}^{(i)}$:

$$\mathbf{P}^{(i)} = \begin{pmatrix} \exp\left[-\mathrm{i}\kappa_0 N_{z1}^{(i)} d_i\right] & 0 & 0 & 0 \\ 0 & \exp\left[-\mathrm{i}\kappa_0 N_{z2}^{(i)} d_i\right] & 0 & 0 \\ 0 & 0 & \exp\left[-\mathrm{i}\kappa_0 N_{z3}^{(i)} d_i\right] & 0 \\ 0 & 0 & 0 & \exp\left[-\mathrm{i}\kappa_0 N_{z4}^{(i)} d_i\right] \end{pmatrix}, \tag{4.43}$$

where $N_{z,j},\ j = 1, \ldots, 4$ are the propagation constants in z-direction defined in (4.40) and d_i is the thickness of the i-th layer. The vector of amplitudes is then transformed according to the relation:

$$\mathbf{A}^{(i)}\left(z_i\right) = \mathbf{P}^{(i)}\mathbf{A}^{(i)}\left(z_{i-1}\right) \tag{4.44}$$

Boundary conditions

The transmission of light through an interface z_{i-1} (see Fig. 4.1) is solved using boundary conditions of Maxwell equations (4.3). Tangential components of the electric and magnetic field are continuous at the interface between two dielectric media $(i-1)$ and i:

$$\mathbf{E}_x^{(i-1)} = \mathbf{E}_x^{(i)}, \qquad \mathbf{E}_y^{(i-1)} = \mathbf{E}_y^{(i)}, \tag{4.45a}$$

$$\mathbf{H}_x^{(i-1)} = \mathbf{H}_x^{(i)}, \qquad \mathbf{H}_y^{(i-1)} = \mathbf{H}_y^{(i)}. \tag{4.45b}$$

Using the eigen-modes expression (4.41), the boundary conditions (4.45) can be written as:

$$\sum_{j=1}^{4} A_j^{(i-1)} \mathbf{e}_{xj}^{(i-1)} = \sum_{j=1}^{4} A_j^{(i)} \mathbf{e}_{xj}^{(i)}, \tag{4.46a}$$

$$\sum_{j=1}^{4} A_j^{(i-1)} \mathbf{h}_{yj}^{(i-1)} = \sum_{j=1}^{4} A_j^{(i)} \mathbf{h}_{yj}^{(i)}, \tag{4.46b}$$

$$\sum_{j=1}^{4} A_j^{(i-1)} \mathbf{e}_{yj}^{(i-1)} = \sum_{j=1}^{4} A_j^{(i)} \mathbf{e}_{yj}^{(n)}, \tag{4.46c}$$

$$\sum_{j=1}^{4} A_j^{(i-1)} \mathbf{h}_{xj}^{(i-1)} = \sum_{j=1}^{4} A_j^{(i)} \mathbf{h}_{xj}^{(i)}. \tag{4.46d}$$

The boundary conditions for eigen-modes (4.46) can be written in more compact form using the matrix representation:

$$\mathbf{D}^{(i-1)}\mathbf{A}^{(i-1)} = \mathbf{D}^{(i)}\mathbf{A}^{(i)}, \tag{4.47}$$

where $\mathbf{A}^{(i)}$ is the vector of amplitudes for the i-th layer and $\mathbf{D}^{(i)}$ is the dynamic matrix of the same layer. They are in form:

$$\mathbf{A}^{(i)} = \begin{bmatrix} A_1^{(i)} \\ A_2^{(i)} \\ A_3^{(i)} \\ A_4^{(i)} \end{bmatrix}, \tag{4.48}$$

$$\mathbf{D}^{(i)} = \begin{pmatrix} \mathbf{e}_{x1}^{(i)} & \mathbf{e}_{x2}^{(i)} & \mathbf{e}_{x3}^{(i)} & \mathbf{e}_{x4}^{(i)} \\ \mathbf{h}_{y1}^{(i)} & \mathbf{h}_{y2}^{(i)} & \mathbf{h}_{y3}^{(i)} & \mathbf{h}_{y4}^{(i)} \\ \mathbf{e}_{y1}^{(i)} & \mathbf{e}_{y2}^{(i)} & \mathbf{e}_{y3}^{(i)} & \mathbf{e}_{y4}^{(i)} \\ \mathbf{h}_{x1}^{(i)} & \mathbf{h}_{x2}^{(i)} & \mathbf{h}_{x3}^{(i)} & \mathbf{h}_{x4}^{(i)} \end{pmatrix}. \tag{4.49}$$

Columns of the matrix $\mathbf{D}^{(i)}$ represent four different eigen-modes, while rows contain tangential components of eigen-polarization vectors.

Substituting the eigen-modes from (4.42), the dynamic matrix for i-th isotropic layer has the form:

$$\mathbf{D}^{(i)} = \begin{pmatrix} 1 & 1 & 0 & 0 \\ \sqrt{\varepsilon^{(i)} - N_y^2} & -\sqrt{\varepsilon^{(i)} - N_y^2} & 0 & 0 \\ 0 & 0 & \frac{1}{\sqrt{\varepsilon^{(i)}}}\sqrt{\varepsilon^{(i)} - N_y^2} & \frac{1}{\sqrt{\varepsilon^{(i)}}}\sqrt{\varepsilon^{(i)} - N_y^2} \\ 0 & 0 & -\sqrt{\varepsilon^{(i)}} & \sqrt{\varepsilon^{(i)}} \end{pmatrix}, \tag{4.50}$$

where $\tilde{\varepsilon}_r$ is substituted by $\varepsilon^{(i)}$ which is the complex relative permitivity of the medium and N_y is the propagation constant in y-direction defined by (4.36b). We can see that the dynamic matrix is block-diagonal for isotropic case. The top left block of the matrix represents the s-polarization and the bottom right block corresponds to the p-polarization.

Propagation in multi-layers

To obtain the relation between amplitude $\mathbf{A}^{(i-1)}$ at the interface (z_{i-1}) and amplitude $\mathbf{A}^{(i+1)}$ at the interface (z_i) the equations (4.47) and (4.44) are combined, resulting in:

$$\mathbf{A}^{(i-1)}(z_{i-1}) = \left[\mathbf{D}^{(i-1)}\right]^{-1} \underbrace{\mathbf{D}^{(i)}\left[\mathbf{P}^{(i)}\right]^{-1}\left[\mathbf{D}^{(i)}\right]^{-1}}_{\mathbf{T}^{(i)}} \mathbf{D}^{(i+1)}\mathbf{A}^{(i+1)}(z_i), \tag{4.51}$$

where $\mathbf{T}^{(i)}$ is the transfer matrix of the i-th layer. The above formula (4.51) can be generalized for thin film system consisting of $(K+1)$ media as follows:

$$\mathbf{A}^{(0)} = \underbrace{\left[\mathbf{D}^{(0)}\right]^{-1} \prod_{i=1}^{K} \left\{\mathbf{D}^{(i)} \left[\mathbf{P}^{(i)}\right]^{-1} \left[\mathbf{D}^{(i)}\right]^{-1}\right\} \mathbf{D}^{(K+1)}}_{\mathbf{M}} \mathbf{A}^{(K+1)}. \tag{4.52}$$

The relation between the amplitude $\mathbf{A}^{(0)}$ in the superstrate and the amplitude $\mathbf{A}^{(K+1)}$ in the substrate is then defined by the total matrix of the thin film system:

$$\mathbf{M} = \begin{pmatrix} \mathsf{M}_{11} & \mathsf{M}_{12} & \mathsf{M}_{13} & \mathsf{M}_{14} \\ \mathsf{M}_{21} & \mathsf{M}_{22} & \mathsf{M}_{23} & \mathsf{M}_{24} \\ \mathsf{M}_{31} & \mathsf{M}_{32} & \mathsf{M}_{33} & \mathsf{M}_{34} \\ \mathsf{M}_{41} & \mathsf{M}_{42} & \mathsf{M}_{43} & \mathsf{M}_{44} \end{pmatrix}. \tag{4.53}$$

4.2.2 Optical intensity and power

The flow of electromagnetic power is governed by the real Poynting vector $\mathbf{S}$ defined as the cross product of the real parts of complex vectors of electromagnetic field [56]:

$$\mathbf{S} = \Re\left(\mathbf{E}\right) \times \Re\left(\mathbf{H}\right). \tag{4.54}$$

The cross product in (4.54) determines the direction of the power flow to be perpendicular to both $\Re\left(\mathbf{E}\right)$ and $\Re\left(\mathbf{H}\right)$. In the isotropic medium, the Poynting vector $\mathbf{S}$ is parallel to the wave vector $\boldsymbol{\kappa}$ which means that the power flows in the direction normal to the wavefronts.

The optical intensity I is defined as the power flow through a unit area normal to the vector $\mathbf{S}$. This corresponds to the magnitude of the time-averaged Poynting vector:

$$I = \left|\langle \mathbf{S} \rangle\right| = \left|\langle \Re\left(\mathbf{E}\right) \times \Re\left(\mathbf{H}\right) \rangle\right|. \tag{4.55}$$

Substituting the monochromatic wave (4.16) into (4.54) leads to the expression:

$$\begin{gathered} \mathbf{S} = \Re\left\{\mathbf{E}_\omega \exp(\mathrm{i}\omega t)\right\} \times \Re\left\{\mathbf{H}_\omega \exp(\mathrm{i}\omega t)\right\} = \\ = \frac{1}{4}\left[\mathbf{E}_\omega \times \mathbf{H}_\omega^* + \mathbf{E}_\omega^* \times \mathbf{H}_\omega + \mathbf{E}_\omega \times \mathbf{H}_\omega \exp(\mathrm{i}2\omega t) + \mathbf{E}_\omega^* \times \mathbf{H}_\omega^* \exp(-\mathrm{i}2\omega t)\right], \end{gathered} \tag{4.56}$$

where * denotes the complex conjugate.

Further, terms containing $\exp(\mathrm{i}2\omega t)$ and $\exp(-\mathrm{i}2\omega t)$ are removed by the time-averaging since , leading to [56]:

$$\langle \mathbf{S} \rangle = \frac{1}{4}\left(\mathbf{E}_\omega \times \mathbf{H}_\omega^* + \mathbf{E}_\omega^* \times \mathbf{H}_\omega\right) = \frac{1}{2}\left(\mathbf{S}_\omega + \mathbf{S}_\omega^*\right) = \Re\left\{\mathbf{S}_\omega\right\}, \tag{4.57}$$

where $\mathbf{S}_\omega$ is the complex Poynting vector:

$$\mathbf{S}_\omega = \frac{1}{2}\mathbf{E}_\omega \times \mathbf{H}^*_\omega. \tag{4.58}$$

The optical intensity is then the magnitude of the vector $\Re\{\mathbf{S}_\omega\}$:

$$I = |\langle \mathbf{S} \rangle| = |\Re\{\mathbf{S}_\omega\}|. \tag{4.59}$$

The intensity of the plane monochromatic wave in isotropic medium is [56]:

$$I = |\Re\{\mathbf{S}_\omega\}| = \frac{1}{2}|E_0 H_0^*| = \frac{|E_0|^2}{2\eta}, \tag{4.60}$$

where E_0, H_0 are the magnitudes of complex envelopes of electric and magnetic field, respectively, η is the impedance of the medium:

$$\eta = \frac{E_0}{H_0} = \sqrt{\frac{\mu}{\varepsilon}} = \frac{\eta_0}{n}, \tag{4.61}$$

and $\eta_0 = \sqrt{\frac{\mu_0}{\varepsilon_0}}$ is the impedance of free space.

The Poynting vector $\mathbf{S}$ can be used to calculate the absorption in thin film systems, since it takes into account also the effects of interfaces and interferences in thin films, in contrast to the Beer-Lambert law (4.33) mentioned in Section 4.1.4. The absorptance in each layer of the structure is calculated as a difference of the z-components of Poynting vector at the interfaces of that layer.

4.2.3 Reflection and transmission of light

Light reflected from or transmitted through a sample can be characterized by amplitude reflection and transmission coefficients and by the reflectance and transmittance. The reflection and transmission coefficients r and t are defined as the ratios between complex amplitudes of reflected or transmitted light to the incident one. Using the boundary condition for continuity of tangential components of the electric and magnetic field $\mathbf{E}$ and $\mathbf{H}$, the amplitude coefficients of the single interface have for eigen-modes represented by s- and p-polarizations the

following form:

$$r_s = \frac{E_{rs}}{E_{is}} = \frac{n_i \cos\varphi_i - n_t \cos\varphi_t}{n_i \cos\varphi_i + n_t \cos\varphi_t}, \tag{4.62a}$$

$$r_p = \frac{E_{rp}}{E_{ip}} = \frac{n_t \cos\varphi_i - n_i \cos\varphi_t}{n_t \cos\varphi_i + n_i \cos\varphi_t}, \tag{4.62b}$$

$$t_s = \frac{E_{ts}}{E_{is}} = \frac{2n_i \cos\varphi_i}{n_i \cos\varphi_i + n_t \cos\varphi_t}, \tag{4.62c}$$

$$t_p = \frac{E_{tp}}{E_{ip}} = \frac{2n_i \cos\varphi_i}{n_t \cos\varphi_i + n_i \cos\varphi_t}. \tag{4.62d}$$

Subscripts s and p represent the type of polarization, while the subscripts r, t, and i stand for reflected, transmitted, and incident wave, respectively. The refractive index of the medium above the interface is n_i, while the refractive index of medium below the interface is n_t. Similarly, φ_i is the angle of incidence on the interface and φ_t is the angle of refraction to the medium below the interface.

The power reflectance R and transmittance T of a sample are defined as the ratios of power flow (along a direction normal to the boundary) of the reflected and transmitted waves to that of the incident one. Using the z-components of Poynting vector the power reflectance and transmittance at a single interface have the form:

$$R_m = \left| \frac{\langle \mathsf{S}_{rm} \rangle_z}{\langle \mathsf{S}_{im} \rangle_z} \right|, \tag{4.63a}$$

$$T_m = \left| \frac{\langle \mathsf{S}_{tm} \rangle_z}{\langle \mathsf{S}_{im} \rangle_z} \right|, \tag{4.63b}$$

where subscript m denotes the type of polarization (s or p), while the subscripts r, t, and i stand for reflected, transmitted, and incident wave, respectively.

In the case of a single interface, the power reflectance and transmittance to a non-absorbing medium can be expressed using the amplitude reflection and transmission coefficients (4.62) as follows:

$$R_s = |r_s|^2, \tag{4.64a}$$

$$R_p = |r_p|^2, \tag{4.64b}$$

$$T_s = \left(\frac{n_t \cos\varphi_t}{n_i \cos\varphi_i} \right) |t_s|^2, \tag{4.64c}$$

$$T_p = \left(\frac{n_t \cos\varphi_t}{n_i \cos\varphi_i} \right) |t_p|^2. \tag{4.64d}$$

The reflectance and transmittance of unpolarized light which has been measured using spectrophotometer described in Section 3.1 are in the form:

$$R = \frac{1}{2}\left(R_s + R_p\right), \tag{4.65a}$$

$$T = \frac{1}{2}\left(T_s + T_p\right), \tag{4.65b}$$

In the case of thin-film system characterized by the total matrix **M** defined by (4.53), the reflection coefficients are defined using the elements of this matrix. For eigen-modes in the medium (0) represented by s- and p-polarized waves according to (4.42), the refection coefficients are:

$$r_{12} = r_{ss} = \left.\frac{A_2^{(0)}}{A_1^{(0)}}\right|_{A_3^{(0)}=0} = \frac{\mathsf{M}_{21}\mathsf{M}_{33} - \mathsf{M}_{23}\mathsf{M}_{31}}{\mathsf{M}_{11}\mathsf{M}_{33} - \mathsf{M}_{13}\mathsf{M}_{31}}, \tag{4.66a}$$

$$r_{14} = r_{sp} = \left.\frac{A_4^{(0)}}{A_1^{(0)}}\right|_{A_3^{(0)}=0} = \frac{\mathsf{M}_{41}\mathsf{M}_{33} - \mathsf{M}_{43}\mathsf{M}_{31}}{\mathsf{M}_{11}\mathsf{M}_{33} - \mathsf{M}_{13}\mathsf{M}_{31}}, \tag{4.66b}$$

$$r_{32} = -r_{ps} = \left.\frac{A_2^{(0)}}{A_3^{(0)}}\right|_{A_1^{(0)}=0} = \frac{\mathsf{M}_{11}\mathsf{M}_{23} - \mathsf{M}_{13}\mathsf{M}_{21}}{\mathsf{M}_{11}\mathsf{M}_{33} - \mathsf{M}_{13}\mathsf{M}_{31}}, \tag{4.66c}$$

$$r_{34} = -r_{pp} = \left.\frac{A_4^{(0)}}{A_3^{(0)}}\right|_{A_1^{(0)}=0} = \frac{\mathsf{M}_{11}\mathsf{M}_{43} - \mathsf{M}_{13}\mathsf{M}_{41}}{\mathsf{M}_{11}\mathsf{M}_{33} - \mathsf{M}_{13}\mathsf{M}_{31}}. \tag{4.66d}$$

For example, coefficient r_{ps} represents reflection of p-polarized light ($A_2^{(0)}$) generated by the incident s-polarized light ($A_1^{(0)}$) when there is no incident p-polarized wave ($A_3^{(0)} = 0$).

In the case of isotropic system, the resulting **M** matrix is block-diagonal, because of block-diagonal dynamic matrix $\mathbf{D}$ of each medium [see (4.50)] and diagonal propagation matrix $\mathbf{P}$. Zero elements in off-diagonal blocks leads to $r_{sp} = r_{ps} = 0$ meaning there is no conversion between s- and p-polarization. The **M** matrix can be separated into two independent matrices $\mathbf{M}_s$ and $\mathbf{M}_p$, each one formed from a respective diagonal block at the **M** matrix.

The transmission coefficients are defined using the elements of M matrix char-

acterizing a thin film system as follows:

$$t_{11} = t_{ss} = \left.\frac{A_1^{(K+1)}}{A_1^{(0)}}\right|_{A_3^{(0)}=0} = \frac{\mathsf{M}_{33}}{\mathsf{M}_{11}\mathsf{M}_{33} - \mathsf{M}_{13}\mathsf{M}_{31}}, \tag{4.67a}$$

$$t_{13} = t_{sp} = \left.\frac{A_3^{(K+1)}}{A_1^{(0)}}\right|_{A_3^{(0)}=0} = \frac{-\mathsf{M}_{31}}{\mathsf{M}_{11}\mathsf{M}_{33} - \mathsf{M}_{13}\mathsf{M}_{31}}, \tag{4.67b}$$

$$t_{31} = t_{ps} = \left.\frac{A_1^{(K+1)}}{A_3^{(0)}}\right|_{A_1^{(0)}=0} = \frac{-\mathsf{M}_{13}}{\mathsf{M}_{11}\mathsf{M}_{33} - \mathsf{M}_{13}\mathsf{M}_{31}}, \tag{4.67c}$$

$$t_{33} = t_{pp} = \left.\frac{A_3^{(K+1)}}{A_3^{(0)}}\right|_{A_1^{(0)}=0} = \frac{\mathsf{M}_{11}}{\mathsf{M}_{11}\mathsf{M}_{33} - \mathsf{M}_{13}\mathsf{M}_{31}}, \tag{4.67d}$$

provided that eigen-modes are in the media (0) and $(K+1)$ represented by s- and p-polarized waves according to (4.42). Similarly as for reflection coefficients, the subscripts sp and ps of the transmission coefficients refer to conversion between s- and p-polarization after transmission through the thin film system. For the isotropic system, these coefficients are zero, since there is no polarization conversion.

4.3 Principles of spectroscopic ellipsometry and Mueller matrix polarimetry

The ellipsometric techniques such as spectroscopic ellipsometry and Mueller matrix polarimetry are fast, non-destructive optical measurements with a wide application area. They are extremely sensitive to the properties of interfaces and thin films (thickness sensitivity up to about 0.01 nm). They can provide information about the optical constants (complex refractive index or complex dielectric function including absorption coefficient) of investigated samples as well as about the sample structure (film thicknesses, surface roughness, composition of material).

Measurements in different spectral ranges enable us to obtain even more specific information about band structure or free-carriers. Measurements in ultraviolet/visible region enable characterization of interband transitions and determination of energy bandgap. Also other properties connected with the band structure such as alloy composition, material phase or grain size can be analyzed. Measurements in the infrared region are sensitive to the absorption by free charge carriers of low concentrations thus electrical properties including carrier mobility, carrier

concentration and conductivity can be studied. Moreover, the ellipsometric measurements can be performed in-situ during the sample preparation to monitor the evolution of sample properties in real time (initial growth process, changes in composition, reaction rate during processing, etc.) and to perform a process control [60].

The essential principle of ellipsometric methods is the measurement of the change in light polarization after the interaction with the sample. The measurement can be performed in both, the reflection or transmission configuration. We will describe the reflection configuration in more detail in the following text, since it corresponds to the measurements in this thesis. A standard ellipsometry is typically used to characterize optically isotropic bulk and layered materials. More advanced Mueller matrix ellipsometry (also called polarimetry) enable accurate sample characterization including anisotropy and depolarization.

All types of ellipsometric measurements are indirect methods which means that data analysis requires construction of optical model. The more complex the studied sample is, the more sophisticated model has to be used.

4.3.1 Principles of spectroscopic ellipsometry

The spectroscopic ellipsometry allows to determine two independent values Ψ and Δ (called ellipsometric angles) as functions of wavelength or photon energy of light. The ellipsometric angles Ψ and Δ are defined from the ratio of the complex reflection coefficients as follows [60–62]:

$$\frac{r_p}{r_s} = \tan\Psi \exp(\mathrm{i}\Delta)\,, \tag{4.68}$$

where

$$r_p = |r_p| \exp(\mathrm{i}\delta_p)\,, \tag{4.69a}$$
$$r_s = |r_s| \exp(\mathrm{i}\delta_s) \tag{4.69b}$$

are the complex reflection coefficients for p- and s-polarization, respectively (for more detailed information see Section 4.2.3). Thus $\tan\Psi$ and Δ correspond to the amplitude ratio and the phase difference between the p- and s-polarized light reflected from the sample [61]:

$$\tan\Psi = \frac{|r_p|}{|r_s|}, \tag{4.70a}$$
$$\Delta = \delta_p - \delta_s, \tag{4.70b}$$

where δ_p and δ_s are the absolute phase changes of the p- and s-polarized waves [62].

In the phase-modulated ellipsometry, which is used for the material characterization in this thesis (see Section 3.2.1), the harmonic analysis of the measured signal is carried out to obtain the ellipsometric values I_S and I_C [61]. These values are connected with the ellipsometric angles Ψ and Δ through the relations [63, p.491]:

$$I_S = \sin(2\Psi)\sin\Delta, \tag{4.71a}$$
$$I_C = \sin(2\Psi)\cos\Delta. \tag{4.71b}$$

In the absence of the depolarization, the interaction of light with a sample can be described by Jones formalism using the 2×2 Jones matrix $\mathbf{J}$ [60, 61]:

$$\mathbf{E}_0^{out} = \mathbf{J}\mathbf{E}_0^{in}, \tag{4.72a}$$
$$\mathbf{J} = \begin{bmatrix} J_{xx} & J_{xy} \\ J_{yx} & J_{yy} \end{bmatrix}, \tag{4.72b}$$

where superscripts in and out refer to the incident and outgoing light, respectively. In the case of light reflection from an isotropic sample, the Jones matrix can be expressed using the reflection coefficients from (4.62):

$$\mathbf{J} = \begin{bmatrix} r_p & 0 \\ 0 & r_s \end{bmatrix}, \tag{4.73}$$

while for the reflection from anisotropic sample, the Jones matrix has the more general form using the reflection coefficient from (4.66):

$$\mathbf{J} = \begin{bmatrix} r_{pp} & r_{ps} \\ r_{sp} & r_{ss} \end{bmatrix}. \tag{4.74}$$

4.3.2 Principles of Mueller matrix polarimetry

In Mueller matrix polarimetry the polarization changes induced by the studied sample on selected input polarization states represented by the Stokes vector S are measured [61]. The Stokes vector is defined as:

$$\mathbf{S} = \begin{bmatrix} S_0 \\ S_1 \\ S_2 \\ S_3 \end{bmatrix} = \begin{bmatrix} I_p + I_s \\ I_p - I_s \\ I_{+45^\circ} - I_{-45^\circ} \\ I_L - I_R \end{bmatrix}, \tag{4.75}$$

where I_p, I_s, I_{+45°, I_{-45°, I_L, and I_R are the intensities of p- and s-polarized light, linearly polarized light at $+45^\circ$ and -45° and left- and right-circular polarized

light, respectively. The Stokes vector is thus defined by directly measurable light intensities. The degree of light polarization ρ_S can be obtained from Stokes vector [61]:

$$\rho_S = \frac{\sqrt{S_1^2 + S_2^2 + S_3^2}}{S_0} \tag{4.76}$$

and it varies between 0 for totally depolarized and 1 for totally polarized states.

The transformation of Stokes vector after the interaction with the sample is described by the 4×4 Mueller matrix $\mathbf{M}$:

$$\mathbf{S}^{out} = \mathbf{M}\mathbf{S}^{in}, \tag{4.77a}$$

$$\mathbf{M} = \begin{pmatrix} M_{11} & M_{12} & M_{13} & M_{14} \\ M_{21} & M_{22} & M_{23} & M_{24} \\ M_{31} & M_{32} & M_{33} & M_{34} \\ M_{41} & M_{42} & M_{43} & M_{44} \end{pmatrix}, \tag{4.77b}$$

where superscripts in and out refer to the incident and outgoing light, respectively. This approach to description of light-polarization properties is known as Stokes-Mueller formalism and it is the most general representation which can adequately handle any polarization states [61].

The depolarizing properties of the sample are quantified using depolarization index P_D which can be determined from the sample Mueller matrix according to the relation [61]:

$$P_D = \sqrt{\frac{\sum_{i,j} M_{i,j}^2 - M_{11}^2}{3M_{11}^2}}. \tag{4.78}$$

The depolarization index is 0 for a perfect depolarizer and 1 for non-depolarizing samples.

In the case of non-depolarizing samples, the Stokes-Muller and Jones formalisms are equivalent [64] and a corresponding Mueller matrix can be calculated directly from Jones matrix [63]:

$$\mathbf{M} = \mathbf{A}\,(\mathbf{J} \otimes \mathbf{J}^*)\,\mathbf{A}^{-1}, \tag{4.79}$$

where the symbol $\otimes$ denotes the Kronecker product, matrix $\mathbf{J} \otimes \mathbf{J}^*$ is called the coherence matrix, and $\mathbf{A}$ is defined as:

$$\mathbf{A} = \begin{pmatrix} 1 & 0 & 0 & 1 \\ 1 & 0 & 0 & -1 \\ 0 & 1 & 1 & 0 \\ 0 & -\mathrm{i} & \mathrm{i} & 0 \end{pmatrix}. \tag{4.80}$$

Therefor, Mueller matrix of isotropic non-depolarizing samples is block-diagonal and its elements are related to the ellipsometric angles Ψ and Δ [61]:

$$\mathbf{M} = \begin{pmatrix} 1 & -\cos(2\Psi) & 0 & 0 \\ -\cos(2\Psi) & 1 & 0 & 0 \\ 0 & 0 & \sin(2\Psi)\cos\Delta & \sin(2\Psi)\sin\Delta \\ 0 & 0 & -\sin(2\Psi)\sin\Delta & \sin(2\Psi)\cos\Delta \end{pmatrix}. \tag{4.81}$$

The elements M_{33}, M_{43} of Mueller matrix of isotropic non-depolarizing sample thus correspond directly to the values I_C, $-I_S$ (4.71) measured by spectroscopic ellipsometry.

4.3.3 Data analysis

Due to the indirect nature of ellipsometric techniques the construction of optical model is necessary to obtain information of interest from raw measured data. The layered optical models defined by optical constants and thicknesses of layers are typically used for the interpretation of ellipsometric data.

Using the theory described in Section 4.2.1, the total matrix **M** of the system is build, the complex reflection coefficients are determined and ellipsometric angles are extracted. Then, theoretical values of I_S and I_C of the modeled structure are obtained using relations (4.71). We look for the adequate parameters of the model (optical constants and layer thicknesses) to minimize the difference between the modeled and measured values of I_S and I_C. In other words, we need to adjust the model parameters to make the modeled data to "fit" the measured one. The fitting process is usually performed by numerical algorithm which searches for the best-fitting values of the model parameters. The quality of the fit is evaluated by the figure of merit called fitting error function. In this thesis, we use least-square algorithm based on minimization of fitting error function χ^2 defined as:

$$\chi^2 = \frac{1}{(2M-N-1)} \cdot \left(\sum_{k=1}^{M} \frac{\left(I_{S,k}^{meas} - I_{S,k}^{mod}\right)^2}{\left(\sigma_{I_{S,k}}\right)^2} + \sum_{k=1}^{M} \frac{\left(I_{C,k}^{meas} - I_{C,k}^{mod}\right)^2}{\left(\sigma_{I_{C,k}}\right)^2} \right). \tag{4.82}$$

Here superscripts $meas$ and mod stand for the measured and modelled values, respectively. $\sigma_{i,k}$ represents the estimated measurement error. The sum is calculated over the measured spectral interval. M stands for the number of spectral points and N is the number of fitting parameters.

The process of interpretation of data measured by the Mueller matrix polarimetry is similar. However, the elements of Mueller matrix are used in the fitting process instead of the values I_S and I_C this time.

Optical functions of materials are essential parameters required for optical models. When the optical functions of desired material are not known, they can

be described using models for dielectric functions as introduced in the following text.

Models of dielectric functions

The required dielectric function of material of interest can be modeled directly using various phenomenological models. An appropriate model has to be selected with respect to the optical properties and nature of the material. Sometimes, a combination of several terms has to be used for modeling the dielectric function in a whole studied spectral range. Dielectric function models used for materials presented in this thesis are introduced below.

Cauchy transparent model expresses an empirical relationship between the refractive index and wavelength of light for a transparent, non-absorbing material. In this thesis it was used in the form:

$$n(\lambda) = A_C + \frac{B_C \cdot 10^4}{\lambda^2} + \frac{C_C \cdot 10^9}{\lambda^4}, \quad k = 0, \tag{4.83}$$

where n and k are the real and imaginary parts of refractive index, λ is the wavelength, and A_C, B_C, C_C are fitting parameters.

Drude model is usually applied to model absorptions by free electrons in metals or free carriers in conductive oxides and heavily doped semiconductors. The complex dielectric function is expressed as:

$$\tilde{\varepsilon}(E) = \varepsilon_\infty - \frac{E_p^2}{E^2 - \mathrm{i}E\Gamma_D}, \tag{4.84}$$

where ε_∞ is the high-frequency dielectric constant, E is the photon energy, E_p is the plasma energy, and Γ_D is the collision energy of free carriers.

Lorentz damped harmonic oscillator assumes a physical model in which negatively charged electron is bound to a positively charged atomic nucleus. The expression for Lorentz oscillator is obtained by solving damped oscillations of the electron forced by the external periodic electric field [60]. Dielectric functions of real materials are often modeled using a sum of several Lorentz damped harmonic oscillators:

$$\tilde{\varepsilon}(E) = \varepsilon_\infty + \sum_{j=1} \frac{A_{L,j} E_{L,0,j}^2}{E_{L,0,j}^2 - E^2 + \mathrm{i}\gamma_{L,j} E}, \tag{4.85}$$

where ε_∞ is the constant term describing contributions of high energy transitions, E is the photon energy and parameters $A_{L,j}$, $E_{L,0,j}$, and $\gamma_{L,j}$ are the amplitude, resonant energy and damping of the j-th Lorentz oscillator.

Tauc-Lorentz model is used to model dielectric functions of amorphous materials [65–67] and in combination with Drude model (4.84) can be applied to model also transparent conductive oxides [68, 69]. The Tauc-Lorentz model was deduced from Lorentz model of damped harmonic oscillator (4.85) by extension of Tauc gap [70] describing better the unique bandgap of amorphous materials. The imaginary part ε_2 of the complex dielectric function has an asymmetric shape [65, 66]:

$$\varepsilon_2(E) = \begin{cases} \frac{1}{E}\frac{A_L E_{L,0} C (E-E_g)^2}{\left(E^2-E_{L,0}^2\right)^2+C^2E^2} & \text{for } E > E_g \\ 0 & \text{for } E < E_g \end{cases}, \tag{4.86}$$

where E is the photon energy, A_L, $E_{L,0}$, C are the amplitude, position and broadening of the peak, and E_g is the Tauc band gap energy. The real part ε_1 of the dielectric function is derived from (4.86) using the Kramers-Kronig relation and has the form [65, 66]:

$$\varepsilon_1(E) = \varepsilon_\infty + \frac{2}{\pi}\mathcal{P}\int_{E_g}^{\infty}\frac{\zeta\cdot\varepsilon_2(\zeta)}{\zeta^2-E^2}\mathrm{d}\zeta. \tag{4.87}$$

Here ε_∞ is the high-frequency dielectric constant, $\mathcal{P}$ is the Cauchy principal value of the integral, for more detailed information see [65, 66]. Despite the rather complicated expression, the dielectric function can be modeled using only five parameters [ε_∞, A_L, C, $E_{L,0}$ and E_g] and evaluated fast using analytical expression.

Effective medium approximation

The effective medium approximation is an approach based on representing the heterogeneous material as a set of inclusions (or guest materials) embedded into matrix (often called host material). In such a case the effective dielectric function of a mixture can be calculated if the dielectric functions of its components are known [71]. This means that the optical functions of the heterogeneous material can be modeled as a combination of individual optical functions of all contained materials. This approach is often used for modeling of composite materials and also surface roughness.

There are several formulations of the effective medium theory which slightly differ in the choice of the host medium. However, for isotropic samples with random orientation of ellipsoid inclusions, they all can be written in the same generic form [71–73]:

$$\frac{\varepsilon_{eff}-\varepsilon_h}{\varepsilon_{eff}+\gamma_S\varepsilon_h} = \sum_j f_j\frac{\varepsilon_j-\varepsilon_h}{\varepsilon_j+\gamma_S\varepsilon_h}, \tag{4.88}$$

where ε_{eff}, ε_h and ε_j are the dielectric functions of the effective medium, of the host, and of the j-th inclusion, respectively, γ_S is a factor related to the screening and the shape of the inclusions (for example, $\gamma_S = 2$ for 3-dimensional spheres) and f_j is the volume fraction of the j-th constituent, where $\sum_j f_j = 1$.

In this thesis, we use Bruggeman effective medium approximation (B-EMA) in which a mixture of materials is represented by inclusions of particular materials embedded directly into the effective medium itself. In the above formulation (4.88) this is equivalent to choosing $\varepsilon_h = \varepsilon_{eff}$. The left-hand side of (4.88) vanishes leading to B-EMA in the form:

$$0 = \sum_j f_j \frac{\varepsilon_j - \varepsilon_{eff}}{\varepsilon_j + 2\varepsilon_{eff}}, \tag{4.89}$$

where spherical inclusions for which $\gamma_S = 2$ are assumed.

The B-EMA makes no assumption concerning the material that has the highest constituent fraction, and is therefore self-consistent. It is most useful when no constituent forms a clear majority of the material. The B-EMA is frequently used in ellipsometry to model surface roughness [60]. The surface roughness is in the model represented by an effective medium layer composed from the material and void. If the surface layer is very thick, it is sometimes necessary to incorporate several layers, each with a different fraction of voids and underlying material [71], or apply even more advanced theories, for example Rayleigh-Rice perturbation theory [74].

5 Results for pyramidal textured samples

Outline

Surface texturing of solar cells enhances light trapping and thus improves their efficiency. The most widely used textures are pyramidal ones, since they are easy to fabricate at relatively low cost, while exhibiting desired light trapping properties. Optimization of thin film systems for pushing the efficiency of silicon heterojunction solar cells requires deep knowledge of effect of the surface texture.

This chapter focuses on a detailed study of the differences between various pyramidal textures and their impact on the solar cell design, fabrication, and performance. First, the impact of different pyramidal textures on the sample reflectance is studied and the optical model of double-reflection is introduced in Section 5.1. Section 5.2 reveals unexpected differences between pyramid vertex angles of real samples and the theoretical value of $70.52°$, and offers an explanation for these variations. Consequences of pyramid vertex angle variation for thin film deposition and performance of silicon heterojunction solar cells are discussed in Section 5.3 together with an approach for monitoring of thin film thicknesses and optimization of multi-layer system on pyramidal surfaces.

5.1 Reflectance of pyramidal textured surfaces

The measurement of the sum of total reflectance and transmittance $(1 - A)$ for all six samples with different pyramidal surfaces (shown in Fig. 2.2) was performed using the spectrophotometer with the integrating sphere as described in Section 3.1. The measurements were done in the spectral range of 250 - 1300 nm (see Fig. 5.1).

The crystalline silicon energy bandgap $E_g = 1.12$ eV corresponds to wavelength $\lambda = 1107$ nm. Owing to the limited light penetration depth in $2.6\ \Omega \cdot$cm silicon, the $(1 - A)$ measurement below the wavelength of about 1000 nm corresponds well to the total (specular and diffuse) reflectance of the sample due to the absorption and sufficient wafer thickness of about 230 μm. However, for longer wavelengths, the light is partially (or completely for photon energies below the silicon bandgap) transmitted through the wafer to its backside. Therefore, the transmittance through the sample rapidly increases for wavelengths above 1100 nm and the sum of total reflectance (including front and back-side reflectance) and transmittance reaches 1 due to a zero absorptance.

Figure 5.1 shows reflectances measured for both sample series which were prepared using etching solution of type A and type B. We can compare samples without any additional post-treatment (samples A1 and B1), samples after short surface post-treatment (A2 and B2), and after long post-treatment (A3 and B3). The additional surface post-treatment increases the sample reflectance (as shown in Fig. 5.1) due to almost flat parts in the U-shaped valleys between pyramids (see right column in Fig. 2.2). This is not desirable for solar cell applications

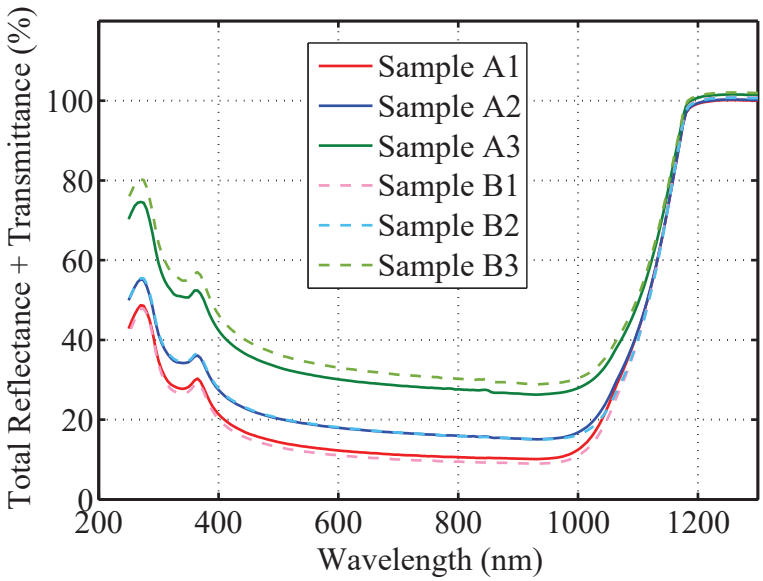

Figure 5.1 – Sum of total reflectance and transmittance corresponding to (1 - absorptance) measurement for type A and B series of samples with no additional surface post-treatment (A1, B1), after short surface post-treatment (A2, B2) and after long surface post-treatment (A3, B3).

for which minimal reflectance is required. Both samples without any additional surface post-treatment (A1 and B1) exhibit the lowest reflectance in their series (see Fig. 5.1) and are therefore suitable for solar cell applications from the optical point of view. Therefore these two samples have been studied in more details in this thesis.

Considering the case of clearly identifiable walls of pyramidal textures (sample A1 and B1), we propose a simplified model considering the double-reflection on flat pyramidal facets along the dominant light path marked in Fig. 5.2(a) to model the total reflectance. The model is based on a detailed study of multiple beam reflection, transmission, and propagation in silicon pyramids showing that the most straightforward beam interaction with pyramids is dominant. Using the Fresnel formulas for reflection from a silicon surface (4.64), (4.65) we model the total reflectance R from our samples as

$$R = \frac{1}{2}(R_s + R_p) = \frac{1}{2}(R_{s1}R_{s2} + R_{p1}R_{p2}) = \frac{1}{2}(|r_{s1}r_{s2}|^2 + |r_{p1}r_{p2}|^2), \qquad (5.1)$$

where subscripts s and p represent particular polarizations and subscripts 1 and 2 indicate first and second reflection from pyramidal facet. First, the reflectance from the first and second facet are multiplied separately for each po-

larization ($R_{s1}R_{s2}$). Then, the obtained reflectances for each polarization after double-reflection on pyramid facets are merged. Fresnel coefficients are according to (4.62):

$$r_{s,i} = \frac{n_1 \cos\varphi_i - n_2 \cos\varphi_{it}}{n_1 \cos\varphi_i + n_2 \cos\varphi_{it}}, \tag{5.2a}$$

$$r_{p,i} = \frac{n_1 \cos\varphi_{it} - n_2 \cos\varphi_i}{n_1 \cos\varphi_{it} + n_2 \cos\varphi_i}, \tag{5.2b}$$

where $i = 1$ for reflection from the first pyramid facet and $i = 2$ for reflection from the second pyramid facet. Refractive indices n_1 and n_2 of air and c-Si, respectively, are used for both reflections from facets, φ_i is the angle of incidence on the i-th facet:

$$\varphi_1 = \frac{180° - \alpha}{2}, \tag{5.3a}$$

$$\varphi_2 = \alpha - \varphi_1, \tag{5.3b}$$

where α is the vertex angle of the pyramid, and φ_{it} is the refractive angle for the i-th facet calculated using the Snell's law of refraction.

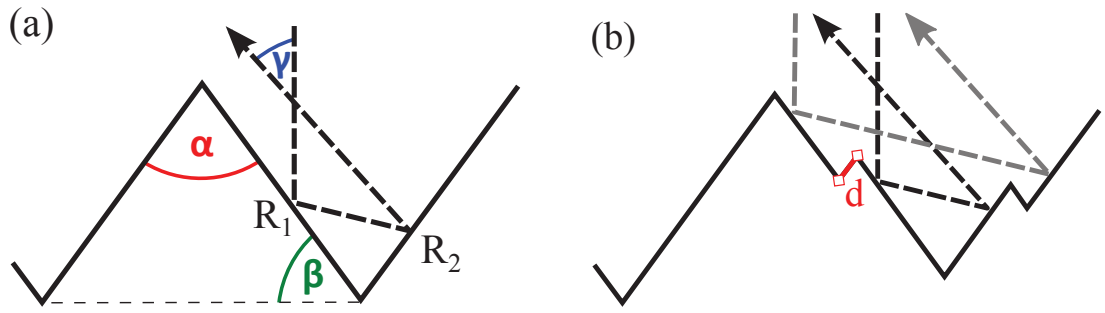

Figure 5.2 – Schematic drawing of the dominant path of light undergoing double-reflection from the pyramidal facets. Light impacts wafer at a normal incidence with respect to its plane. (a) A model considering the double-reflection on flat pyramidal facets. The vertex angle α, the side angle β and the emerging angle γ together with the first and second reflections R_1 and R_2 on the pyramidal facets are marked. (b) Model considering terraces on the pyramidal facets. The terrace corresponding to the height step d between two parallel facets is marked.

Figure 5.2(a) shows the dominant light path undergoing a double-reflection from the neighboring facets. The vertex angle α, the side angle β, and the emerging angle γ at which the light is reflected from the pyramidal surface with respect to the normal incidence to the plane of the wafer are marked. Angles are related

as follows:

$$\alpha = 180° - 2\beta, \tag{5.4a}$$

$$\beta = \frac{180° - \alpha}{2} = \varphi_1, \tag{5.4b}$$

$$\gamma = 180° - 2\alpha, \tag{5.4c}$$

where φ_1 is the angle of incidence at the first facet. Figure 5.2(b) shows the model considering terraces on the pyramidal facets as described in the following text.

Figure 5.3 shows the measured total reflectance of samples A1 and B1 (blue dashed and green dashed-dotted lines, respectively) and results of our simplified double-reflection model (red line) described above, applied on pyramids with a vertex angle $\alpha = 75°$ (this value is explained in Section 5.2.1). We can observe a good agreement between measured values and the model, especially for wavelengths above 400 nm.

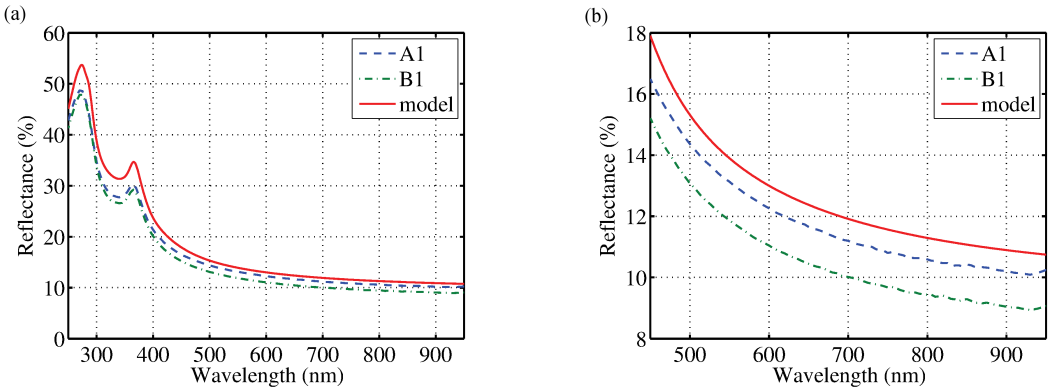

Figure 5.3 – Measured total reflectance of samples A1 and B1 (blue dashed and green dashed-dotted lines, respectively) and modelled reflectance of pyramidal surface with vertex angle $\alpha = 75°$ (red solid line) in the spectral range (a) 250-950 nm and (b) the detail of the spectral range 400-950 nm.

We have studied also the impact of the variation of the pyramidal vertex angle on the resulting reflectance. Figure 5.4 shows a minimal difference between modeled reflectance for pyramidal surface with vertex angle $\alpha = 70°$ and $\alpha = 75°$ (see black solid and magenta dotted lines in Fig. 5.4). A 2 nm thick layer of SiO_2 [75] was added to the model of pyramid with vertex angle $\alpha = 75°$ to evaluate the effect of the surface oxide. However, this change didn't affect the result significantly (see green dashed line in Fig. 5.4). Finally, terraces on the pyramidal facets [as observed in Fig. 2.2(A1) and drawn schematically in Fig. 5.2(b)] were taken into account. These terraces cause phase shift in the reflected light beams. To represent this effect, the Fresnel reflection coefficient of two parallel pyramidal

facets connected by the terrace of size d was calculated as:

$$r_1' = \frac{1}{2}(r_1 + \xi\, r_1), \tag{5.5a}$$

$$\xi = e^{i\theta}, \tag{5.5b}$$

$$\theta = \frac{2\pi x}{\lambda}, \tag{5.5c}$$

$$x = 2d\, \cos\frac{\alpha}{2}. \tag{5.5d}$$

Here θ represents the phase shift and x is the path difference between the light beams reflected from these facets [see Fig. 5.2(b)]. This superposition of coherent light beams reflected from parallel facets (assuming for simplicity equal contribution from each one) has much more significant influence on the resulting sample reflectance than the previously considered effects as shown in Fig. 5.4 for vertex angle $\alpha = 75°$ and terrace size $d = 90$ nm. Since we don't know the precise statistical distribution of the terraces on the pyramid facets, it is not easy to model their effect accurately. Nevertheless, incorporation of this effect into the model gives us better agreement with the experimental data.

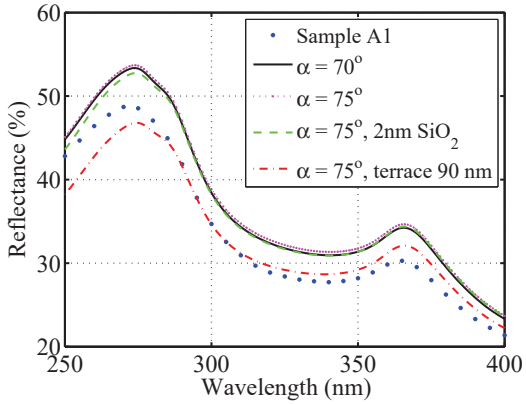

Figure 5.4 – Comparison of measured reflectance of sample A1 (blue symbols) and modeled reflectance (lines) in the spectral range 250-400 nm. Models of pyramidal surface with vertex angle $\alpha = 70°$, $\alpha = 75°$, $\alpha = 75°$ covered by 2 nm of SiO_2, and $\alpha = 75°$ with terraces of size $d = 90$ nm are represented by black solid line, magenta dotted line, green dashed line, and red dashed-dotted line, respectively.

We have demonstrated, that the model based on double-reflection along the dominant light path is suitable to describe light reflected from pyramidal surface. Therefor, we will adopt this strategy also for analysis of ellipsometric measurements in Section 5.3.2.

5.2 Analysis of angles of pyramids

5.2.1 Measurement of the angles of pyramids

Figure 5.5 shows a schematic shape of one pyramid on the wafer surface. Since all pyramids should be formed by intersections of $\{111\}$ crystallographic planes, the geometry of each pyramid and its angles are defined with high accuracy. The angle α between two opposite facets (vertex angle of the pyramid) and the angle β between a facet and a base of the pyramid (side angle) are determined from the S4S2E triangle (marked in Fig. 5.5) as $70.52°$ and $54.74°$, respectively.

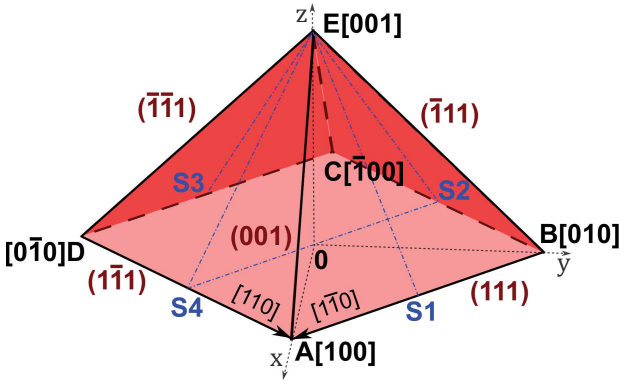

Figure 5.5 – Geometric drawing of the c-Si pyramid formed by four facets $\{111\}$ and a base (001). ABCD plane corresponds to the flat surface of the (100) wafer. Crystallographic directions $[110]$ and $[1\bar{1}0]$ are marked by arrows.

However, cross-sectional images from the scanning electron microscope in Fig. 5.6 show that different texturing recipes (for samples type A and type B) lead to pyramids with different vertex angles α. The cross-sectional images were obtained by tilting the sample to acquire the view of the projection of the pyramidal facet to the S4S2E cross-section marked in Fig. 5.5. In Fig. 5.6, we observe $\alpha \approx 75°$ for A1 sample and $\alpha \approx 80°$ for B1 sample.

To confirm our observations statistically on a larger surface area of samples, reflectance measurements at oblique angle of incidence and angle-resolved Mueller matrix polarimetry were used.

In the first case, we put our sample inside the integrating sphere of the spectrophotometer and rotated it to gradually change the angle of incidence [for illustration see Fig. 5.7]. The sum of total reflectance and transmittance of the samples at the angles of incidence of $8°, 15°, 20°, 30°, 47.5°, 50°, 52.5°, 55°$, and $60°$ with respect to the normal of the wafer was measured. The spot size of several mm^2 allowed us to get averaged information from a large surface and not only from a few pyramids.

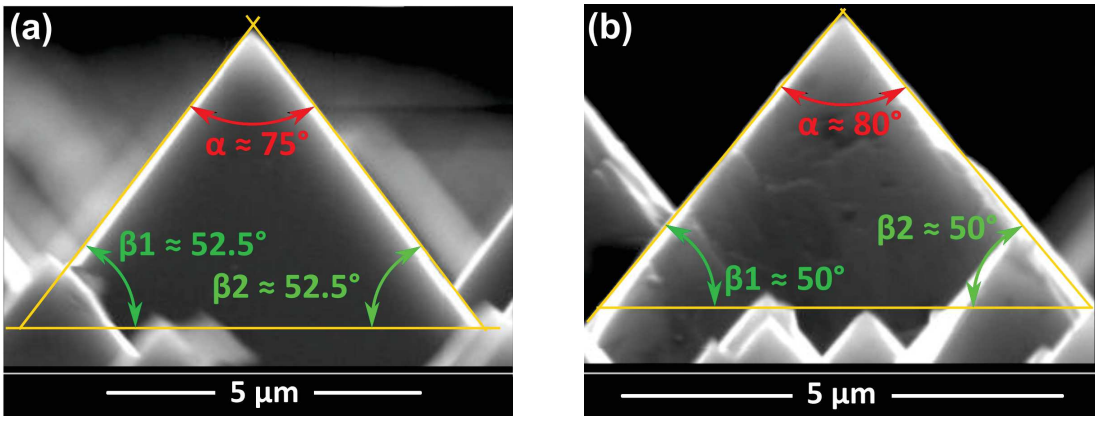

Figure 5.6 – SEM cross-sectional images of pyramidal surfaces of wafers textured by different etching conditions (a) A1 sample and (b) B1 sample with measured angles of interest.

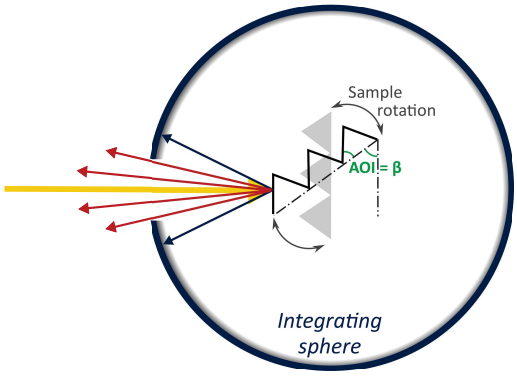

Figure 5.7 – Schematic drawing of the reflectance measurement inside the integrating sphere. Sample is rotated to change the angle of incidence. When the angle of incidence corresponds to the side angle β of the pyramid, part of the reflected light (red arrows) escapes from the integrating sphere through the entrance hole.

When the pyramidal facets are perpendicular to the incident beam, the light is reflected back and some part escapes from the integrating sphere through the entrance hole as illustrated by the red arrows in Fig. 5.7. This causes a decrease of the measured intensity and corresponds to the local minima in Fig. 5.8(a) and Fig. 5.8(b). The angle of incidence is equal to the side angle β of the pyramid and $\alpha = 180° - 2\beta$ according to (5.4a). Note the excellent agreement of these side angles with the values obtained from cross-sectional SEM confirming the vertex angle $\alpha = 75°$ for the pyramid of sample A1 and $\beta = 80°$ for sample B1.

We have measured A1 and B1 samples by angle-resolved Mueller matrix po-

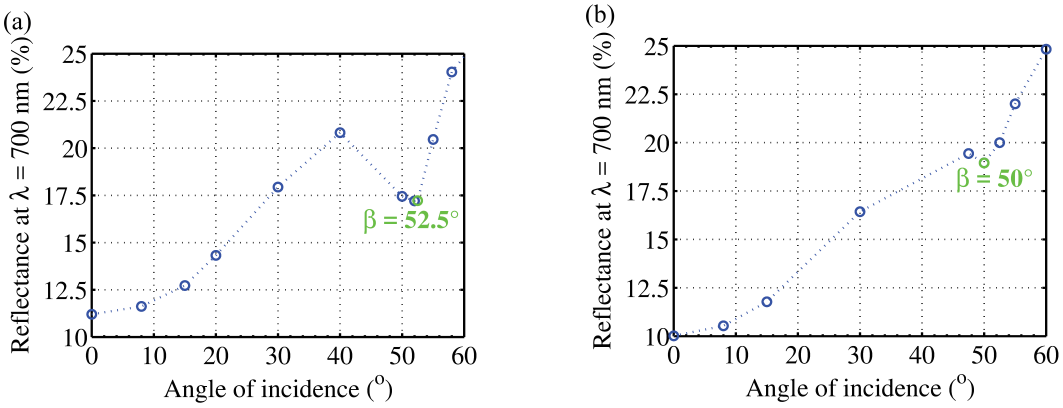

Figure 5.8 – Total reflectance of the pyramidal textured wafers at the wavelength $\lambda = 700$ nm measured as a function of the angle of incidence for samples (a) A1 and (b) B1.

larimetry to compare scattered light patterns for different etching conditions. This method gives us access to the angular distribution of the light reflected from pyramidal surface after the normal incidence on the wafer plane as shown in the Fig. 5.9. The advantage of this method is that we have images of both real (see subplots in Fig. 5.9) and Fourier space from the same area of the sample. The diameter of the imaged spot is around 30 μm.

According to Baker-Finch and McIntosh study of the reflection of normally incident light from pyramidal textured silicon solar cells [31], using the 3-dimensional ray tracing calculus described by Yun et al. [30], more than 68 % of light undergoes double-reflections from the pyramidal facets along to the path marked in Fig. 5.2(a). The angle γ at which the light emerges after these two reflections corresponds to the polar angle ϕ from the angle-resolved Mueller matrix polarimetry measurement. Measured emerging angle γ enabled us calculation of corresponding vertex angle α of the pyramid using the equation (5.4c) as $\alpha = \frac{1}{2}(180° - \gamma)$.

Figure 5.9(a) shows four dominant maxima representing the four-fold symmetry of the pyramids. Each maximum appears around the polar angle $\phi = 30°$ which corresponds to the emerging angle $\gamma = 30°$ and confirms the vertex angle $\alpha = 75°$ for A1 sample as determined previously by the cross-sectional SEM.

In contrast, Fig. 5.9(b) shows a diffusive ring indicating broken symmetry due to non-idealities on the pyramidal facets and stronger diffraction due to smaller pyramid sizes (see Fig. 2.2) of sample B1. Despite this, the center of the diffusive ring is situated at the polar angle $\phi = 20°$ equal to the emerging angle $\gamma = 20°$ corresponding to the vertex angle $\alpha = 80°$ which agrees with the value determined for this sample by SEM.

Values of the vertex angle α obtained from SEM measurements, the side angle

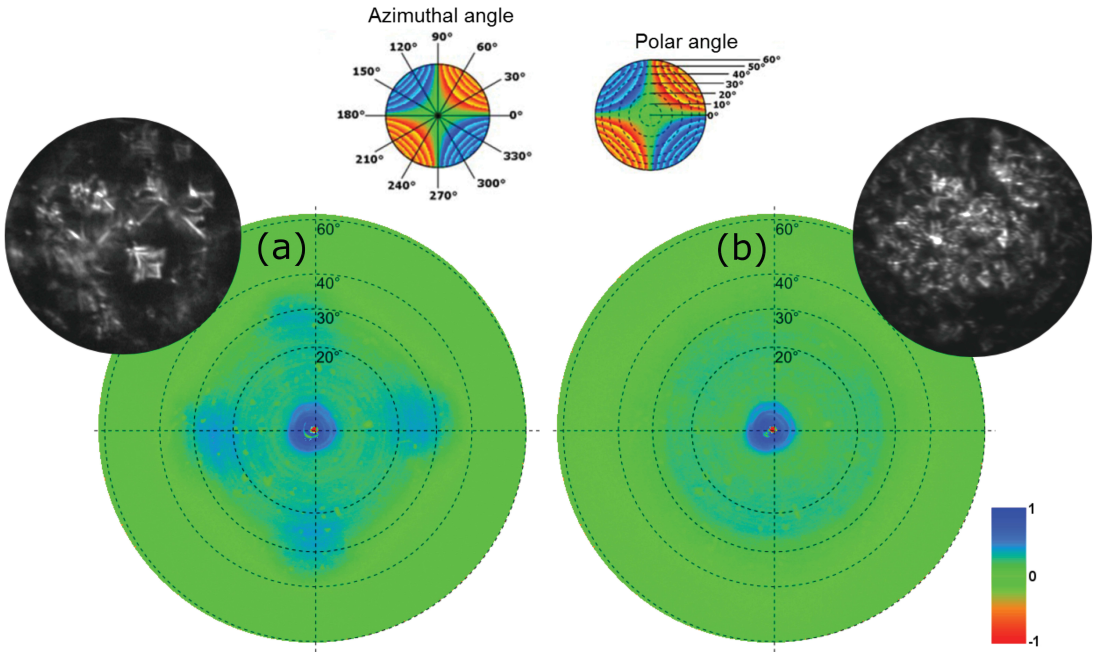

Figure 5.9 – Angle-resolved Mueller matrix polarimetric data of the samples (a) A1 and (b) B1. Each point represents element M_{22} of normalized Mueller matrix for corresponding polar and azimuthal angle ϑ and ϕ, respectively. Azimuthal and polar angles ϑ and ϕ are defined according to the schematics on the top of the figure. Black and white subplots show the real space images.

β established using the reflectance measurement with the integrating sphere, and the corresponding emerging angle γ confirmed by angle-resolved Mueller matrix polarimetry for the ideal case and the samples A1 and B1 are listed in Table 5.1.

	SEM α (°)	Integrating sphere β (°)	AR-MMP γ (°)
Ideal case	70.52	54.74	38.96
Sample A1	75	52.5	30
Sample B1	80	50	20

Table 5.1 – Values of the vertex angle α, the side angle β, and the corresponding emerging angle γ for the ideal case and the samples A1 and B1 obtained from the SEM measurements, reflectance measurements with the integrating sphere, and from angle-resolved Mueller matrix polarimetry, respectively.

From the three independent measurements above, we conclude that the geometry of the studied pyramids is different from the ideal model. Moreover, the resulting geometry depends on the used etching solution.

5.2.2 Origin of different pyramidal angles

In this subsection we propose an explanation for the difference between the experimental and ideal pyramid vertex angles.

The SEM image of sample A1 [see Fig. 5.10(a)] shows smooth facets. Apart from the occasional terraces, there are no regular steps which could explain the difference in the pyramid vertex angle. However, the scanning transmission electron microscopy high-angle annular dark-field (STEM-HAADF) image in Fig. 5.10(b) clearly shows atomic steps which occur relatively regularly. This causes the effective change in the facet angle by about the deviation angle $\delta \approx 3^\circ$ marked in the Fig. 5.10(b). This corresponds to apparent angle in SEM. Thus we can conclude that atomic steps on the walls are responsible for modifying the apparent pyramid vertex angle. This has important consequences for the surface passivation and film deposition as will be discussed below.

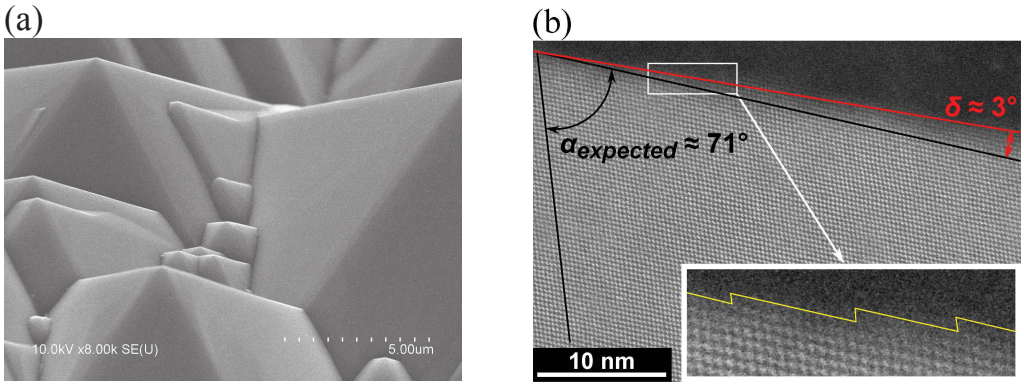

Figure 5.10 – (a) Image of pyramidal surfaces of the sample A1 taken by SEM. (b) Image of the pyramidal edge of the sample A1 taken by STEM-HAADF. $\{111\}$ crystallographic planes forming the angle 71° which is near the ideal vertex angle $\alpha = 70.52^\circ$ are marked in black, while deviation angle $\delta \approx 3^\circ$ induced by atomic steps is marked in red. The inset shows a zoom detail of the atomic steps highlighted by yellow.

5.3 Analysis of thin films deposited on pyramids for silicon heterojunction devices

5.3.1 Consequences of variation of pyramidal vertex angles for silicon heterojunction solar cell performance

The deposition time for a required thin film thickness is usually calculated from the deposition rate of material on a reference flat substrate and the geometrical factor of the pyramid. The geometrical factor $P = 1/\sin(\frac{\alpha}{2})$ can be obtained as a ratio between the surface area of the pyramid and its corresponding horizontal projection. Since P varies for pyramids with different vertex angles, using the same deposition time for different samples leads to different thin film thicknesses. Values of the geometrical factor P for the ideal pyramid and samples A1 and B1 are listed in Table 5.2 together with the thicknesses L of thin films deposited with the same deposition time as for a 40 nm thin film deposited on the flat reference substrate. According to the table, the deposition time has to be adjusted using the proper geometrical factor for the particular samples to obtain thin films of required thicknesses. The precise control of the thin film thickness is essential to fabricate solar cells with design optimized for the maximum energy conversion efficiency.

	α (°)	P (-)	L (nm)
Flat substrate	-	1	40
Ideal pyramid	70.52	1.732	23.095
Sample A1	75	1.643	24.346
Sample B1	80	1.556	25.707

Table 5.2 – Values of the vertex angle α, the geometrical factor P, and the thickness L of the thin films corresponding to the reference 40 nm thin film deposited on the flat substrate for the ideal pyramidal surface and the samples A1 and B1

Different vertex angles α lead to different surface areas of the pyramids. This affects the thicknesses of material layers deposited by PECVD on top of the pyramids to create the SHJ solar cell. Moreover, atomic steps observed in TEM images may have a negative impact on the surface passivation.

Apparent vertex angles different from the ideal value of $70.52°$ are due to the presence of atomic steps as shown before. Examples of atomic steps on the c-Si surface are shown in a scanning transmission electron microscopy bright-field (STEM-BF) image in Fig. 5.11. These surface irregularities can induce local epitaxy and extra effort is sometimes needed to impede this phenomenon, as described in the recently patented approach [44]. Indeed, epitaxial growth, even

very localized, has to be avoided during the deposition of a-Si:H, as it can reduce the passivation quality and thus decrease the minority carrier lifetime in silicon solar cells [43,44,76,77].

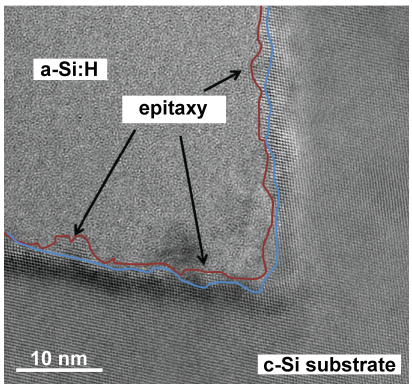

Figure 5.11 – Image of a valley of pyramidal textured sample of type A1 passivated with a 27 nm thick a-Si:H layer taken by STEM-BF [43]

5.3.2 Model of spectroscopic ellipsometry data

Since different pyramid vertex angles α lead to various deposition rates as discussed in Section 5.3.1, the precise thickness control of deposited films to obtain the designed solar cell architecture is necessary. Spectroscopic ellipsometry with inclined sample in lateral measurement geometry described in Section 3.2.1 was used to measure the a-Si:H thin passivation films on c-Si pyramids of sample A1. Advanced methods based on diffraction theory could be used for modeling [78]. However, application of these methods to the samples with pyramids of edges as large as 5-10 μm would be time-consuming and demanding for computational performance. Moreover, we have demonstrated that the double-reflection model describes measured reflectance data very well (see Section 5.1). We performed a ray-analysis of the light interaction with the inclined pyramid which revealed that only light undergoing a specular reflection from horizontal facet can reach the detector (see Fig. 5.12). Based on this and the verified model for the double-reflection introduced in the Section 5.1, we consider the following approximation to be sufficient for modeling of the ellipsometric data.

The inclined sample is treated as a flat c-Si wafer covered by an a-Si:H layer of thickness L_1 and a native silicon dioxide layer (SiO_2) of thickness L_2 (see Fig. 5.13). The silicon dioxide layer was included into the model to represent a possible surface oxidation. Furthermore, it compensates the effect of a surface roughness on optical properties, since its refractive index is very close to that of a surface roughness layer modeled by Bruggneman effective medium

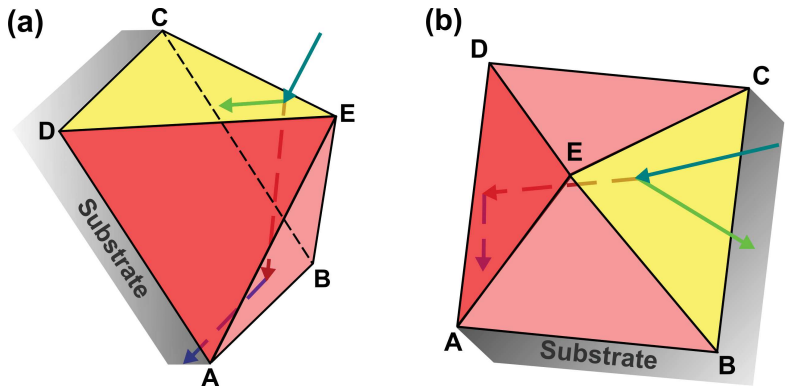

Figure 5.12 – Illustration of light beam interaction with the tilted pyramid. Light incident on the horizontal facet (a) undergoes either a specular reflection to the detector (green arrow) or goes into the wafer (purple arrow). Light incident on the side facet of the tilted pyramid (b) is either reflected outside the detector (green arrow) or goes to the wafer (purple arrow).

approximation [60]. Dielectric functions of crystalline and hydrogenated amorphous silicon were obtained from Ref. [79] and earlier characterization of a hydrogenated amorphous silicon thin film prepared at LPICM and modelled using Tauc-Lorentz model [65, 66]. The dielectric function of silicon dioxide was obtained from Ref. [75]. For more detailed information on dielectric functions of used materials see Appendix A.

The model is fitted to the experimental data using the Levenberg-Marquard least-square minimization algorithm implemented in the DeltaPsi2 software (Horiba Scientific). The following fitting error function χ^2 (4.82) was used as a criterion for the least square algorithm [80]:

$$\chi^2 = \frac{1}{(2M-N-1)} \cdot \left[\sum_{k=1}^{M} \frac{\left(I_{S,k}^{meas} - I_{S,k}^{mod}\right)^2}{\left(\sigma_{I_{S,k}}\right)^2} + \sum_{k=1}^{M} \frac{\left(I_{C,k}^{meas} - I_{C,k}^{mod}\right)^2}{\left(\sigma_{I_{C,k}}\right)^2} \right], \tag{5.6}$$

where values I_S and I_C are connected with the ellipsometric angles through relations (4.71). Superscripts $meas$ and mod stand for the measured and modeled values, respectively. $\sigma_{i,k}$ represents the estimated measurement error, which is set by the software at a constant value of 0.01. The sum is calculated over the measured spectral interval. M stands for the number of spectral points and N is the number of fitting parameters. Fitting parameters are the thickness of the a-Si:H layer (L_1), the thickness of the SiO_2 layer (L_2) and the angle of incidence.

Various angles of incidence were used to measure ellipsometric data to evaluate the impact of the AOI on the measurement and to identify the optimal measurement set-up. A pyramidal textured c-Si wafer of type A1 covered by a passivation layer of a-Si:H was used as a test sample. During first 30 s of 10 min a-Si:H

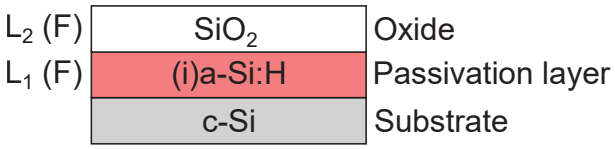

Figure 5.13 – Schematic drawing of a multi-layer optical model consisting of a c-Si substrate covered by an a-Si:H layer of the thickness L_1 and a SiO_2 layer of the thickness L_2.

deposition CH_4 gas was introduced into the reactor to deposit a thin layer (thickness of about 1.5 nm) of a-SiC:H to prevent the epitaxial growth as described in [43, 44]. Deposition conditions for both materials are listed in table 2.1. Dielectric function of a-SiC:H is in Appendix A.

Figure 5.14(a) shows the sample attached to the tilted stage of ellipsometer while Fig. 5.14(b) shows a cross-sectional TEM image of the sample covered by a protective Pt layer and SiO_x oxide for the purpose of TEM measurement. Values of the thickness of a-Si:H layer slightly change from 27.3 nm to 26.4 nm for different parts of the sample as marked in the figure.

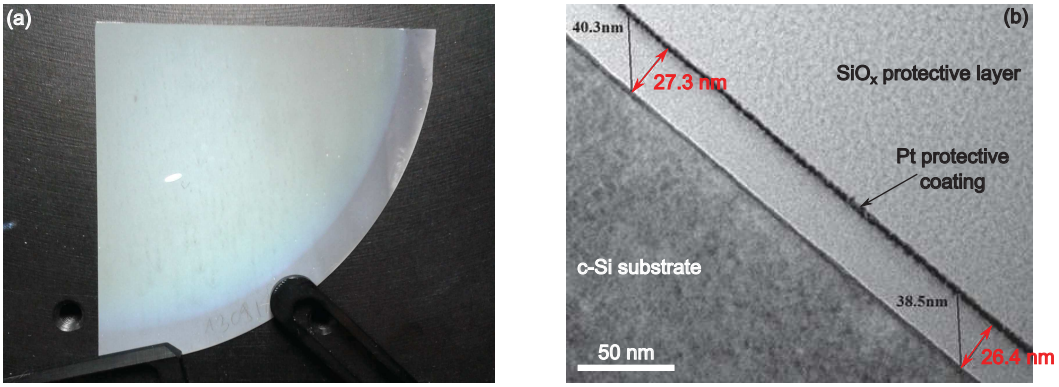

Figure 5.14 – (a) Photo of the sample consisting of 1.5 nm of a-SiC:H and a-Si:H layer of thickness L_1 on c-Si pyramidal wafer of type A1. (b) Cross-sectional TEM image of the same sample. Sample is covered by a protective Pt layer and SiO_x oxide for purposes of TEM measurement [43].

We performed the ellipsometric measurement of this sample acording to the method described in Section 3.2.1 using AOI of 45°, 50°, 52.5°, 55°, 57.5°, 60°, 65°, and 70°, respectively. A 1.5 nm layer of a-SiC:H corresponding to the 30 s of deposition was added between c-Si and a-Si:H layers of the optical model described above and shown in Fig. 5.13 to fit the experimental data. Results for each AOI are listed in Tab. 5.3.

Verification of the optical model was carried out by the comparison of a-Si:H

Fit results

Set AOI (°)	Fit AOI (°)	L_1 (nm)	L_2 (nm)	χ^2 (-)
70	70.3	25.9	0.01	12.23
65	64.6	26.5	1.3	6.67
60	59.9	28.8	1.3	2.10
57.5	57.6	29.2	1.4	1.32
55	55.2	30.0	1.5	0.89
52.5	53.0	30.1	1.4	0.49
50	49.5	29.0	2.7	0.26
45	45.3	29.6	2.2	0.14

Table 5.3 – Best fitted parameters for various angles of incidence obtained from an optical modeling of ellipsometric data.

layer thickness determined by the spectroscopic ellipsometry and transmission electron microscopy. Figure 5.15 shows that values of thickness of a-Si:H layer obtained by spectroscopic ellipsometry at variousAOIchange between 25.9 nm and 30.1 nm (see blue symbols in Fig. 5.15). These results agree well with values obtained from TEM measurement (see black lines in Fig. 5.15) thus supporting the validity of the optical model.

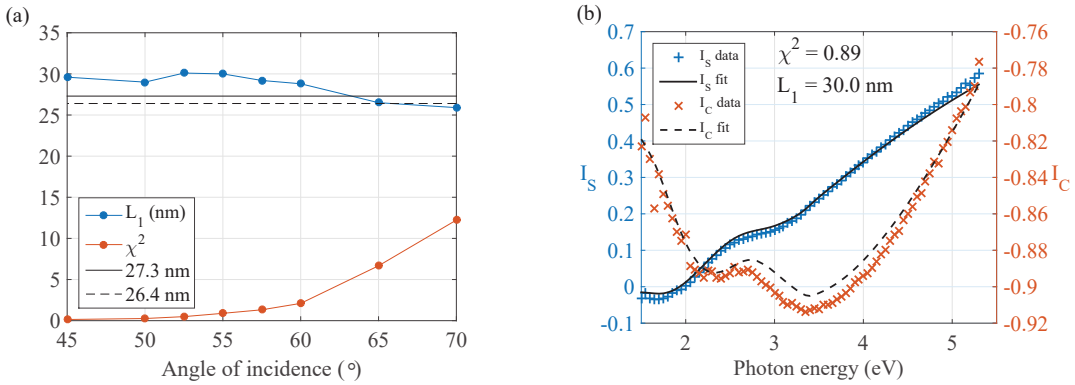

Figure 5.15 – (a) Thickness of a-Si:H passivation layer L_1 (blue symbols) on c-Si pyramidal wafer of type A1 determined with the fitting error function χ^2 (orange symbols) from spectroscopic ellipsometry at various angles of incidence and the lower and higher value of L_1 (solid and dashed black lines, respectively) deduced from the TEM cross-sectional measurement of the sample (as marked in Fig. 5.14). (b) Ellipsometric values I_S (blue) and I_C (orange) obtained from model (lines) and measurement (symbols) of the same sample at AOI of 55°.

Note, that values of fitting error function χ^2 increases significantly with AOI

from 0.15 at $45°$ to 14.42 for $70°$ [see orange symbols in Fig. 5.15(a)] indicating worse agreement between model and experimental data for higher AOI. In contrast, sensitivity of ellipsometric measurement is for semiconductor materials better at AOI around $70 - 80°$ [60, p.40], where is the largest contrast in reflectance between s- and p-polarized light, and this sensitivity drops down with decreasing AOI. Therefore, we decided to use $AOI = 55°$ for further measurements to have as high angle as possible with reasonably low χ^2 ensuring good relation between the ellipsometric sensitivity and accuracy of the optical model. Figure 5.15(b) shows a good agreement between ellipsometric values I_S and I_C obtained from model and measurement for $AOI = 55°$.

Five samples of c-Si pyramidal textured wafers (type A1) with various thicknesses of a-Si:H passivation layer (without a-SiC:H buffer layer) were measured by SE at $AOI = 55°$ with respect to the tilted pyramid plane since there is a good sensitivity to the ellipsometric angles and film thicknesses at this angle of incidence. The deposition times of a-Si:H layers of samples A1-3, A1-5, A1-7.5, A1-10, and A1-11, leading to different thicknesses, were 3, 5, 7.5, 10, and 11 minutes, respectively. The optical model described above (see Fig. 5.13) was applied to the measured data. Obtained results are shown in Table 5.4 and Fig. 5.16.

		Fit results		
		$AOI = 55°$		
Sample	Deposition time (min)	L_1 (nm)	L_2 (nm)	χ^2
A1-3	3	**7.5**	1.4	0.35
A1-5	5	**14.2**	1.4	0.19
A1-7.5	7.5	**21.3**	1.1	0.39
A1-10	10	**29.0**	0.6	0.41
A1-11	11	**32.3**	1.9	0.19

Table 5.4 – Best fitted parameters obtained from an optical model of the samples A1-3, A1-5, A1-7.5, A1-10, and A1-11.

A cross-sectional TEM measurement of sample A1-11 was performed to compare a-Si:H layer thickness with that obtained from ellipsometric measurement. A cross-sectional TEM image of the A1-11 sample covered by a protective Pt layer and SiO_x oxide for the purpose of TEM measurement is shown in Fig. 5.17(a). Values of the a-Si:H thickness slightly change from 33.2 nm to 34.1 nm for different parts of the sample as marked in the figure. Thickness of the a-Si:H layer of the same sample determined from the spectroscopic ellipsometry is $L_1 = 32.3$ nm with value of fitting error function $\chi^2 = 0.19$ (see Tab. 5.4). There is a good agreement between the thickness of a-Si:H layer determined by spectroscopic ellipsometry and TEM measurement. Figure 5.17(b) shows a good agreement be-

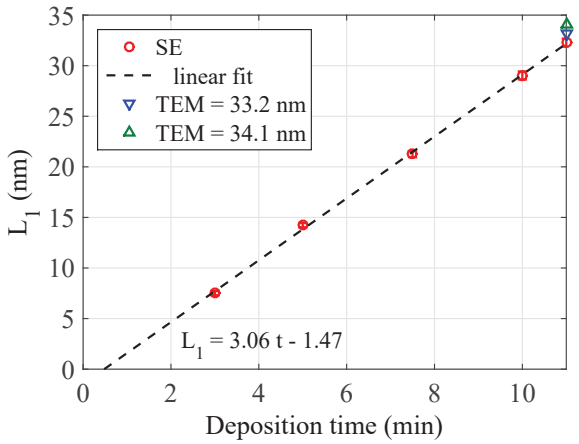

Figure 5.16 – Thickness of a-Si:H passivation layer L_1 on c-Si pyramidal wafer of type A1 determined from spectroscopic ellipsometry at the angle of incidence of 55° (red symbols) for five deposition times and the lower and higher value deduced from the TEM measurement of the sample A1-11 (blue and green symbol, respectively).

tween ellipsometric values I_S and I_C obtained from optical model and ellipsometric measurement of the sample A1-11 at AOI of $55°$.

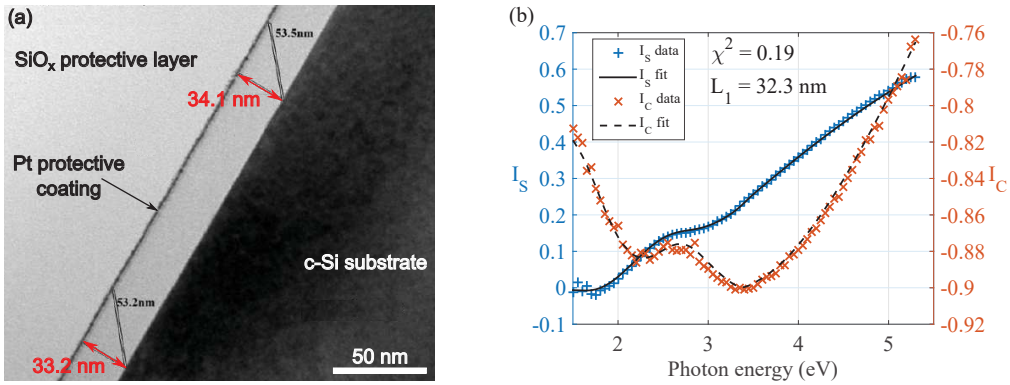

Figure 5.17 – (a) Cross-sectional TEM image of sample A1-11 consisting of a-Si:H layer L_1 on c-Si pyramidal wafer of type A1. Sample is covered by a protective Pt layer and SiO_x oxide for purposes of TEM measurement [43]. (b) Ellipsometric angles Ψ (blue) and Δ (orange) obtained from model (lines) and measurement (symbols) of the same sample at AOI of $55°$.

Figure 5.16 shows a linear dependence of the thickness of the deposited a-Si:H thin film on the deposition time. The deposition rate on pyramids can be determined from this data as (0.051 ± 0.009) nm/s.

5.3.3 Optimization of multi-layer system

We can further extend our model of pyramidal wafer surface reflectance (described in Section 5.1) to a system of multi-layers on pyramids. This is suitable for optimization of thicknesses of particular layers to maximize the optical performance and hence the resulting efficiency of fabricated solar cells.

The optimization is focused on the loss reduction in photo-generated current density ($J_{ph\,loss}$) caused by the reflection of incident light from the front surface and parasitic absorptions in particular layers of the solar cell. The front surface of the studied cell consists of the pyramidal textured (n)c-Si wafer covered by the thin intrinsic passivation layers of (i)a-SiC:H and (i)a-Si:H, the gradient p-type layer consisting of (p)a-Si:H and (p++)a-Si:H, and a transparent conducting indium tin oxide layer, as shown in Fig. 2.1(a). Figure 5.18 shows an enlarged view of the modeled structure on the front surface. Optical functions of ITO, intrinsic and doped hydrogenated amorphous silicon were determined from reference spectroscopic ellipsometry measurements of materials deposited by magnetron sputtering and PECVD on Corning glass substrates. All amorphous silicon based materials are modeled using Tauc-Lorentz model [81,82], while ITO was modeled by combination of Tauc-Lorentz [81,82] and Drude [83] model. For more detailed information on dielectric functions of used materials see Appendix A.

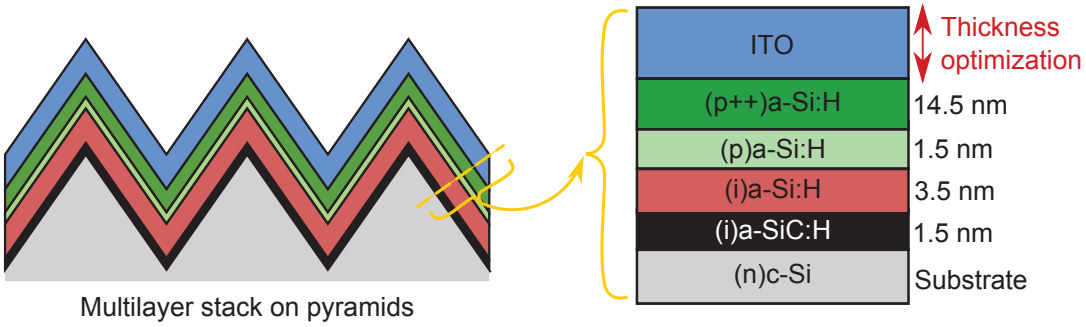

Figure 5.18 – Illustration of the modeled front surface of the studied solar cell. System of thin films on the surface of the pyramidal textured c-Si wafer (left) and its multi-layered representation consisting of the c-Si substrate covered by the (i)a-SiC:H, (i)a-Si:H, (p)a-Si:H, and (p++)a-Si:H thin films of the thickness of 1.5 nm, 3.5 nm, 1.5 nm, and 14.5 nm, respectively, and the ITO transparent conducting oxide with thickness to be optimized (right). Thicknesses of layers are taken perpendicular to the pyramidal facet.

The total reflectance of the multi-layer stack on pyramidal surface together with parasitic absorptions in thin films above active (n)c-Si absorber were modeled for various thicknesses of ITO layer using double reflection multilayer model. Figure 5.19 shows results for a multi-layer stack with 80 nm thick ITO layer

on pyramids with vertex angle $\alpha = 70°$. The grey part of this figure represents the light which penetrates into the (n)c-Si absorber and can generate charge carriers. The losses caused by parasitic absorptions in thin films above the (n)c-Si wafer and by the reflectance of the solar cell front surface are larger in the short-wavelength region. The highest losses are in the ITO and (p++)a-Si:H layers. While the thickness of the (p++)a-Si:H layer cannot be decreased (to preserve a good field effect), the thickness of the ITO layer can be further optimized.

The standard solar spectrum is included in the optimization to obtain overall solar cell performance. The loss in photo-generated current density $J_{ph\,loss}$ was calculated for each ITO thickness according to the equation:

$$J_{ph\,loss} = q \int AM1.5G\,(\lambda) \cdot [R\,(\lambda) + A\,(\lambda)]\,\mathrm{d}\lambda, \tag{5.7}$$

where $AM1.5G\,(\lambda)$ is the global standard solar spectrum at the Earth's surface [84], $R\,(\lambda)$ is the total reflectance of the structure calculated using Eq. (5.1), $A\,(\lambda)$ is the total parasitic absorptance calculated as the sum of parasitic absorptions in all layers above the active (n)c-Si substrate from the difference of the z-components of Poynting vector (4.57) at the interfaces of each layer, and q is the charge of the electron.

Figure 5.20 shows the dependence of the calculated $J_{ph\,loss}$ on the ITO deposition time. Results for each pyramidal geometry (vertex angles $\alpha = 70°$, $75°$, and $80°$, respectively) are compared with the same thin film system on the flat wafer. The minimum of the $J_{ph\,loss}$ (marked by the crosses in Fig. 5.20) determines the deposition time of the ITO layer with optimal thickness for the maximum performance of the device. Precise values of $J_{ph\,loss}$ minimum for each geometry are listed in Table 5.5. The enhanced light-trapping provided by the pyramidal surface reduces the $J_{ph\,loss}$ significantly. Moreover, there is a considerable difference between the optimal ITO deposition time for pyramidal and flat surface. The structure of thin films with thicknesses optimized for flat devices cannot be directly reused for pyramidal structures. Therefore, the optimization of the thin film structure and deposition times directly for the pyramidal texture is required.

Different pyramidal textures lead to almost the same value of the $J_{ph\,loss}$ minimum. However, the position of $J_{ph\,loss}$ minimum determining the optimal ITO effective deposition time is different for all three samples (see Table 5.5). Moreover, the minimum of the $J_{ph\,loss}$ is rather flat and small changes in the ITO deposition rate do not change the value of the $J_{ph\,loss}$ dramatically. This is advantageous for solar cell fabrication since this provides certain tolerance to the precision of the ITO film thickness.

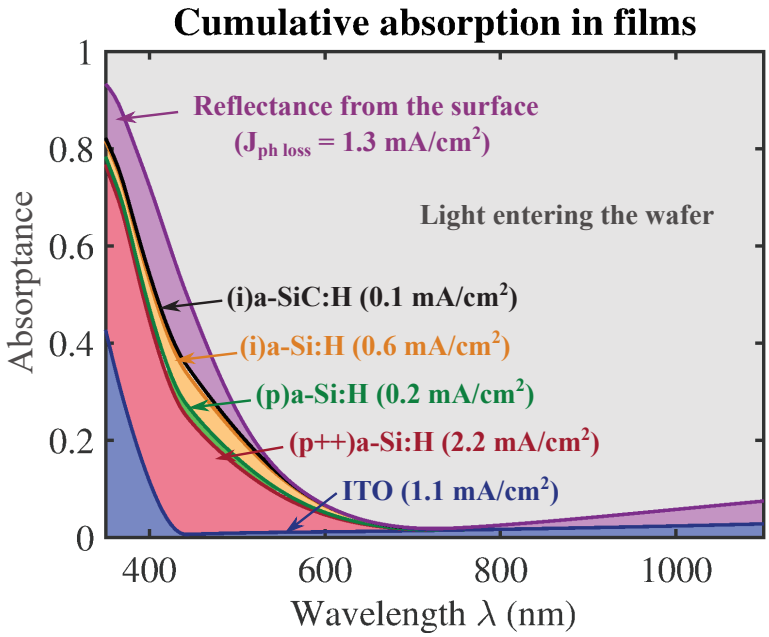

Figure 5.19 – Results for the thin film system from Fig. 5.18 on the pyramidal textured front surface of the c-Si wafer. Absorptance in each layer of the structure and reflectance from the surface as functions of the wavelength for pyramids with vertex angle $\alpha = 70°$ and ITO thickness of 80 nm. Values of $J_{ph\,loss}$ for each layer are indicated in brackets.

Vertex angle α	ITO thickness (nm)	Deposition time (s)	$J_{ph\,loss}$ (mA/cm^2)
70° (near ideal value)	72.2	200.1	5.5
75° (sample A1)	72.5	190.6	5.5
80° (sample B1)	73.0	181.7	5.5
Flat structure	78.9	126.0	9.4

Table 5.5 – Minimum values of $J_{ph\,loss}$, corresponding ITO thicknesses, and required deposition times calculated for system of thin films on c-Si wafer illustrated in Fig. 5.18. Results for pyramidal texture with vertex angle near the ideal value ($\alpha = 70°$), for sample A1 ($\alpha = 75°$), for sample B1 ($\alpha = 80°$), and for structure on the flat wafer are presented.

5.3.4 Silicon heterojunction solar cells

Four SHJ solar cells fabricated by Igor P. Sobkowicz on textured wafers of type B1 using the structure presented in Fig. 2.1 are studied to compare their performance. As shown in the schematic figure, a p-layer gradient is used. Indeed,

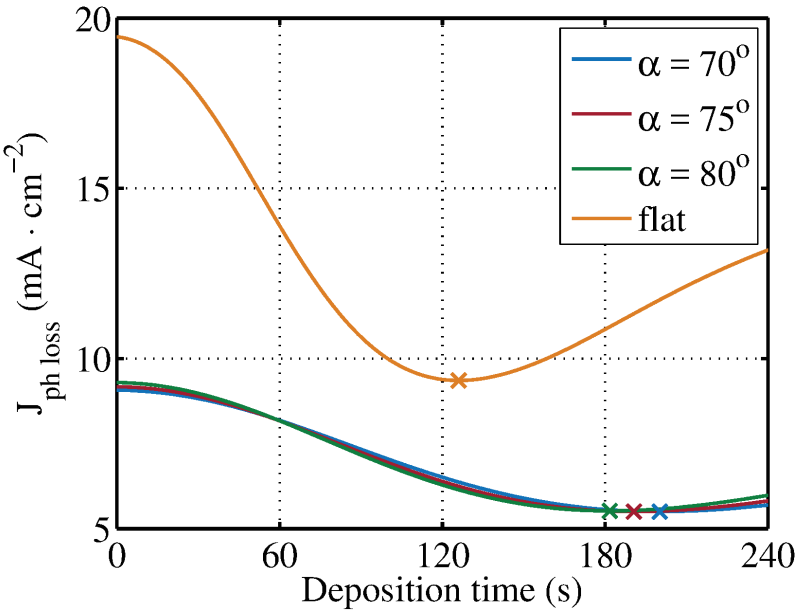

Figure 5.20 – Results for the thin film system from Fig. 5.18 on the pyramidal textured front surface of the c-Si wafer. $J_{ph\,loss}$ as a function of the ITO deposition time with marked minimum for pyramids with vertex angles $\alpha = 70°$, $75°$, and $80°$, respectively, and for reference flat geometry with normal angle of incidence. Crosses indicate the minimum of $J_{ph\,loss}$ for each geometry.

results reported by Igor P. Sobkowicz have shown that using a doping gradient in the case of the p-layer leads to better cell performance by: i) reducing the amount of Fermi-level related created defects at the a-Si:H/c-Si interface, and ii) protecting the interface from degradation upon ITO sputtering when finalizing solar cells [43]. Therefore, while the whole back side of the solar cell and the (p)a-Si:H layer were kept constant in terms of deposition conditions and thickness, the (p++)a-Si:H layer thickness was varied to obtain the overall p-layer thickness p [sum of (p)a-Si:H and (p++)a-Si:H layer thickness] of 10, 13, 16, and 19 nm, respectively.

Light current density-voltage (JV) characteristics in Fig. 5.21 show that a p-layer thickness of 16 nm is optimal to get the maximum conversion efficiency. This is partially due to the higher open circuit voltage (V_{OC}) but also due to enhanced carrier collection. Despite the almost constant short-circuit current density (J_{SC}), the fill factor (FF) depends on the p-layer thickness and its maximum is 76.1 % at $p = 16$ nm.

This observation clearly demonstrates the importance of the precise control of the thicknesses of deposited thin films since a few nm difference in p-layer

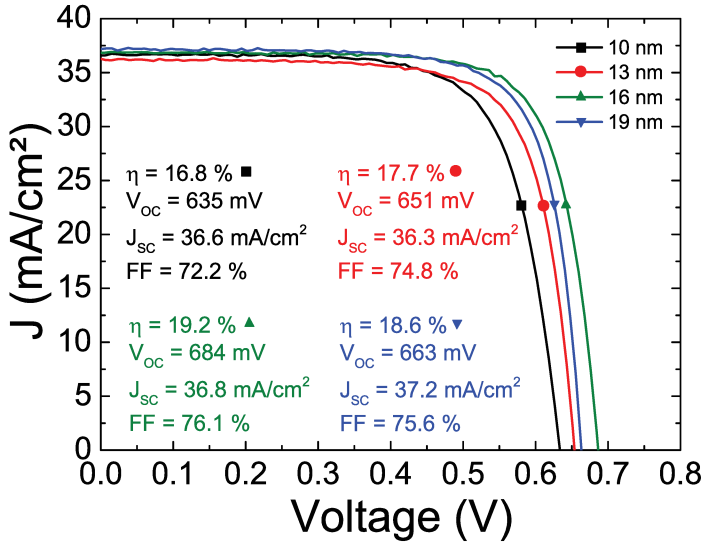

Figure 5.21 – Light JV characteristics of SHJ solar cells fabricated on textured wafers of type B1 as a function of the p-layer thickness [43, 85].

thickness leads to a change in the efficiency of the cells by a 2.4 % in absolute value (19.2 % for $p = 16$ nm in contrast with 16.8 % for $p = 10$ nm). Spectroscopic ellipsometry is therefore a valuable method for a precise control of deposited thin film thicknesses and solar cell efficiency optimization.

5.4 Chapter key results

Crystalline silicon wafers with different pyramidal textures resulting from various texturing conditions were studied. Samples without additional post-treatment seem to be more suitable for photovoltaic applications from an optical point of view, since additional post-treatment increases the undesirable reflectance. A designed simple model for reflectance based on dominant double-reflection from opposite pyramidal facets was proved to agree with experimental measurements.

Differences in vertex angles of studied pyramids were presented. We associate this with steps at atomic level revealed by HRTEM. These atomic steps could have a detrimental impact on the passivation quality and hence on the overall solar cell efficiency. Moreover, different pyramidal surfaces with respect to vertex angles influence deposition rates and resulting thin film thicknesses. Careful optimization of multi-layer system with respect to particular pyramidal surface, together

with the accurate thickness characterization is thus required.

A model based on calculation of parasitic absorptions in each layer, together with the total reflectance of the structure on the front surface of the solar cell was designed for optimization of thicknesses of thin films on pyramids. We demonstrated that optimal parameters of multi-layer structure vary depending on used surface geometry. Thanks to this study, we were able to optimize our SHJ solar cell base structure shown in Figure 2.1(a), and choose an optimal p-layer thickness of 16 nm. The thickness optimization has led to improvement of SHJ solar cell efficiency by 2.4 % in absolute value, up to 19.2 % on a 2×2 cm^2 surface, thus proving the paramount importance of accurate a-Si:H layer thickness monitoring to reach higher performance.

6 Results for silicon nanowires

Outline

Randomly oriented silicon nanowires belong to even more challenging structures for light-trapping enhancement than pyramidal ones. A concept of radial junction built over silicon nanowires benefits from the fact, that collection of charge carriers occurs in a radial direction, while the light is absorbed mainly in axial direction of nanowires. This enables using a-Si:H absorber layers as thin as 100 nm, with a good light absorption preserved thanks to the sufficient length of nanowires (about $1-2\mu$m). This leads to material and cost savings. Furthermore, plasma-assisted vapor-liquid-solid method combined with low melting point Sn catalyst (described in details in Section 2.2) allows for a deposition on low-cost substrates as glass, flexible foils or plastics.

In this chapter, results obtained from material characterization and in-situ measurements of silicon nanowire growth are presented and discussed. Characterization of reference materials is described in Section 6.1, Section 6.2 is devoted to the characterization of substrate including Sn droplets, followed by the Section 6.3 on the modeling of the data measured in-situ during SiNWs growth.

6.1 Characterization of used materials

Before analysis of in-situ data measured during Sn droplet formation and SiNW growth, optical functions of used materials (namely Corning glass substrate, aluminum doped ZnO, and Sn) have to be determined. Determination of optical functions in spectral range $450-850$ nm is sufficient due to the limited spectral range of Mueller matrix ellipsometer installed on the reactor and used for in-situ measurements.

Optical function for Corning glass was provided by the Corning company and it is shown in Fig. 6.1.

Aluminum doped ZnO deposited on Corning glass acts as back contact for radial junction devices. Its optical functions were obtained from independent measurements of a reference sample with a spectral Mueller matrix ellipsometer. Reference sample consisted of ZnO:Al layer of nominal thickness of 1 μm deposited by RF magnetron sputtering on 1 mm thick Corning glass substrate. The sample was measured by Mueller matrix ellipsometer MM16 in spectral range 440 - 1000 nm (2.818 - 1.240 eV) at three different angles of incidence ($AOI = 50°, 60°,$ and $70°$). All three measured spectra were modeled simultaneously by multi-layer optical model shown in Fig. 6.2. The model consists of 1 mm thick Corning glass substrate ($L1$) covered by the ZnO:Al layer ($L2$). Surface roughness ($L3$) is represented by the Bruggeman effective medium approximation [71] containing 50 % of ZnO:Al and 50 % of void. The optical constants of ZnO:Al were modeled, in the required spectral range of 450-850 nm (spectral range of ellipsometer installed on the reactor), by the combination of the Cauchy transparent (4.83) and

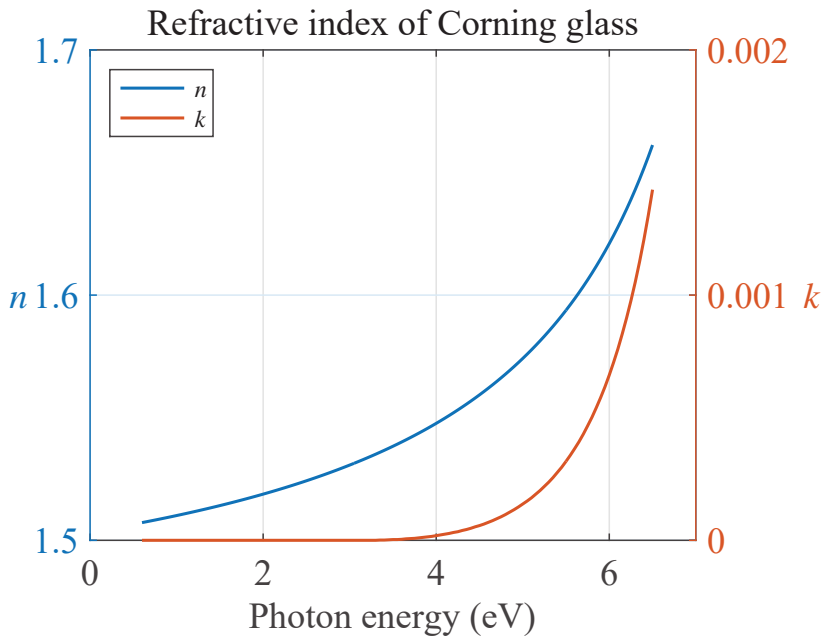

Figure 6.1 – Real and imaginary parts n and k of Corning glass refractive index as a function of photon energy.

Drude (4.84) terms. Parameters of these terms were used as free fitting parameters together with the thickness of the ZnO:Al layer ($L2$) and that of the roughness layer ($L3$). Figure 6.3 shows good agreement between measured data and model fitted to measured data for all three angles of incidence simultaneously.

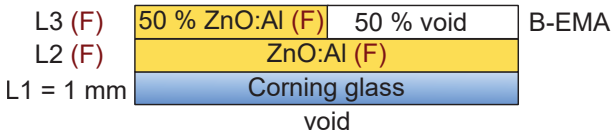

Figure 6.2 – Multi-layer optical model consisting of 1 mm Corning glass substrate ($L1$), the aluminum doped ZnO layer ($L2$), and surface roughness modeled by B-EMA containing 50 % of ZnO:Al and 50 % of void ($L3$). Red symbols F mark the free fitting parameters which are the thicknesses of layers $L2$ and $L3$, and the optical function of ZnO:Al.

Resulting optical function of ZnO:Al (see solid lines in Fig. 6.4) was used as the initial one in the model of Sn droplets formation (see Fig. 6.12 in the following Section 6.2). However, the parameters of the ZnO:Al optical function had to be slightly adapted to correspond to the material under deposition conditions in the reactor. The first spectrum measured in-situ in the reactor after Sn droplets

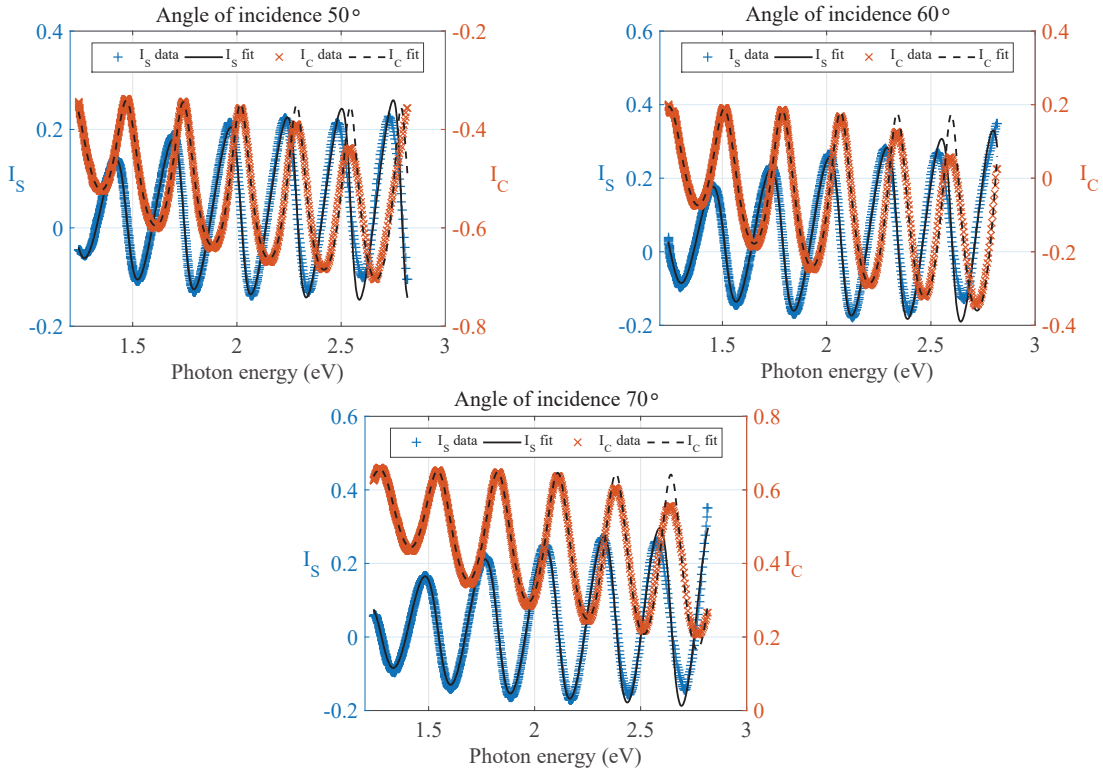

Figure 6.3 – Measured (symbols) and modeled (lines) values of I_S (blue) and I_C (orange) for angle of incidence (a) $50°$ (b) $60°$, and (c) $70°$.

formation (see Fig. 6.14 in the following Section 6.2) was therefore used as the reference for ZnO:Al under deposition conditions. In the firs step, the parameters of ZnO:Al optical function were used as free fitting parameters in model in Fig. 6.12 to obtain optical function of ZnO:Al under conditions in the reactor. Figure 6.13 shows very good agreement between model and data measured after Sn droplets formation and before SiNW growth (marked as 0 min of SiNW growth in this figure). Resulting function shown by dashed lines in Fig. 6.4 was then used in all following models of Sn droplets formation and SiNW growth. Note that a difference between the initial and adapted ZnO:Al optical function is in the studied spectral range of $450 - 850$ nm minimal.

A reference sample of 50 nm (nominal thickness) of Sn thermally evaporated on 1 mm thick Corning glass was used to determine the optical functions of Sn. The sample was measured from both sides (first with Sn layer on the top and then the sample was flipped upside down) using spectroscopic ellipsometer Uvisel. The measurement was performed in the spectral range $0.7 - 4.6$ eV with an increment of 0.025 eV and at the angle of incidence of $69.8°$. Both spectra were modeled using optical multi-model with bound parameters. Figure 6.5 shows

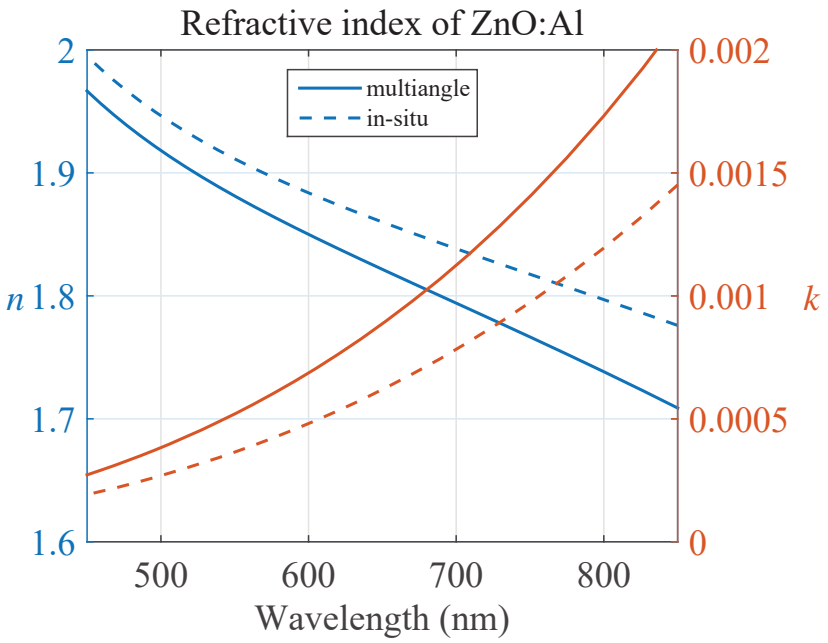

Figure 6.4 – Real (blue) and imaginary (orange) parts n and k, respectively, of ZnO:Al refractive index obtained from simultaneous modeling of multi-angle measurement of reference sample (solid lines) and from sample measured in-situ in the reactor under real deposition conditions (dashed lines).

the structure of the multi-model. Model $M1$ corresponds to the sample with the Sn layer on top of Corning glass, while model $M2$ represents the sample turned upside down. Both models consist of Corning glass of thickness $L1 = 1$ mm, Sn layer of thickness $L2$, and roughness layer of thickness $L3$ modeled by B-EMA consisting of 50 % of Sn and 50 % of void. Free fitting parameters are thicknesses of the layers $L2$ and $L3$ and parameters of the Sn optical function. Model of the Sn optical function consists of three Lorentz harmonic oscillators (4.85). All the free fitting parameters were bound between model $M1$ and $M2$ as indicated by arrows in Fig. 6.5. Figure 6.6 shows good agreement between measured data and model. Resulting refractive index is shown in Fig. 6.7.

To asses the influence of processes occurring during sample treatment in the reactor (such as increasing temperature and H_2 plasma environment) on Sn optical function, we performed an in-situ measurements of a test sample in the reactor. The sample consisted of 50 nm thick Sn layer evaporated on Corning glass. Figure 6.8 shows ellipsometric data measured every half minute during increasing the temperature to $250\,°C$ (near process temperature). This process step took around 13 min. After reaching the temperature, H_2 plasma at nominal RF power 20 W (corresponding to 100 mW/cm^2) was applied for about 34 min. The high

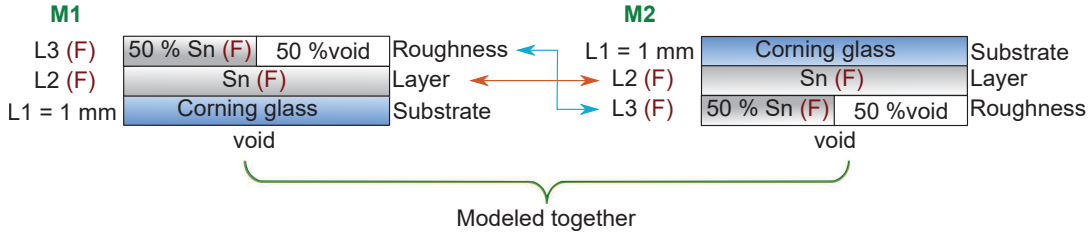

Figure 6.5 – Multi-layer optical models consisting of 1 mm Corning glass substrate ($L1$), the Sn layer ($L2$), and surface roughness ($L3$) modeled by B-EMA containing 50 % of Sn and 50 % of void. Model $M1$ corresponds to the reference sample with Sn layer on top of Corning glass. Model $M2$ represents the same sample turned upside down. Red symbols F mark the free fitting parameters which are the thicknesses of layers $L2$ and $L3$, and the optical function of Sn. Arrows mark the bound parameters.

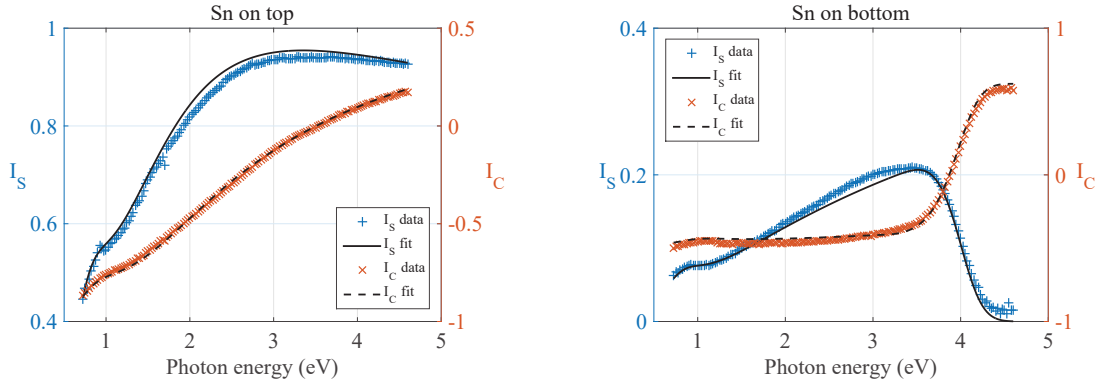

Figure 6.6 – Measured (symbols) and modeled (lines) values of I_S (blue) and I_C (orange) for reference sample (a) with Sn layer on the Corning glass and (b) reference sample turned upside down. Both spectra have been fitted simultaneously.

RF power was chosen to increase the process of Sn reduction and metal droplets formation since Sn layer of 50 nm is much thicker than that of 2 nm usually used. Figure 6.9 shows ellipsometric data measured every half minute during H_2 plasma treatment. The figure was limited to first 10 min of treatment to make the data easier to distinguish since no more changes appeared later in the process.

We can see that ellipsometric data doesn't change during increasing the temperature (see Fig. 6.8) suggesting no important changes of the sample despite a temperature exceeding the melting point of a bulk Sn (232 °C). In contrary, there is a significant change in ellipsometric data measured during H_2 plasma treatment (see Fig. 6.9). We attribute this to a removing of a surface oxide which probably prevented Sn from melting during the temperature increase. We expect Sn

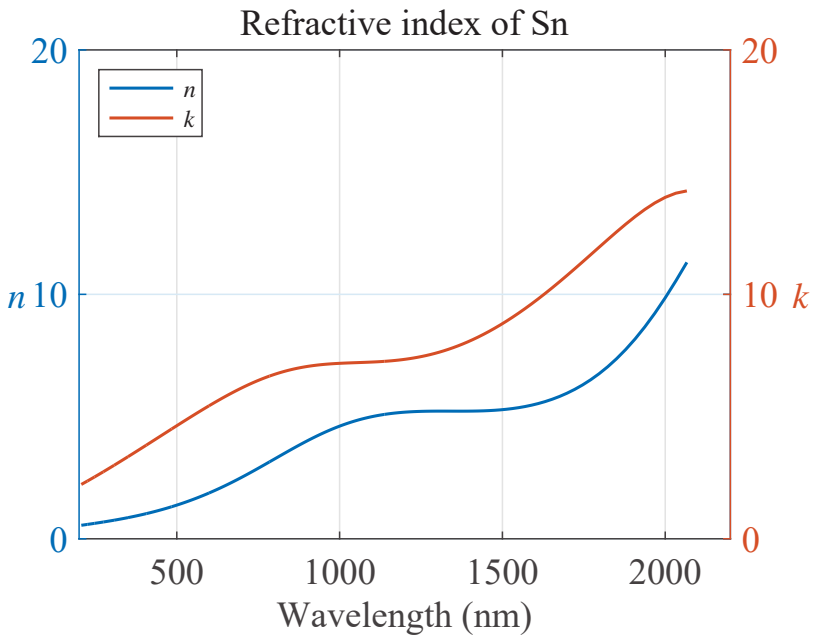

Figure 6.7 – Real (blue) and imaginary (orange) parts n and k, respectively, of Sn refractive index obtained from bound multi-model of reference sample.

droplets to be formed at this point. The change is very fast and happens between 5^{th} and 7^{th} measured spectrum i.e. between 2.5 and 3.5 minutes of the treatment. In contrast, 2 min of H_2 plasma treatment is sufficient for Sn droplets formation under our standard conditions described in Section 2.2.1. We asses this to the fact that formation of metal droplets from thiner and less oxidized 2 nm Sn layer is faster than that from 50 nm thick layer of the test sample.

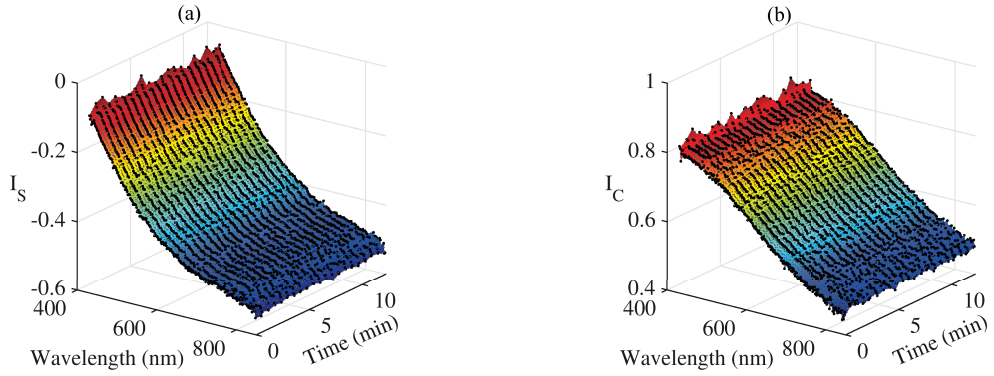

Figure 6.8 – Evolution of ellipsometric data (a) I_S and (b) I_C with deposition time measured during increasing the temperature to $250\,°\text{C}$.

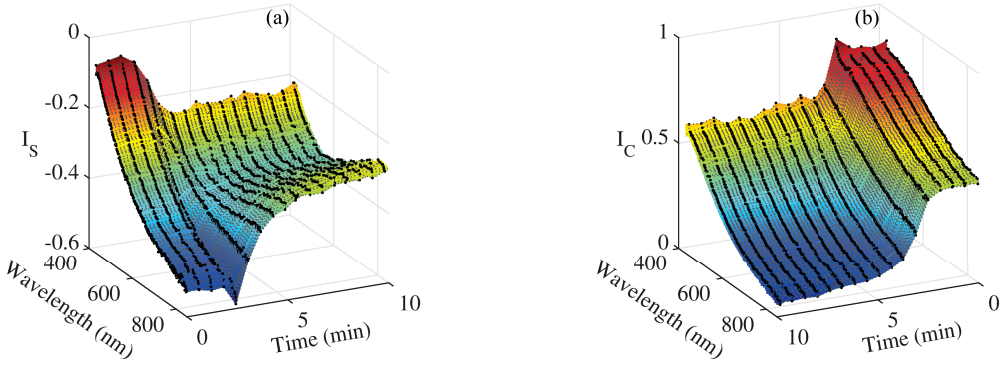

Figure 6.9 – Evolution of ellipsometric data (a) I_S and (b) I_C with deposition time during first 10 min of H_2 plasma treatment at $250\,°C$. The direction of time axis was reversed in case (b) to improve the visibility of I_C data.

It is not possible to use the same optical function of Sn to model all measured spectra, since changes of the material during H_2 plasma treatment are reflected also by significant changes in ellipsometric data. Figure 6.10(a) shows the real and imaginary parts of refractive index of Sn obtained from modeling of the 1^{st}, 6^{th}, and 11^{th} spectrum from Fig. 6.9, corresponding to 0, 3, and 6 min of H_2 plasma treatment, respectively. Model $M1$ from Fig. 6.5 was used to obtain those optical functions. Refractive index marked as 0 min (see dashed-dotted line in Fig. 6.10(a)) corresponds to the Sn covered by a SnO_2 shell at the very beginning of H_2 plasma treatment. Refractive index marked as 3 min (see dotted line in the same figure) corresponds to the material during biggest change of ellipsometric data (see 6^{th} spectrum in Fig. 6.9). Refractive index marked as 6 min (solid line in Fig. 6.10(a)) was obtained from ellipsometric data well stabilized after change occurring at 3 min of plasma treatment. Figure 6.10(b) shows a very good agreement between modeled and measured data. We decided to use refractive index obtained at 6 min of H_2 plasma treatment in further models, since we assume that this function represents best the melted Sn which forms droplets for silicon nanowire growth.

Figure 6.11 compares refractive index of melted Sn obtained at 6 min of H_2 plasma treatment (solid line) and that of solid Sn (dashed line) established from reference sample using bound multi-model shown in Fig. 6.5. The limited spectral range corresponds to that of our Mueller matrix ellipsometer installed on the reactor. We can see that both functions differ from each other and it is necessary to use the proper one (marked as in-situ 6 min in Fig. 6.11) adapted to material under real conditions in the reactor during the fabrication process.

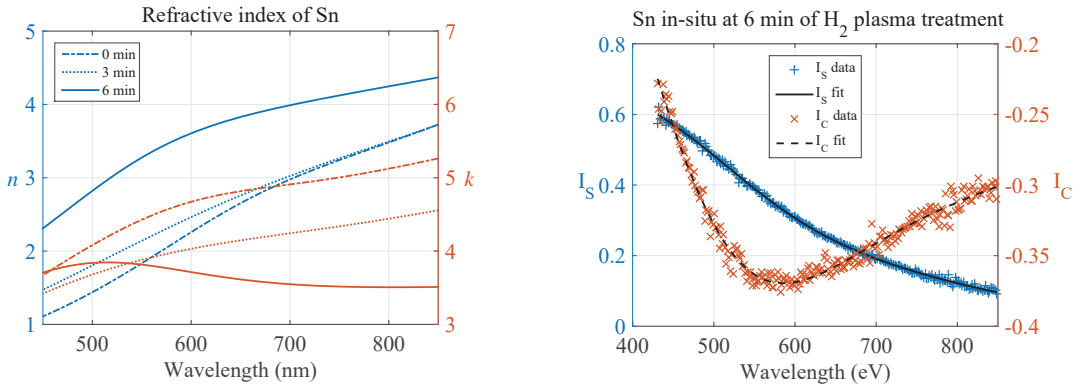

Figure 6.10 – (a) Real (blue) and imaginary (orange) parts n and k, respectively, of Sn refractive index obtained from ellipsometric data measured in-situ in the reactor during H_2 plasma treatment of the test sample at 0, 3, and 6 min, respectively. (b) Measured (symbols) and modeled (lines) values of I_S (blue) and I_C (orange) test sample at 6 min of H_2 plasma treatment

.

6.2 Characterization of substrate before nanowire growth

At first, the Sn droplets were formed after 2 min of H_2 plasma treatment (before the start of the nanowire growth, marked as 0 min of SiNW growth) and measured in-situ during the fabrication process in the reactor. Figure 6.12 shows a schematic illustration of the sample and corresponding multi-layer optical model consisting of 1 mm thick Corning glass substrate covered by the ZnO:Al layer of nominal thickness of 2 μm, while Sn droplets are represented by the B-EMA containing Sn and void. Optical functions of Corning glass, ZnO:Al and Sn were obtained from independent measurements of reference samples as described in Section 6.1.

The model was fitted to the experimental data using the Levenberg-Marquardt least-square minimization algorithm implemented in the DeltaPsi2 software (Horiba Scientific). The following fitting error function χ^2 was used as a criterion for the least square algorithm [80] [as compared to previously used one in Eq. (5.6)]:

$$\chi^2 = \frac{1}{(2M - N - 1)} \cdot \left[\sum_{k=1}^{M} \frac{\left(M_{33,k}^{meas} - M_{33,k}^{mod}\right)^2}{\left(\sigma_{M_{33,k}}\right)^2} + \sum_{k=1}^{M} \frac{\left(M_{43,k}^{meas} - M_{43,k}^{mod}\right)^2}{\left(\sigma_{M_{43,k}}\right)^2} \right], \quad (6.1)$$

where M_{33} and M_{43} correspond to the elements of the normalized Mueller matrix. Superscripts $meas$ and mod stand for the measured and modelled values,

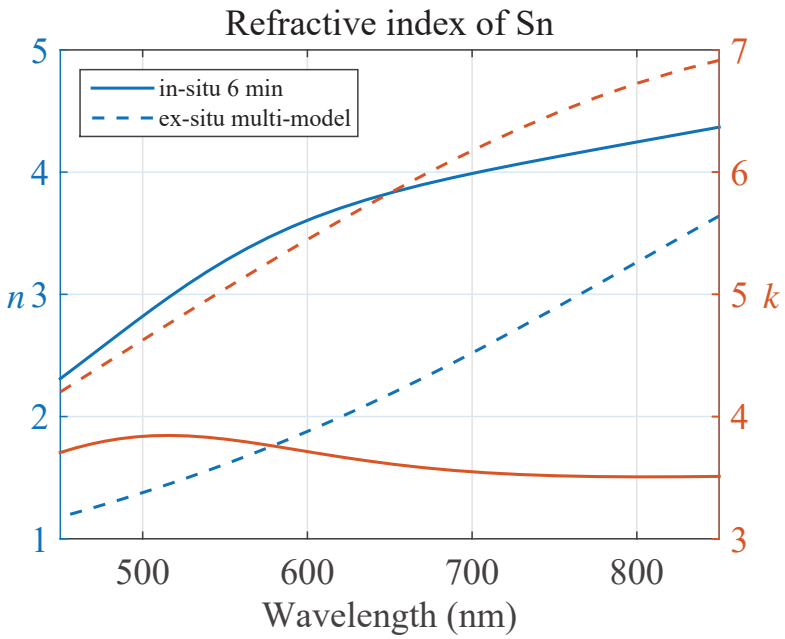

Figure 6.11 – Comparison of real (blue) and imaginary (orange) parts n and k, respectively, of Sn refractive index obtained from in-situ measurements after 6 min of H_2 plasma treatment and that obtained from bound multi-model of reference sample as shown in Fig. 6.7. Spectral range corresponds to that of Mueller matrix ellipsometer installed on the reactor for in-situ measurements

.

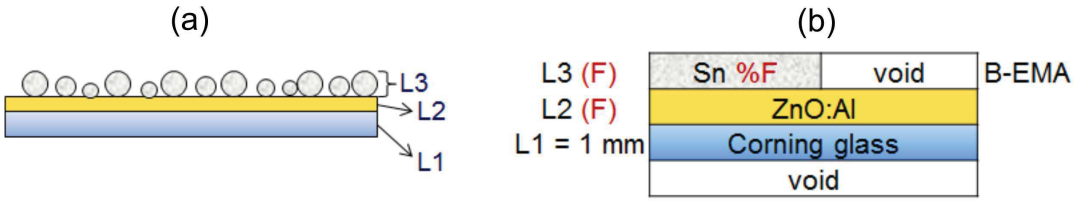

Figure 6.12 – (a) Schematic illustration of the Sn droplets formation after 2 min of H_2 plasma treatment. (b) Multi-layer optical model consisting of 1 mm Corning glass substrate ($L1$), the aluminum doped ZnO layer ($L2$), and Sn droplets modeled by B-EMA containing the Sn and void ($L3$). Red symbols F mark the free fitting parameters which are the thicknesses of layers $L2$ and $L3$, and the volume fraction of Sn.

respectively. $\sigma_{i,k}$ represents the estimated measurement error, which is set by the software at a constant value of 0.01. The sum is calculated over the measured spectrum. M stands for the number of spectral points and N is the number of

fitting parameters. In this case, fitting parameters are the thickness of the ZnO:Al layer ($L2$), the thickness of the layer $L3$ and the volume fraction of Sn in the layer $L3$ (marked by red symbols in the Fig. 6.12).

Figure 6.13 shows a very good agreement between the measured (symbols) and modeled (lines) values of Mueller matrix elements for the Sn droplets formed after 2 min of H_2 plasma treatment (marked as 0 min of SiNW growth) and for the 4 min of SiNW growth (which is discussed in the next section 6.3). The resulting thickness of the ZnO:Al layer obtained from the model in Fig. 6.12 is 2.23 μm. The thickness of the $L3$ layer consisting of 12.4 % of Sn and 87.6 % of void is 21.1 nm. The amount of Sn in this layer corresponds to the 2.6 nm thick layer of pure Sn. This value agrees well to the expected 2 nm nominal thickness of evaporated Sn film. The value of the fitting error function χ^2 defined by (6.1) is 3.2. Obtained results confirm that designed model is appropriate for description of Sn droplet formation.

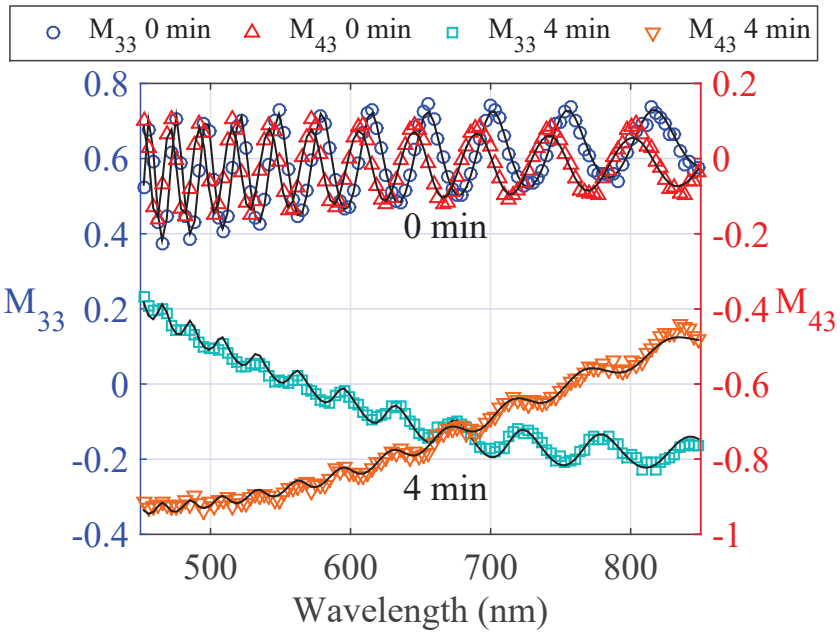

Figure 6.13 – Measured (symbols) and modeled (lines) Mueller matrix elements M33 and M43 as a function of the wavelength of incident light for sample of Sn droplets after 2 min of H2 plasma treatment before the nanowire growth (0 min of SiNW growth) and for the sample after 4 min of SiNW growth.

6.3 In-situ characterization of silicon nanowire growth

The SiNWs were grown from the Sn droplets by plasma-enhanced VLS process in a PECVD reactor as described in Section 2.2.1 and the samples were measured in-situ every minute during growth. Figure 6.14 shows the evolution of measured Muller matrix ellipsometric data with the deposition time. Measurements were performed from Sn droplets formation by H_2 plasma treatment corresponding to 0 min of SiNW growth (marked by blue curve in Fig. 6.14) until the end of nanowire growth after 10 min. The direction of the time axis was reversed to make the data easier to distinguish. We can observe gradual changes in measured data demonstrating the changes of optical properties of the sample connected to the structural evolution during SiNW growth.

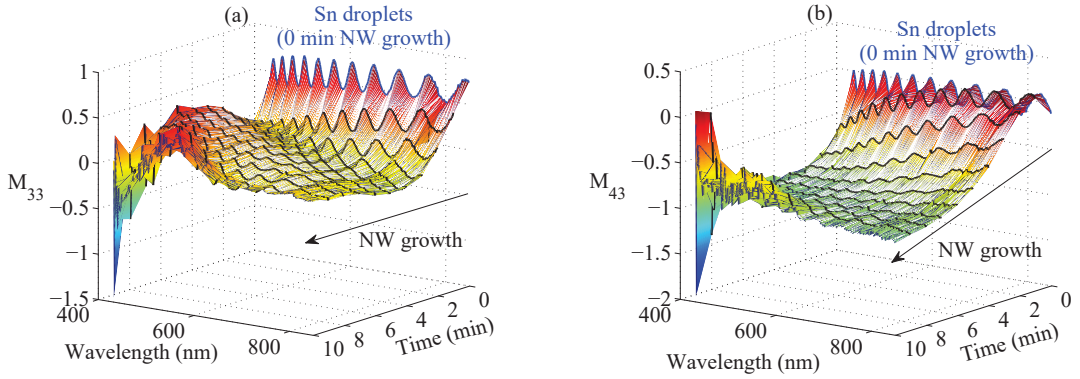

Figure 6.14 – Evolution of Mueller matrix elements (a) M_{33} and (b) M_{43} with deposition time starting from Sn droplets formation at 0 min of SiNW growth (blue curve) and continuing with SiNW growth measured every 1 min (black curves) up to 10 min.

Optical modeling of Mueller matrix ellipsometry data (see Fig. 6.14) allows us to trace the sample deposition step by step. Models start from a relatively simple model of the substrate with Sn droplets presented in Fig. 6.12 and continue to more complex versions for growing nanowires. Best fitted parameters of each spectrum have been used as initial parameters for the following one. Each spectrum has been analyzed thoroughly to assess the accuracy of the used multilayer optical model and the quality of the fit. We have added additional layers only when the current model was not able to provide satisfactory fit of the measured data. This enabled us to preserve a good quality of fits across the whole set of measured spectra and to obtain trends for the silicon deposition.

Since only approximately 1 of 100 initial Sn droplets will lead to growth of

a long SiNW [86], the rest of Sn droplets leads to a short SiNW growth and is gradually being buried in the hydrogenated amorphous silicon which is being deposited on the sample surface. We expect that the nanowires consist of a crystalline silicon core covered by a thin a-Si:H surface layer, which is formed during the growth [86]. Moreover, there is a large amount of a-Si:H being deposited on the sample surface in between the nanowires and gradually burying Sn droplets and short nanowires which stopped to grow during the process. Due to this and due to a limited spectral range of our in-situ instrument (450 - 850 nm corresponding to 1.45 - 2.75 eV), we decided to use only a-Si:H in optical models to avoid unwelcome correlations between different forms of silicon material (amorphous, microcrystalline, and crystalline).

Figure 6.15 shows a schematic illustration of the sample and the corresponding multi-layer optical model, which was applied from the beginning of the SiNW growth up to 3 min of the growth. The model consists of 1 mm thick Corning glass substrate ($L1$) covered by the ZnO:Al layer of thickness $L2 = 2.23\,\mu$m established from the previous analysis of the sample before SiNW growth. Layer $L3$ containing the B-EMA consisting of the Sn, void and a-Si:H, represents the Sn droplets partially buried by deposited hydrogenated amorphous silicon. Dielectric functions of a-Si:H were obtained from earlier characterization of a hydrogenated amorphous silicon thin film prepared at LPICM [38] and modelled using Tauc-Lorentz model [65,66] (for more detailed information see Appendix A). Layers $L4$ and $L5$ consisting of the B-EMA of void and silicon represent the shortest very dense nanowires partially covered by a-Si:H, and medium length less dense nanowires, respectively. The thicknesses of layers representing nanowires don't have to correspond exactly to the real SiNW length due to approximation of B-EMA and correlations between thickness of each layer and volume fractions of materials in it. However, used effective medium describes well optical effects of random nanowires in specular reflection. Note that higher absorption of a-Si:H probably partially compensates scattering losses that are not included in our simplified model. In addition, Sn droplets on top of nanowires [illustrated in Fig. 6.15(a)] are not incorporated into layers $L4$ and $L5$ of optical model [see Fig. 6.15(b)], since their volume fractions are below sensitivity of ellipsometric measurements.

Starting from the fourth minute of the growth, one additional layer ($L6$) of B-EMA consisting of the void and silicon with different composition has been added to represent the effect of the longest and very sparse nanowires (see Fig. 6.16) and to preserve the good quality of the fit. Based on the analysis of the data, void was excluded from the layer $L3$ corresponding to the situation that Sn droplets and shortest nanowires with deposited a-Si:H completely fill the layer. This model agrees very well with the experimental data as illustrated in Fig. 6.13 for 4 min of SiNW growth.

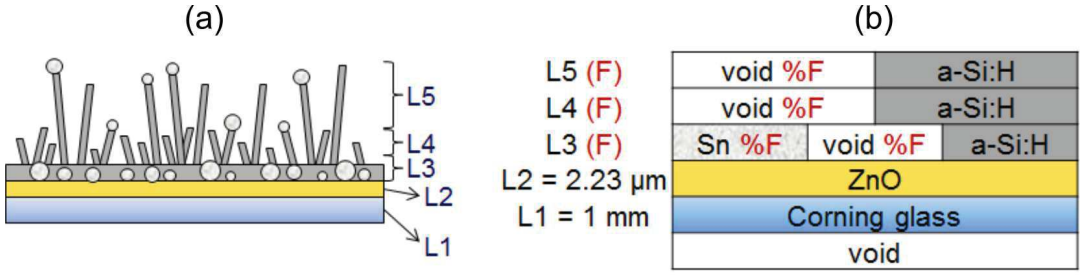

Figure 6.15 – (a) Schematic illustration of the first stages of silicon nanowire growth by the plasma-assisted VLS method using Sn droplets as the mediator for the growth. (b) Multi-layer optical model consisting of 1 mm Corning glass substrate ($L1$), the aluminum doped ZnO layer of thickness of 2.23 μm ($L2$), Sn droplets partially buried in the silicon represented by the B-EMA consisting of Sn, void, and silicon ($L3$), the $L4$ layer formed by B-EMA of void and silicon representing short dense nanowires, and the $L5$ layer representing longer, less dense nanowires. Red symbols mark the free fitting parameters.

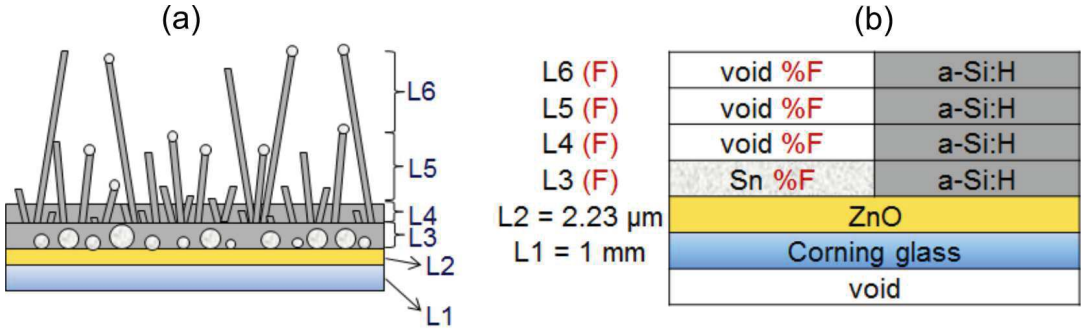

Figure 6.16 – (a) Schematic illustration of the later stages of silicon nanowire growth by the plasma-assisted VLS method using the Sn droplets as the catalyst for the growth. (b) Multi-layer optical model consisting of 1 mm Corning glass substrate ($L1$), the aluminum doped ZnO layer of thickness of 2.23 μm ($L2$), a mixture of Sn droplets and silicon represented by B-EMA consisting of Sn and silicon ($L3$), the $L4$ layer formed by B-EMA of void and silicon representing the shortest very dense nanowires gradually being filled by a-Si:H, the $L5$ layer representing longer less dense nanowires, and $L6$ layer representing the longest very sparse nanowires. Red symbols mark the free fitting parameters.

Figure 6.17 shows the best fit parameters describing the lower Si layer $L3$ as a function of the deposition time. The error-bars, corresponding to a standard deviation σ_{SD} representing a confidence interval of 68.3 %, were obtained from analysis of results of Levenberg-Marquardt least-square minimization algorithm

performed by the DeltaPsi2 software (Horiba Scientific). The Sn droplets are partially buried in silicon (up to 3 min) and starting from 4 minute the layer is filled only by a mixture of Sn and silicon. The void fraction in layer $L3$ gradually decreases with the increasing deposition time and drops to zero for 4 min [see Fig. 6.17]. Therefore, it was excluded from the model for the 4 min and later (see Fig. 6.16). The volume fraction of Sn increases with the deposition time, however this value is anti-correlated with the thickness of $L3$ layer, which decreases as a function of the NW growth time [see blue curve in Fig. 6.17(b)]. This leads to the rather stable amount of Sn calculated as a product of the $L3$ layer thickness and Sn volume fraction [see orange curve in the Fig. 6.17(b)] which is close to the expected nominal thickness of 2 nm of pure Sn layer and does not change significantly during the NW growth.

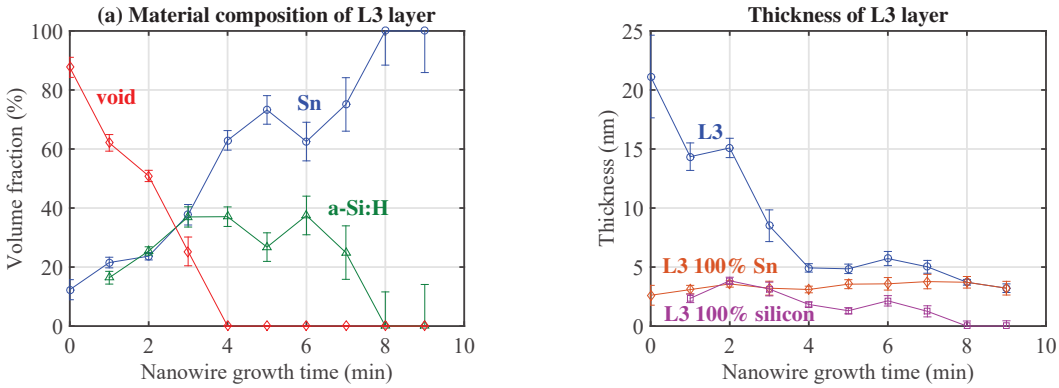

Figure 6.17 – Best fit parameters for the $L3$ layer representing the mixture of Sn droplets and silicon. (a) Volume fractions of Sn, void, and silicon as functions of the deposition time. (b) Thickness of the $L3$ layer as a function of the deposition time (blue curve), and the corresponding thickness of the effective dense Sn layer (purple curve).

Figure 6.18 shows results for layer $L4$, representing the shortest very dense nanowires. This layer contains a very large amount of silicon [see Fig. 6.18(a)] reaching 100 % from the 4 min. It can be explained by a complete fill up of an intermediate space by the silicon, including very short nanowires and bases of longer nanowires buried in a-Si:H. The thickness of this layer gradually increases with the deposition time as shown in Fig. 6.18(b). Increasing effective amount of silicon calculated as a product of the $L4$ layer thickness and silicon volume fraction [see purple curve in the Fig. 6.18(b)] results in the effective growth rate around 0.1 nm/s which is faster than the a-Si:H growth rate on a planar substrate (0.07 nm/s) at these plasma and gas conditions. This indicates that not only a-Si:H is deposited but also SiNWs are grown.

Figure 6.19 shows results for the $L5$ layer containing the medium length,

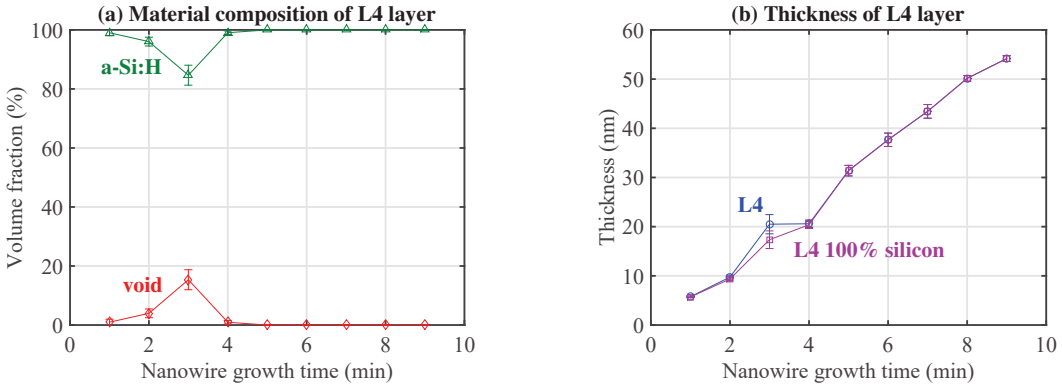

Figure 6.18 – Best fit parameters for the $L4$ layer representing the shortest and densest nanowires in the matrix of a-Si:H. (a) Volume fractions of silicon and void as functions of the deposition time. (b) Thickness of the $L4$ layer as a function of the deposition time (blue curve), and the corresponding thickness of the effective dense silicon layer (purple curve).

less dense nanowires. This is represented by the smaller amount of silicon [see Fig. 6.19(a)] than in the previous layer $L4$. $L5$ is the most upper layer up to 3 min, while later even longer nanowires represented by the $L6$ layer appear. Insertion of the $L6$ layer is the source of the sudden jump in the fit results for the $L5$ layer between 3 and 4 min. The thickness of $L5$ layer gradually increases with the deposition time before (1-3 min) and after (4-9 min) the model is changed to take into account longest nanowires and to keep the same quality of the fit. The purple curve representing the effective thickness of pure silicon layer calculated as a product of the $L5$ layer thickness and silicon volume fraction shows gradual increase of amount of silicon with the deposition time.

Finally, Figure 6.20 shows best fit parameters for the $L6$ layer representing the longest, very sparse nanowires. The amount of silicon is very low in this layer as shown in Fig. 6.20(a), corresponding to the low density of nanowires. The thickness of this layer gradually increases with the deposition time from 4 min [see Fig. 6.20(b)] when this layer is introduced into the optical model. Very low effective thickness of pure silicon layer [see purple curve in Fig. 6.20(b)] calculated as a product of the $L6$ layer thickness and silicon volume fraction results from the very low density of nanowires and hence small amount of deposited silicon.

Figure 6.21(a) summarizes the trends for the deposition of silicon determined from results above. The amount of silicon in each layer is obtained as a product of layer thickness and silicon volume fraction in that layer. The total amount of silicon in all layers corresponds to the sum of all these thicknesses [red curve in Fig. 6.21(a)]. The total effective amount of deposited silicon corresponds to the thickness of continuous layer of 81 nm after 9 min growth [see red curve in

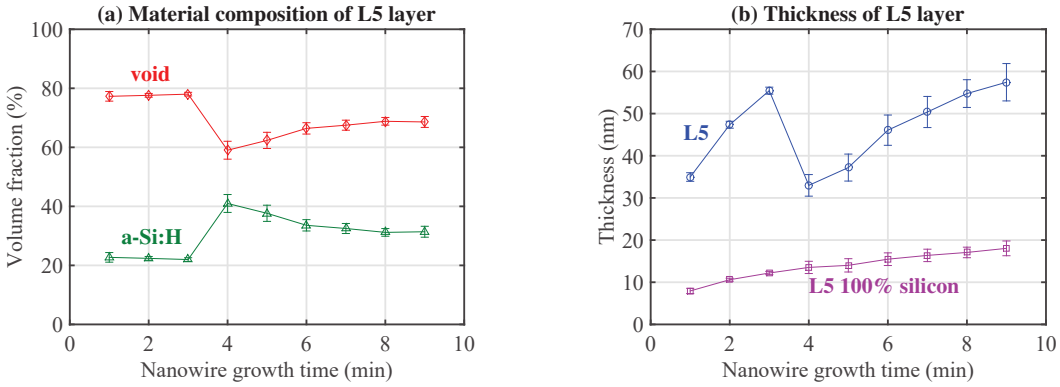

Figure 6.19 – Best fit parameters for the $L5$ layer representing the medium length, less dense nanowires. (a) Volume fractions of silicon and void as functions of the deposition time. (b) Thickness of the $L5$ layer as a function of the deposition time (blue curve), and the corresponding thickness of the effective dense silicon layer (purple curve).

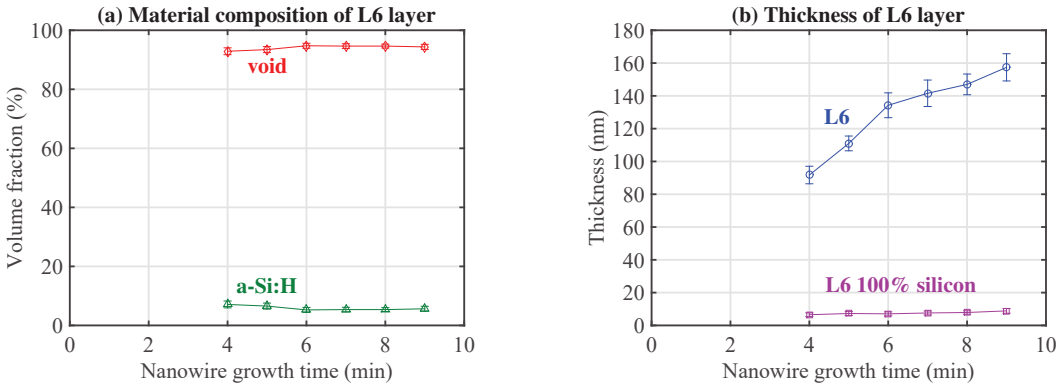

Figure 6.20 – Best fit parameters for the $L6$ layer representing the longest very sparse nanowires. (a) Volume fractions of silicon and void as functions of the deposition time. (b) Thickness of the $L6$ layer as a function of the deposition time (blue curve), and the corresponding thickness of the effective dense silicon layer (purple curve).

Fig. 6.21(a)]. This represents a combination of a-Si:H and SiNWs since the model can determine the total amount of deposited silicon but it is not very sensitive to differences between crystalline and amorphous phase due to a very limited spectral range (1.45 - 2.75 eV) of used in-situ instrument. However, knowing the individual deposition rates of a-Si:H and SiNWs enables to roughly estimate the relative amount of each material in the mixture.

For the simplicity, we will approximate the deposition rate of a-Si:H during the SiNW growth by that of pure a-Si:H deposited under the same conditions on flat substrate (around 0.07 nm/s [49, 87]). Thus, 9 min deposition of a-Si:H with this rate results in the layer of the thickness of 38 nm. The remaining 43 nm of the total silicon layer is formed by material of SiNWs (crystalline and/or microcrystalline silicon). An approximate growth rate of 1.67 nm/s for SiNWs can be estimated from 10 min deposition resulting in approximately 1000 nm long nanowires according to SEM [86, 87]. Assuming an area of 1 μm^2, the volume of 43 nm thick layer of material corresponds to the volume of 38 SiNWs of a diameter of 40 nm and an average length of 900 nm obtained after 9 min growth with the 1.67 nm/s deposition rate. The estimated density of 38 SiNWs per 1 μm^2 after 9 min growth is in a good agreement with Ref. 86 and corresponds to about 4.8 % of the sample volume fraction represented by silicon nanowires.

The red curve in Fig. 6.21 indicates a piecewise linear increase of silicon during the deposition. Two deposition rates of silicon can be determined from this curve as 0.16 nm/s and 0.11 nm/s, respectively [see Fig. 6.21(b)]. Both deposition rates are between the approximate growth rate of 1.67 nm/s of crystalline silicon nanowires estimated in the previous paragraph and that of pure a-Si:H deposited under same conditions on flat substrate, which is around 0.07 nm/s [49, 87] [for comparison see blue and green lines in Fig. 6.21(b)]. The higher deposition rate of 0.16 nm/s at the beginning of the process corresponds well to the production of a combination of growing SiNWs and a-Si:H deposited between them. The volume fraction of SiNWs can be estimated to be about 5.6 % using the formula:

$$f_{SiNWs} = \frac{v - v_1}{v_2 - v_1}, \tag{6.2}$$

where $v_1 = 0.07$ nm/s is the approximate deposition rate of a-Si:H, $v_2 = 1.67$ nm/s is the estimated growth rate of SiNWs, and v is the deposition rate of silicon determined from the red curve in Fig. 6.21(b) as 0.16 nm/s up to 6 min of deposition and 0.11 nm/s after 6 min of deposition. Later on, some Sn catalyst droplets are exhausted and stop producing nanowires [86]. This leads to the lowering of the general deposition rate to the value of 0.11 nm/s which corresponds to the approximate volume fraction of growing SiNWs calculated using (6.2) to be about 2.5 %. The estimated average SiNW volume fraction of 4.8 % established in the previous paragraph is well between the approximate vol-

ume fractions of 5.6 % and 2.5 % calculated from the total material deposition rates 0.16 and 0.11 nm/s, respectively.

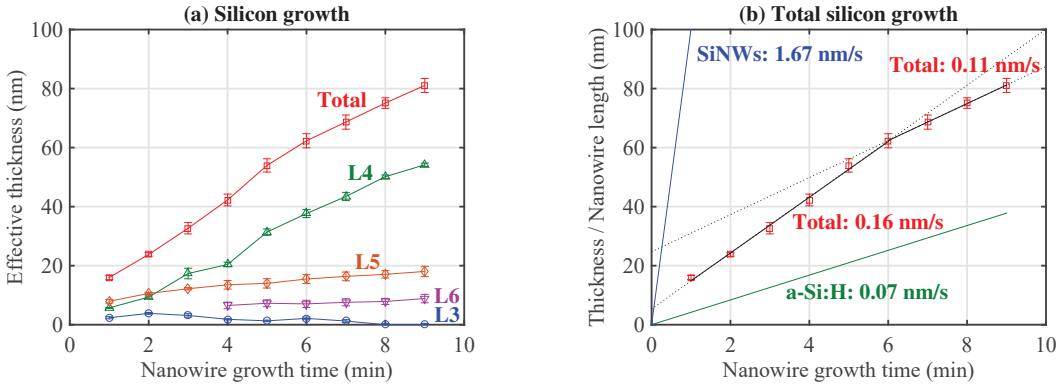

Figure 6.21 – Trends for the silicon deposition. (a) Evolution of the amount of silicon in each layer and its total sum (red curve) as a function of the deposition time. (b) Deposition rate of silicon established from the increase of the total amount of silicon in all layers (red points) in comparison with the deposition rate of pure a-Si:H (green) and crystalline silicon nanowires growth rate (blue) [87].

Straightforward dependence of the amount of silicon on the deposition time in Fig. 6.21 shows that we can trace the SiNW growth using a single parameter, and thus provide a tool for a better fabrication process control using in-situ ellipsometry. Moreover, average density of SiNWs can be estimated if sufficient structural information is known a priori (e.g. SiNW lengths and diameters).

6.4 Ex-situ characterization of silicon nanowires after growth

In this section we demonstrate that the difference between various silicon phases can be observed in the spectral range, which is beyond the capability of our in-situ Mueller matrix ellipsometer. The role of the crystalline silicon starts to be more important above the photon energy of 3 eV as illustrated in the Fig. 6.22. We have used scanning spectroscopic phase modulated ellipsometer Uvisel 2 with wider spectral range than MM16 Mueller matrix polarimeter for the ex-situ characterization of a sample of randomly oriented silicon nanowires after 8 min long deposition. Silicon nanowires were grown from Sn droplets directly on Corning glass substrate, this time without the ZnO:Al layer, under similar conditions as for the previous sample (see Section 6.3). Values of I_S and I_C measured in the spectral range of $0.8-5$ eV are presented by blue and red symbols in Fig. 6.22, together with results of optical models.

Model 1 is based on structure discussed in Section 6.3 using only a-Si:H, while Model 2 was derived from the Model 1 by including also crystalline and microcrystalline silicon as illustrated in Fig. 6.23. We can see in Fig. 6.22, that in the narrow spectral range corresponding to the range for in-situ measurements (highlighted by yellow color in the figure), Model 1 and Model 2 give almost identical results. However, there are peaks indicating the presence of crystalline and/or microcrystalline silicon above the photon energy of 3 eV. Model 1 which includes only a-Si:H (solid black curve) misses these peaks completely as shown in Fig. 6.22. Incorporation of crystalline and microcrystalline silicon into the Model 2 improves the quality of the I_C value fit in this region (see dashed black curve in Fig. 6.22).

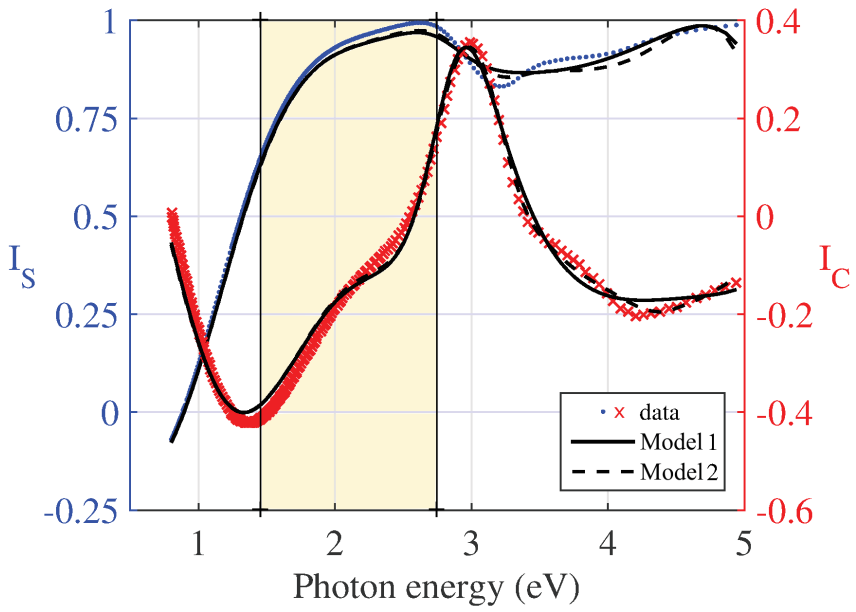

Figure 6.22 – Measured (symbols) and modeled (lines) values of I_S and I_C as a functions of the photon energy of incident light for sample of SiNWs on Corning glass measured ex-situ after 8 min growth. Model 1 is based on results obtained from in-situ modeling of similar sample and contains a-Si:H, while Model 2 includes also microcrystalline and crystalline silicon. Area highlighted by yellow corresponds to the spectral range of the MM16 Mueller matrix ellipsometer installed on the reactor.

Measurements in the wider spectral range including also the UV region are crucial to distinguish different phases of silicon (amorphous, microcrystalline, and crystalline). Thus, using only a-Si:H in optical models for Mueller matrix data measured during the deposition presented in Section 6.3 is sufficient due to

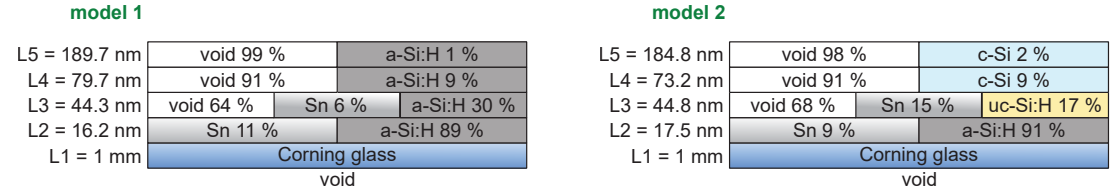

Figure 6.23 – Multi-layer optical models for analysis of ellipsometric data measured ex-situ in the spectral range of $0.8 - 5$ eV. (a) Model 1 containing only amorphous silicon phase (a-Si:H) is based on optical modeling of in-situ data measured on similar sample in Section 6.3. (b) Model 2 is derived from Model 1 by incorporation also hydrogenated microcrystalline (uc-Si:H) and crystalline (c-Si) silicon.

a limited spectral range of the measurements. Extension of the spectral range of in-situ measurements together with incorporation of microcrystalline and crystalline silicon into optical models will make these models more accurate and will enable tracing also the evolution of different silicon phases during SiNW growth.

6.5 Chapter key results

We have demonstrated for the first time in-situ monitoring and modeling of the Si nanowire growth using Mueller matrix data obtained by an ellipsometer installed on the reactor. We have shown that a straightforward optical model based on B-EMA simplifying the complex geometry of randomly oriented SiNWs can be used to interpret the data for process control purposes. Trends in the amount of deposited silicon together with effective deposition rates were obtained despite the limitations of proposed model and measured data discussed in the text. The observed piece-wise linear dependence of the silicon material deposition on the deposition time enables to trace the fabrication process in-situ and to control variable deposition conditions. Extension of the measurement range to include also UV region is crucial to distinguish between different phases of silicon (amorphous, microcrystalline, and crystalline).

Conclusions and perspectives

Conclusions

Optical methods (in particular spectroscopic and ellipsometric techniques) were successfully used for the characterization of both, widely used pyramidal textures as well as highly challenging randomly oriented silicon nanowires. These techniques provide us important informations which lead to solar cell improvement. Design of new optical models has been crucial for data analysis.

Comprehensive study of various pyramidal textures (resulting from different texturing recipes) and their impact on the solar cell design, fabrication, and performance has been carried out. Key findings regarding the influence of the surface textures on light-trapping, deposition rates and resulting thin film thicknesses as well as multi-layer design optimization have been discussed in Chapter 5. The crucial role of pyramid vertex angles has been demonstrated. Application of these findings leads to solar cell efficiency improvement.

Optical methods have also been used for growth monitoring and modeling of randomly oriented silicon nanowires. However, measurements of ellipsometric data in-situ during sample fabrication is not trivial. Challenges connected with the position of the sample in the reactor and signal to noise ratio have been overcome leading to successful measurements. Optical models simplifying the complex structure of samples has been designed to analyze measured Mueller matrix ellipsometric data. Developed models together with obtained trends for material deposition and deposition rates have been presented in Chapter 6. The amount of deposited material seems to be a suitable single parameter allowing to trace the fabrication process. Extension of the spectral range of measurements to cover also the UV region is crucial to distinguish between different silicon phases.

Perspectives

This thesis is the result of a collaboration between Nanotechnology Centre in Ostrava and Laboratoire de Physique des Interfaces et des Couches Minces in Palaiseau on developing models usable for the characterization of the photovoltaic devices and investigation of novel materials and nanostructures to increase energy conversion efficiency of solar cells. There are many interesting topics which can build on results achieved in this thesis.

In the near future, I would like to extend the optical model of multi-layer optimization of pyramidal front side of silicon heterojunction solar cells to cover also the back side of the structure. This will allow to include also back-side reflections and provide a complete model for multi-layer structure optimization of

pyramidal solar cells. The study of a complete structure can be further extended by including certain structural disorder and imperfections present in pyramidal based solar cells. That would provide a unique platform which can be used to study not only more general cases, but also tandem devices combined with pyramidal structures. One of the promising materials is perovskite, which is still studied in laboratories around the world as well as at LPICM. This would allow to profit from light trapping of pyramidal structures, high bandgap of perovskite and complete optical model for current balancing and performance optimization.

I would also like to continue in the study of SiNW growth, as nanowire based solar cells are getting increasing attention of communities focused on opto-electronic devices. I would like to apply the model developed for in-situ ellipsometric data on wider range of samples (prepared on different substrates and with various deposition conditions) and to test the repeatability of process under many different fabrication conditions. Another goal is to extend the model to cover a wider spectral range (0.73 - 6.45 eV) of new ellipsometer installed on the reactor. This range allows to distinguish between a-Si:H and crystalline silicon, and to separate deposition trends of these two materials. In addition to the NW density acquired in this thesis, getting more detailed structural information is expected. As low fabrication cost nanowires are random in their nature, it is paramount to developed reliable in-situ characterization techniques which could be eventually used by industry for an accurate growth control. Moreover, development of more accurate optical models is necessary to optimize radial tandem devices based on random NW arrays to further increase the performance of radial junction based solar cells.

In addition, a transfer of the know-how on the in-situ characterization of nanostructured devices within a scientific collaboration and exchanges is possible to share the acquired knowledge with other groups focusing on nanostructured devices.

A Determination of optical functions of materials for pyramidal textured samples

Outline

Optical functions of materials used on the front side of silicon heterojunction solar cell (see Fig. 5.18) have been determined by ellipsometric measurements of reference samples. The materials of interest are: intrinsic hydrogenated amorphous silicon [(i)a-Si:H], intrinsic hydrogenated amorphous silicon carbide [(i)a-SiC:H], p-type hydrogenated amorphous silicon with lower and higher doping levels [(p)a-Si:H and (p++)a-Si:H, respectively], and indium tin oxide (ITO). Thin films of these materials were separately deposited on 1 mm thick Corning glass substrates using conditions described in Table 2.1 to create reference samples. Corning glass was used to provide sufficient contrast between optical functions of layers and the substrate. Some materials were deposited also on different substrates to evaluate the impact of substrate on their properties. In such cases, more information is provided in sections relevant for these material.

Ellipsometric measurements were performed using a Uvisel 2 (Horiba scientific) at the angle of incidence of 70° and in a wide spectral range $0.6 - 5.4$ eV. The spectral increment varied based on precision needed for different types of samples and the value used for each sample measurement is mentioned in corresponding section. Optical models designed for each sample were fitted to experimental data using the Levenberg-Marquardt least-square minimization algorithm implemented in the DeltaPsi2 software (Horiba Scientific). The fitting error function χ^2 defined by (5.6) in Section 5.3.2 was used as a criterion for the least square algorithm.

Intrinsic hydrogenated amorphous silicon (i)a-Si:H

A reference sample for characterization of an intrinsic a-Si:H consisted of a (i)a-Si:H layer of the nominal thickness of 50 nm deposited by standard conditions (see Table 2.1) on a 1mm thick Corning glass. It was measured in the spectral range $0.6 - 5.4$ eV with an increment of 0.01 eV.

Figure A.1 shows a multi-layer optical model used for modeling of ellispometric data. The model consists of the 1 mm thick Corning glass substrate, the (i)a-Si:H layer of thickness $L2$ and a layer of a surface native oxide SiO_2 of thickness $L3$. The optical function of (i)a-Si:H was modeled using the Tauc-Lorentz model described by Eqs. (4.86) and (4.87) in Section 4.3.3. Parameters of this model were used as free fitting parameters together with the thicknesses $L2$ and $L3$.

Figure A.2 shows excellent agreement between measured (symbols) and modeled (lines) values of I_S and I_C. Measured data are for better visibility drawn with an increment of 0.05 eV instead of that of 0.01 eV used for measurement. Fit results are listed in Table A.1. Obtained optical function of (i)a-Si:H is shown in Fig. A.3, together with optical functions of other silicon based materials to enable better comparison.

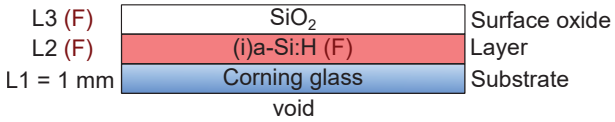

Figure A.1 – Multi-layer optical model for determination of the optical function of (i)a-Si:H. Model consists of the 1 mm Corning glass substrate ($L1 = 1$ mm), the (i)a-Si:H layer ($L2$), and a surface native SiO_2 layer ($L3$). Red symbols F mark the free fitting parameters which are the thicknesses of layers $L2$ and $L3$, and the optical function of (i)a-Si:H.

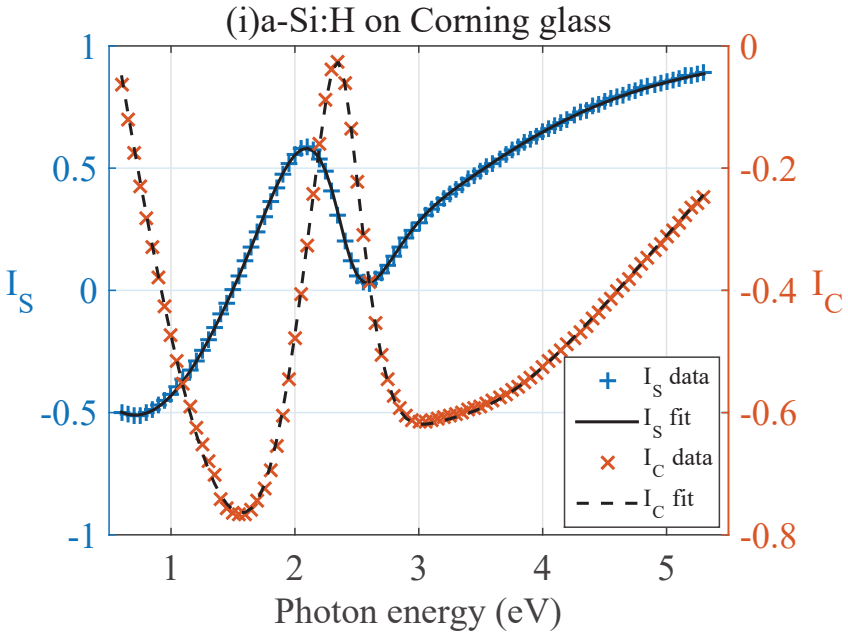

Figure A.2 – Ellipsometric values I_S (blue) and I_C (orange) obtained from model (lines) and measurement (symbols) of the reference sample of (i)a-Si:H on Corning glass at AOI of 70°.

Intrinsic hydrogenated amorphous silicon carbide (i)a-SiC:H

Two reference samples were used for determination of the optical function of intrinsic hydrogenated amorphous silicon carbide [(i)a-SiC:H]. First sample consisted of an (i)a-SiC:H layer of the nominal thickness of 100 nm deposited on the 1 mm thick Corning glass. The second sample consisted of an (i)a-SiC:H layer of the nominal thickness of 50 nm deposited on (100) oriented flat crystalline silicon wafer. Deposition conditions are listed in Table 2.1.

First, each sample was analyzed independently and resulting optical functions were compared to evaluate possible impact of different substrates on de-

Material	Substarte	$L2$ (nm)	$L3$ (nm)	ε_∞ (-)	A (eV)	C (eV)	$E_{L,0}$ (eV)	E_g (eV)	χ^2 (-)
(i)a-Si:H	Corning glass	54.2	2.3	0.5	205	2.20	3.60	1.65	0.18
(i)a-SiC:H	Corning glass	93.4	2.7	1.0	193	2.51	3.65	1.86	0.14
	wafer	45.9	1.9	1.1	195	2.58	3.59	1.87	0.10
	multi-model	93.7 46.1	2.6 2.2	1.0	194	2.54	3.64	1.87	0.24
(p)a-Si:H	Corning glass	143.8	2.6	0.7	190	2.15	3.67	1.66	0.91
(p++)a-Si:H	Corning glass	564.3	3.2	1.1	172	2.25	3.77	1.66	2.02

Table A.1 – Best fit parameters for silicon based materials. Type of a substrate for each reference sample is indicated. Thicknesses $L2$ and $L3$ of material layer and surface oxide, respectively are listed together with the fitting error function χ^2 and parameters of Tauc-Lorentz model used for description of optical function of each material. The parameters of the Tauc-Lorentz model are: the high-frequency dielectric constant ε_∞, the amplitude A_L, position $E_{L,0}$ and broadening C of the peak, and the Tauc energy band gap E_g.

posited material. Both samples were measured by spectroscopic ellipsometer Uvisel 2 in the spectral range $0.6 - 5.4$ eV. First sample was measured with a spectral increment of 0.01 eV, the second sample with an increment of 0.025 eV.

Figure A.4 shows models used for analysis of measured ellipsometric data. Model $M1$ used for the first sample consists of the 1 mm thick Corning glass substrate, an (i)a-SiC:H layer of thickness $L2$ and a surface oxide of thickness $L3$. Model $M2$ used for the second sample is similar to model $M1$ but the substrate is a $300\,\mu$m thick c-Si wafer. The optical function of c-Si was obtained from Ref. 79. Fit results for both samples are listed in Table A.1 and obtained optical functions are shown in Fig. A.5.

One can see that obtained optical functions differ only slightly (see blue and gray lines in Fig. A.5) as well as fitted parameters of Tauc-Lorentz model. Both models agree well to the experimental data as indicated by low values of χ^2 in Table A.1.

Unfortunately, reference sample of (i)a-SiC:H on (111) c-Si wafer was not available to allow a precise determination of the optical function of material corresponding to that deposited on pyramidal facets. However, due to very slight differences between optical functions of materials deposited on the Corning glass and on the wafer, we don't assume big material changes caused by deposition on different substrates. Therefore, we decided to establish only one (i)a-SiC:H optical function which would correspond best to both reference samples at the same time. We modeled both samples together by multi-model consisting of models

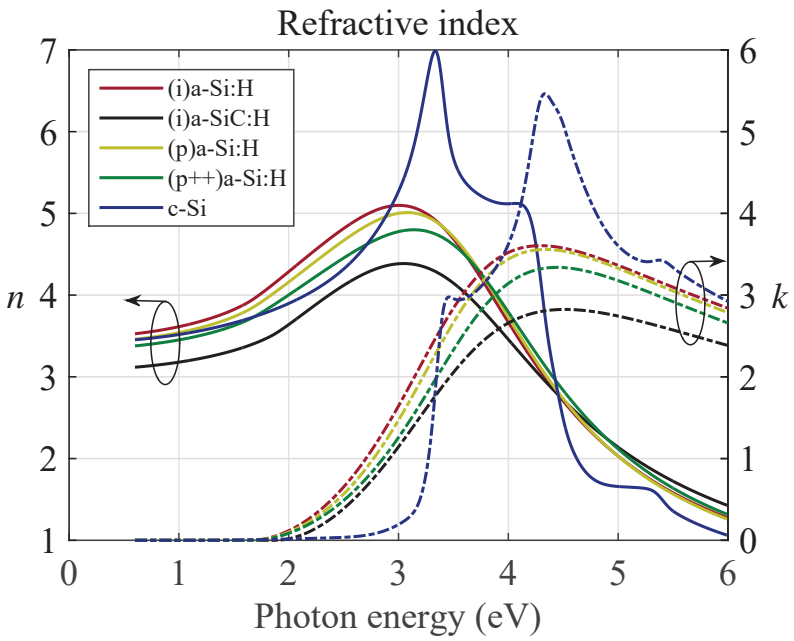

Figure A.3 – Comparison of real (solid lines) and imaginary (dashed-dotted lines) parts n and k of refractive index of intrinsic hydrogenated amorphous silicon [(i)a-Si:H], intrinsic hydrogenated amorphous silicon carbide [(i)a-SiC:H], p-type hydrogenated amorphous silicon with lower and higher doping level [(p)a-Si:H and (p++)a-Si:H, respectively], and crystalline silicon (c-Si) obtained from Ref. 79.

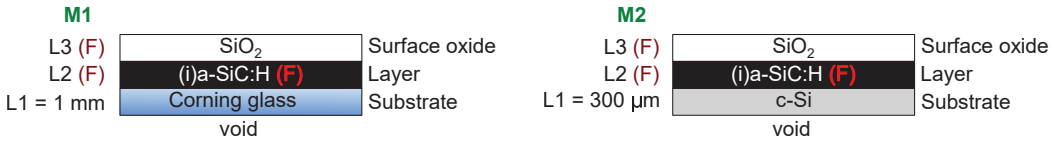

Figure A.4 – Multi-layer optical models $M1$ and $M2$ for determination of the optical function of (i)a-SiC:H. Model $M1$ consists of the Corning glass substrate ($L1 = 1$ mm), the (i)a-SiC:H layer ($L2$), and a surface native SiO_2 layer ($L3$). Model $M2$ includes a c-Si substrate ($L1 = 300\,\mu$m). Red symbols F mark the free fitting parameters which are the thicknesses of layers $L2$ and $L3$, and the optical function of (i)a-SiC:H.

$M1$ and $M2$ with the same optical function of (i)a-SiC:H. The parameters of Tauc-Lorentz model were bound between models $M1$ and $M2$ resulting in one optical function of (i)a-SiC:H best fitted to both reference samples at once. Fit results are listed in Table A.1 and obtained optical function is shown in Fig. A.5 by black lines.

There is a very good agreement between values of I_S and I_C obtained from

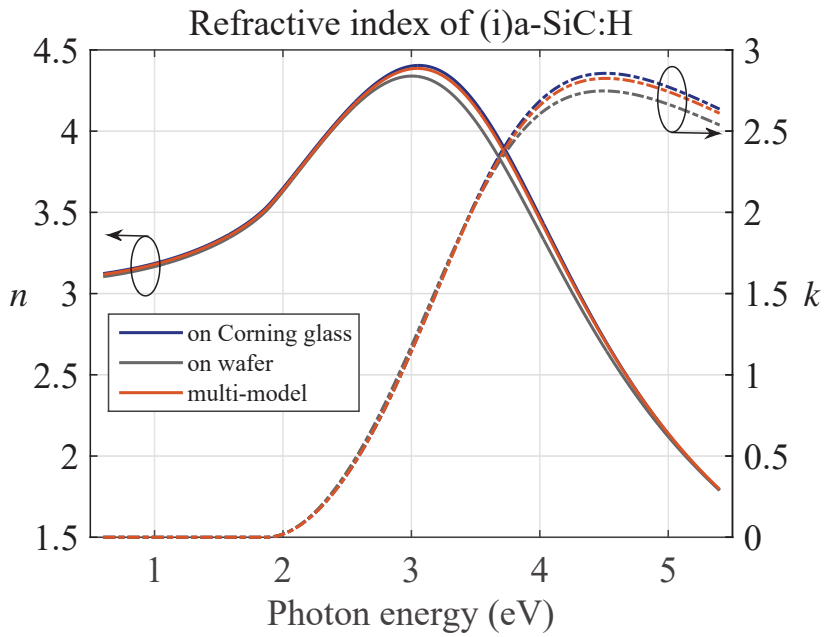

Figure A.5 – Comparison of real (solid lines) and imaginary (dashed-dotted lines) parts n and k of refractive index of hydrogenated amorphous silicon carbide [(i)a-SiC:H] obtained from model $M1$ of reference sample on Corning glass (blue lines), from model $M2$ of reference sample on wafer (gray lines), and from bound multi-model (orange lines).

multi-model (lines) and measurement (symbols) as shown in Fig. A.6 as well as by low value of χ^2 shown in Table A.1. Measured data are for better visibility displayed with an increment of 0.05 eV instead of the measured one 0.01 eV. The optical function determined from the bound multi-model is considered to represent best the average (i)a-SiC:H material and it is used for calculations and modeling of (i)a-SiC:H films on pyramids in Section 5.3. To compare this final function with that of (i)a-Si:H, see Fig. A.3.

P-type hydrogenated amorphous silicon (p)a-Si:H and (p++)a-Si:H

Layers of p-type a-Si:H with lower and higher doping levels [(p)a-Si:H and (p++)a-Si:H, respectively] were deposited using conditions presented in Table 2.1 on the 1 mm thick Corning glass. The nominal thickness of the (p)a-Si:H layer was 150 nm and that of the (p++)a-Si:H was 570 nm. The ellipsometric measurements of both samples were performed with a spectral increment of 0.01 eV.

Figures A.7 and A.8 show multi-layer optical models for analysis of ellipsometric data measured on samples described above. Each model consist of the

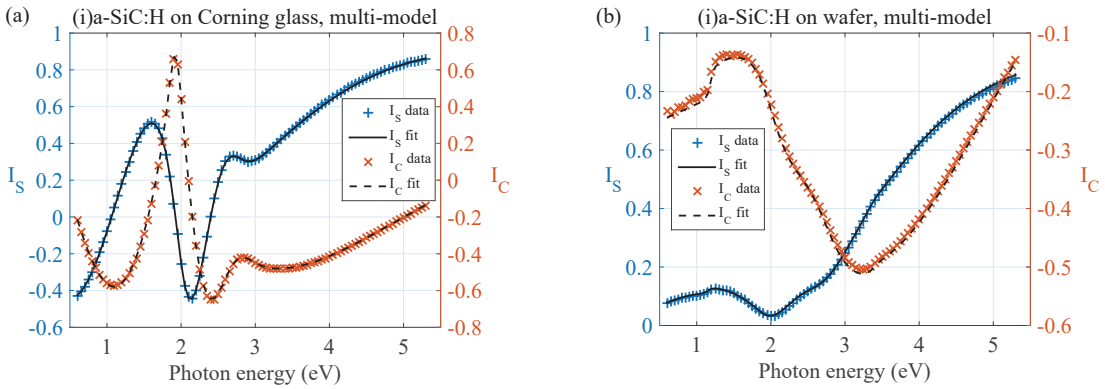

Figure A.6 – Ellipsometric values I_S (blue) and I_C (orange) obtained from bound multi-model (lines) and measurement (symbols) of the reference samples of (i)a-SiC:H on (a) Corning glass and (b) wafer at AOI of 70°.

1 mm thick Corning glass substrate, L_2 layer of analyzed material, and a layer $L3$ representing a surface roughness modeled by Bruggeman effective medium approximation consisting of 50 % of analyzed material and 50 % of void. The optical functions of (p)a-Si:H and (p++)a-Si:H were modeled by Tauc-Lorentz models. The free fitting parameters were the parameters of the Tauc-Lorentz model and thicknesses of the layers $L2$ and $L3$ for each model.

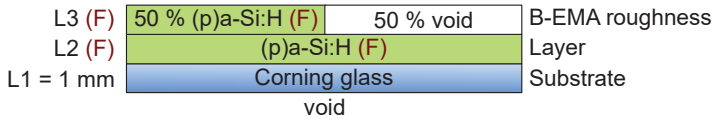

Figure A.7 – Multi-layer optical model for determination of the optical function of (p)a-Si:H. Model consists of the 1 mm Corning glass substrate ($L1 = 1$ mm), the (p)a-Si:H layer ($L2$), and surface roughness layer ($L3$) modeled by B-EMA including (p)a-Si:H and void. Red symbols F mark the free fitting parameters which are the thicknesses of layers $L2$ and $L3$, and the optical function of (p)a-Si:H.

Figure A.9 shows a very good agreement between measured (symbols) and modeled (lines) values of I_S and I_C for both samples. Fit results are listed in Table A.1 and obtained optical functions of (p)a-Si:H and (p++)a-Si:H are shown in Fig. A.3 by light and dark green lines, respectively.

Indium tin oxide ITO

There was one reference sample of ITO deposited on Corning glass and two test samples of ITO deposited on pyramidal wafers of type A1 and B1. The ITO

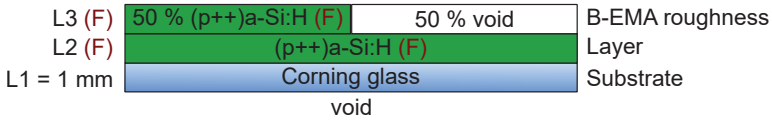

Figure A.8 – Multi-layer optical model for determination of the optical function of (p++)a-Si:H. Model consists of the 1 mm Corning glass substrate ($L1 = 1$ mm), the (p++)a-Si:H layer ($L2$), and a surface roughness layer ($L3$) modeled by B-EMA including (p++)a-Si:H and void. Red symbols F mark the free fitting parameters which are the thicknesses of layers $L2$ and $L3$, and the optical function of (p++)a-Si:H.

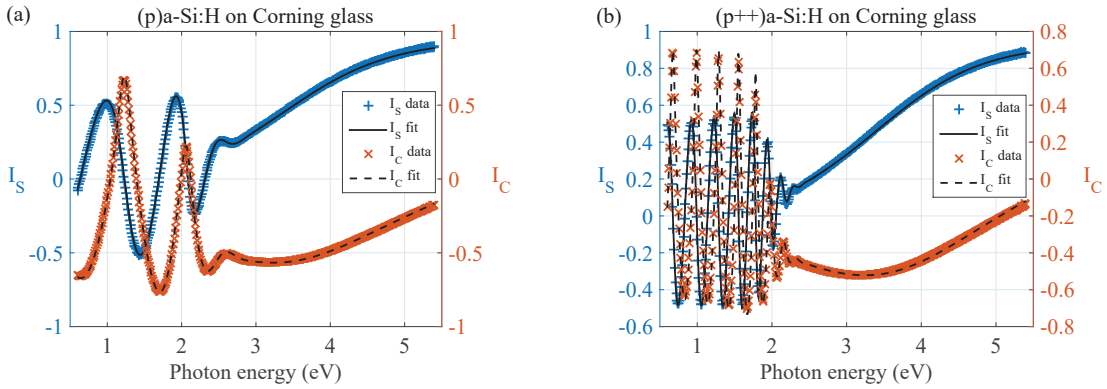

Figure A.9 – Ellipsometric values I_S (blue) and I_C (orange) obtained from model (lines) and measurement (symbols) of the reference samples of (a) (p)a-Si:H and (b) (p++)a-Si:H on Corning glass at AOI of 70°.

was deposited by 2 min sputtering at 200 W and 180 °C resulting in a layer of nominal thickness of 80 - 90 nm on flat substrate. The reference sample was used to determine the ITO optical function and the test samples were used to evaluate possible changes of material properties caused by textured substrates. The sample on Corning glass substrate was measured with a spectral increment of 0.025 eV. Samples on textured substrates were measured in the limited range 1.5 - 5.4 eV with an increment of 0.023 eV using the lateral measurement geometry of inclined sample as described in section 3.2.1 at $AOI = 55°$.

First, optical model $M1$ shown in Fig. A.10 was used for analysis of ellipsometric data measured on the reference sample. This model consists of the 1 mm Corning glass substrate, the ITO layer of thickness $L2$, and a surface roughness layer of thickness $L3$ modeled by B-EMA composed of 50 % of ITO and 50 % of void. The optical function of ITO was modeled using Tauc-Lorentz model (4.86) and (4.87) combined with Drude term (4.84). Parameters describing the optical function together with thicknesses of layers $L2$ and $L3$ were free fitting parame-

ters.

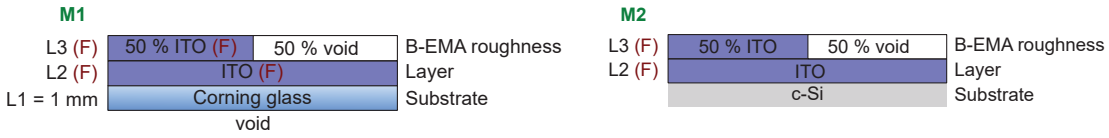

Figure A.10 – Multi-layer optical models $M1$ and $M2$ for determination of the optical function of ITO. Model $M1$ consists of the Corning glass substrate ($L1 = 1$ mm), the ITO layer ($L2$), and a surface roughness layer ($L3$) modeled by B-EMA including ITO and void. Model $M2$ includes a pyramidal wafer substrate modeled as a half-space c-Si. Red symbols F mark the free fitting parameters which are the thicknesses of layers $L2$ and $L3$, and the optical function of ITO.

Figure A.11(a) shows a very good agreement between modeled (lines) and measured (symbols) values of I_S and I_C with a fitting error function as low as $\chi^2 = 0.63$. Obtained optical function is shown in Fig. A.11(b) and is determined by the following parameters of the Tauc-Lorentz and Drude model: $\varepsilon_\infty = 3.0$, $A_L = 102$ eV, $C = 5.89$ eV, $E_{L,0} = 4.11$ eV, $E_g = 2.81$ eV, $E_p = 1.31$ eV and $\Gamma_D = 0.10$ eV, where ε_∞ is the high-frequency dielectric constant, A_L, $E_{L,0}$, C are the amplitude, position and broadening of peak in Tauc-Lorentz model, E_g is the Tauc gap, E_p is the plasma angular frequency and Γ_D is the collision frequency of free carriers in Drude model. The best fitted thicknesses of model layers are $L2 = 70.7$ nm and $L3 = 2.8$ nm.

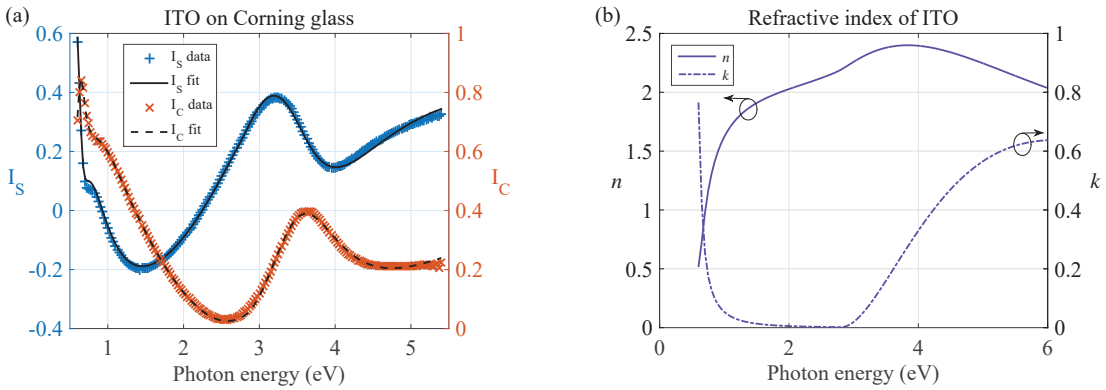

Figure A.11 – (a) Ellipsometric values I_S (blue) and I_C (orange) obtained from model (lines) and measurement (symbols) of the reference sample of ITO on the Corning glass at AOI of 70°. (b) Real (solid line) and imaginary (dashed-dotted line) parts n and k of refractive index of ITO obtained from model $M1$.

Obtained optical function of ITO [see Fig. A.11(b)] was used to model also ITO layers deposited on pyramidal wafers. Optical model $M2$ in Fig. A.10 was used to

analyze ellispometric data measured on test samples with pyramidal substrates of types A1 and B1. The model consists of a c-Si substrate covered by the ITO layer $L2$ and a surface roughness layer $L3$ described by B-EMA consisting of 50 % of ITO and 50 % of void. The substrate can be modeled as a half-space in case of inclined pyramids as demonstrated in Section 5.3.2. The optical function of c-Si was obtained from Ref. 79. The fitting parameters in this case are the thicknesses of layers $L2$ and $L3$.

Figure A.12 shows a good agreement between modeled (lines) and measured (symbols) values I_S and I_C for ITO deposited on pyramidal wafers of type A1 and B1. Fit results for substrate of type A1 are $L2 = 75.5$ nm, $L3 = 1.9$ nm and $\chi^2 = 2.17$. Fit results for substrate of type B1 are $L2 = 76.5$ nm, $L3 = 3.0$ nm and $\chi^2 = 32.53$. Substrate B1 contains smaller pyramids with not so smooth facets as substrate A1 [compare Fig. 2.2(A1) and Fig. 2.2(B1)]. This makes ellipsometric measurements on B1 substrate more difficult and results in higher noise (especially near the boundaries of measured spectral range) than in case of A1 substrate. Despite the high value of χ^2 increased by the higher noise for B1 substrate, the agreement between model and measurement is still very good as can be seen in Fig. A.11(b). Excluding the noise at the boundaries of the measurement region by limiting the spectral range to $1.75 - 5.1$ eV leads to decrease of the χ^2 value to 3.86, while the fit results stay preserved.

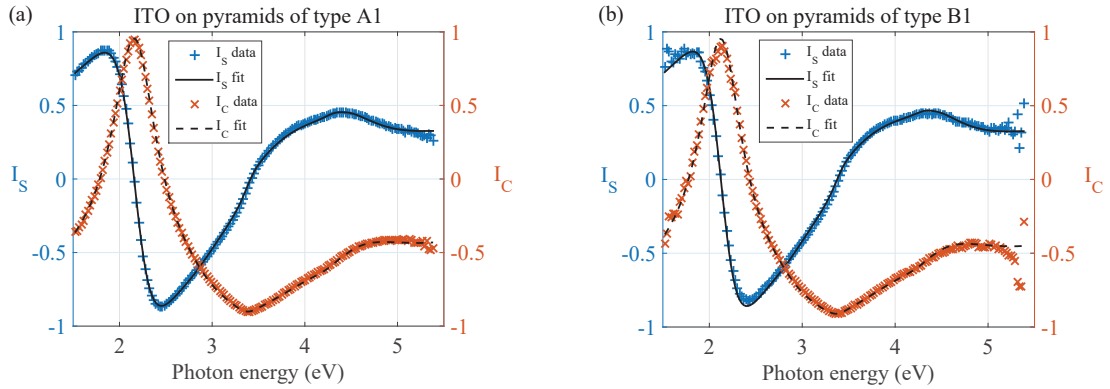

Figure A.12 – Ellipsometric values I_S (blue) and I_C (orange) obtained from model (lines) and measurement (symbols) of the reference sample of ITO on pyramidal wafer of type (a) A1 and (b) B1 at AOI of $55°$.

The performed analysis of test samples confirms that optical function of ITO shown in Fig. A.11(b) is suitable to describe material deposited on pyramidal wafers of both types A1 and B1.

List of Figures

List of Tables

List of publications

Peer-reviewed journals

Z. Mrazkova, I. P. Sobkowicz, M. Foldyna, K. Postava, I. Florea, J. Pištora, and P. Roca i Cabarrocas, "Optical properties and performance of pyramidal texture silicon heterojunction solar cells: key role of vertex angles", Prog. Photovolt. Res. Appl., submitted (2017).

Z. Mrazkova, M. Foldyna, S. Misra, M. Al-Ghzaiwat, K. Postava, J. Pištora, and P. Roca i Cabarrocas, "In-situ Mueller matrix ellipsometry of silicon nanowires grown by plasma enhanced vapor-liquid-solid method for radial junction solar cells", Appl. Surf. Sci., in press (2016) doi: 10.1016/j.apsusc.2016.12.199.

T. Kohut, K. Postava, **Z. Mrazkova**, M. Foldyna, P. Roca i Cabarrocas, M. Mičica, and J. Pištora, "Modeling of Mueller matrix response from diffracting structures", J. Nanosci. Nanotechnol., **16**, 7805–7809 (2016).

Z. Mrazkova, A. Torres-Rios, R. Ruggeri, M. Foldyna, K. Postava, J. Pištora, and P. Roca i Cabarrocas, "In-situ spectroscopic ellipsometry of microcrystalline silicon deposited by plasma-enhanced chemical vapor deposition on flexible Fe-Ni alloy substrate for photovoltaic applications", Thin Solid Films, **571**, 749–755 (2014).

Conference proceedings

T. A. Germer, M. Foldyna, **Z. Mrazkova**, G. Fischer, and E. Drahi, "Mueller matrix bidirectional reflectance distribution function measurements and modeling of textured silicon surfaces", SPIE Optical Engineering+ Applications, International Society for Optics and Photonics, 996107–996107 (2016).

Z. Mrázková, K Postava, A. Torres-Rios, M. Foldyna, P. Roca i Cabarrocas, and J. Pištora, "Optical Modeling of Microcrystalline Silicon Deposited by Plasma-Enhanced Chemical Vapor Deposition on Low-Cost Iron-Nickel Substrates for Photovoltaic Applications", Procedia Materials Science, **12**, 130–135 (2016).

Z. Mrazkova, K Postava, A. Torres-Rios, M. Foldyna, P. Roca i Cabarrocas, V. Vodárek, J. Holešinský, I. Vávra, and J. Pištora, "Crystalline composition of silicon deposited on a low-cost substrate for photovoltaic applications studied by in-situ spectroscopic ellipsometry", Proc. SPIE, **9441**, (2014).

Z. Mrazkova, D. Hrabovsky, K. Postava, and J. Pištora, "Application of infrared ATR ellipsometry for measurement of solid samples: Calibration procedure", Proc. SPIE, **8306**, Photonics, Devices, and Systems V, 83060S (2011).

Z. Mrázková, D. Hrabovský, K Postava, J. Pištora, S. Turczynski, K. Kolodziejak, and D. A. Pawlak, "Far-infrared spectroscopy of terbium-scandium-aluminium garnet and terbium-scandium perovskite", Proc. SPIE **7746**, 17th Slovak-Czech-Polish Optical Conference on Wave and Quantum Aspects of Contemporary Optics, 774617 (2010).

Conference contributions

Z. Mrazkova, M. Foldyna, S. Misra, K. Postava, M. Al-Ghzaiwat, J. Pištora, and P. Roca i Cabarrocas, "Tracing the growth of random silicon nanowires for radial junction solar cells using in-situ ellipsometric techniques", NanoOstrava 2017: 5th Nanomaterials and nanotechnology Meeting, Ostrava, Czech Republic, 22-25 May 2017. *Oral presentation*.

Z. Mrazkova, M. Foldyna, S. Misra, M. Al-Ghzaiwat, K. Postava, J. Pištora, and P. Roca i Cabarrocas, "In-situ Mueller matrix ellipsometry of silicon nanowires grown by plasma enhanced vapor-liquid-solid method for radial junction solar cells", 7th International Conference on Spectroscopic Ellipsometry (ICSE-7), Berlin, Germany, 6-10 June 2016. *Oral presentation*.

Z. Mrazkova, M. Foldyna, S. Misra, K. Postava, J. Pištora, and P. Roca i Cabarrocas, "Polarimetric study of plasma-assisted vapor-liquid-solid grown nanowires on various substrates", Photovoltaic Technical Conference 2016: From advanced materials and processes to innovative applications (PVTC 2016), Marseille, France, 9-11 May 2016. *Oral presentation*.

Z. Mrazkova, I. P. Sobkowicz, I. Florea, M. Foldyna, K. Postava, J. Pištora, and P. Roca i Cabarrocas, "How the etching solution affects the geometry and optical performance of pyramidal texture for solar cell", Journées Nationales du Photo-Voltaïque (JNPV 2015), Dourdan, France, 1-4 December 2015. *Poster presentation*.

Z. Mrazkova, I. P. Sobkowicz, I. Florea, M. Foldyna, K. Postava, J. Pištora, and P. Roca i Cabarrocas, "Optical characterization of thin films deposited on crystalline silicon pyramids for high performance HIT solar cells", European Materials Research Society (E-MRS) Spring Meeting, Lille, France, 11-15 May 2015, Symposium C: Advanced inorganic materials and structures for photovoltaics C-29, P3 33. *Poster presentation*.

Z. Mrazkova, I.P. Sobkowicz, M. Foldyna, I. Florea, K. Postava, V. Mareš, J. Piš-

tora, and P. Roca i Cabarrocas, "Optical properties of random pyramidal textures on silicon wafers: comparison between different fabricated pyramids", Photovoltaic Technical Conference: from Advanced Materials and Processes to Innovative Applications (PVTC 2015), Aix-en-Provence, France, 27-29 May 2015. *Oral presentation*.

Z. Mrazkova, M. Foldyna, K. Postava, A. Torres-Rios, I.P. Sobkowicz, P. Roca i Cabarrocas, "Modeling and characterization of materials and nanostructures for photovoltaic applications", Journées Nationales du PhotoVoltaïque 2014 (JNPV 2014), Dourdan, France, 2-5 December 2014. *Poster presentation*.

Z. Mrazkova, "Modeling and characterization of materials and nanostructures for photovoltaic applications", 6ème Congrès du LPICM, École Polytechnique, Forges-les-Eaux, France, 1-3 October 2014. *Poster presentation*.

Z. Mrazkova, A. Torres-Rios, M. Foldyna, P. Roca i Cabarrocas, K. Postava, and J. Pištora, "Crystalline composition of silicon deposited on a low-cost substrate for photovoltaic applications studied by in-situ spectroscopic ellipsometry", XIX Polish-Slovak-Czech Optical Conference on Wave and Quantum Aspects of Contemporary Optics 2014 (PSCOC 2014), Wojanow, Poland, 8-12 September 2014. *Oral presentation*.

Z. Mrazkova, K. Postava, A. Torres-Rios, M. Foldyna, P. Roca i Cabarrocas, V. Vodárek, J. Holešinský, and J. Pištora, "Optical modelling of microcrystalline silicon deposited by plasma-enhanced chemical vapour deposition on low-cost iron-nickel substrate for photovoltaic application", New Methods of Damage and Failure Analysis of Structural Parts Workshop, Ostrava, Czech Republic, September 2014. *Oral presentation*.

Z. Mrazkova, A. Torres-Rios, M. Foldyna, P. Roca i Cabarrocas, K. Postava, and J. Pištora, "Study of properties of materials for photovoltaic applications by in-situ and ex-situ optical methods", Czech-Bavarian Workshop on Nanotechnology and Advanced Materials, N´urnberg, Germany, 17-18 March 2014. *Oral presentation*.

Z. Mrazkova, A. Torres-Rios, M. Foldyna, P. Roca i Cabarrocas, K. Postava, and J. Pištora, "In-situ spectroscopic ellipsometry of microcrystalline silicon deposited by PECVD on flexible Fe-Ni alloy substrate for photovoltaic applications", 6th International Conference on Spectroscopic Ellipsometry (ICSE – VI 2013), Kyoto, Japan, 24-31 May 2013. *Poster presentation*.

Z. Mrazkova, D. Hrabovský, K. Postava, and J. Pištora, "Application of infrared ATR ellipsometry for measurement of solid samples: Calibration procedure", Photonics Prague 2011: The 7th International Conference on Photonics, Devices and Systems, Prague, Czech Republic, 24-26 August 2011. *Poster presentation*.

Z. Mrazkova, D. Hrabovský, K. Postava, J. Pištora, D. A. Pawlak, S. Turczynski,

and K. Kolodziejak, "Far infrared spectroscopy of terbium-scandium-aluminium garnet and terbium-scandium perovskite", 17th Slovak-Czech-Polish Optical Conference on Wave and Quantum Aspects of Contemporary Optics, Liptovský Ján, Slovakia, 6-10 September 2010. *Poster presentation*.

Research project participations and acknowledgment of financement

Principal investigator: Student research grants (SGS projects)

— SP2017/99: Development of optical models for tracing of deposition processes during solar cell fabrication (2017)

— SP2016/79: In-situ optical characterization of materials for solar cells (2016)

— SP2015/72: Study of pyramidal textured silicon wafers for solar cells applications (2015)

— SP2014/86: Optical modeling and characterization of silicon nanostructures for photovoltaic applications (2014)

European project: granted by the European Union

— PhotonVoltaics (Framework Programme 7, 309127), Nanophotonics for ultrathin crystalline silicon photovoltaics

ANR projects: granted by the French National Grant Agency

— INDEED (ANR-15-CE05-0019), Innovative Diffuse transparent Electrodes for solar cells applications

— Solarium (ANR-14-CE05-0025), Radial-junction silicon nanowire solar cells in a low-cost thin film technology

— Platofil (ANR-14-CE26-0020), PLAteforme phoTOnique à base de nanoFILs

GACR projects: granted by the Czech Science Foundation

— 15-21547S: Charakterizace magnetických nanostruktur optickými metodami

— 15-08971S: Nové nelineární a magneto-optické jevy v periodických strukturách

Nanobase: granted by the Ministry of Education, Youth and Sports of the Czech Republic

— CZ.1.07/2.3.00/20.0074: Nanotechnology – the basis for international cooperation

IT4Innovations: granted by the Ministry of Education, Youth and Sports of the Czech Republic

— LM2015070, Research Program 4: Supercomputing for Nanotechnologies

References

[1] BP Statistical Review of World Energy 2015 (BP p.l.c., London, UK, 2015).

[2] BP Statistical Review of World Energy 2017 (BP p.l.c., London, UK, 2017).

[3] D. Gielen, R. Kempener, M. Taylor, F. Boshell, and A. Seleem, Letting in the Light: How solar PV will revolutionise the electricity system (International Renewable Energy Agency (IRENA), Abu Dhabi, 2016).

[4] IRENA, Renewable capacity statistics 2017 (International Renewable Energy Agency (IRENA), Abu Dhabi, 2017).

[5] J. Merrill, D. Wilt, D. Chapman, G. Bradshaw, K. Montgomery, N. Gapp, and B. Carpenter, "Advanced Photovoltaic Power System Development at the US Air Force Research Laboratory," in E3S Web of Conferences, vol. 16, p. 01001 (EDP Sciences, 2017).

[6] ITRPV, International Technology Roadmap for Photovoltaic Results 2016 (ITRPV Eighth Edition 2017, 2017).

[7] NREL, Best Research-Cell Efficiencies (National Renewable Energy Laboratory (NREL), Golden, CO, USA, 2017).

[8] J. Sun, M. F. Saenger, M. Schubert, J. N. Hilfiker, R. Synowicki, C. M. Herzinger, and J. Woollam, "Characterizing antireflection coatings on textured monocrystalline silicon with spectroscopic ellipsometry," in Photovoltaic Specialists Conference (PVSC), 2009 34th IEEE, pp. 001,407–001,411 (IEEE, 2009).

[9] M. Saenger, J. Sun, M. Schädel, J. Hilfiker, M. Schubert, and J. A. Woollam, "Spectroscopic ellipsometry characterization of SiN x antireflection films on textured multicrystalline and monocrystalline silicon solar cells," Thin Solid Films **518**(7), 1830–1834 (2010).

[10] M. Taguchi, A. Yano, S. Tohoda, K. Matsuyama, Y. Nakamura, T. Nishiwaki, K. Fujita, and E. Maruyama, "24.7% record efficiency HIT solar cell on thin silicon wafer," IEEE Journal of Photovoltaics **4**(1), 96–99 (2014).

[11] T. Mishima, M. Taguchi, H. Sakata, and E. Maruyama, "Development status of high-efficiency HIT solar cells," Solar Energy Materials and Solar Cells **95**(1), 18–21 (2011).

[12] K. Masuko, M. Shigematsu, T. Hashiguchi, D. Fujishima, M. Kai, N. Yoshimura, T. Yamaguchi, Y. Ichihashi, T. Mishima, N. Matsubara, et al., "Achievement of more than 25% conversion efficiency with crystalline silicon heterojunction solar cell," IEEE Journal of Photovoltaics **4**(6), 1433–1435 (2014).

[13] K. Yoshikawa, H. Kawasaki, W. Yoshida, T. Irie, K. Konishi, K. Nakano, T. Uto, D. Adachi, M. Kanematsu, H. Uzu, et al., "Silicon heterojunction solar cell with interdigitated back contacts for a photoconversion efficiency over 26%," Nature Energy **2**, 17,032 (2017).

[14] B. M. Kayes, H. A. Atwater, and N. S. Lewis, "Comparison of the device physics principles of planar and radial p-n junction nanorod solar cells," Journal of applied physics **97**(11), 114,302 (2005).

[15] S. Misra, L. Yu, W. Chen, M. Foldyna, and P. Roca i Cabarrocas, "A review on plasma-assisted VLS synthesis of silicon nanowires and radial junction solar cells," Journal of Physics D: Applied Physics **47**(39), 393,001 (2014).

[16] S. Misra, L. Yu, M. Foldyna, and P. Roca i Cabarrocas, "High efficiency and stable hydrogenated amorphous silicon radial junction solar cells built on VLS-grown silicon nanowires," Solar Energy Materials and Solar Cells **118**, 90–95 (2013).

[17] S. Misra, L. Yu, M. Foldyna, and P. Roca i Cabarrocas, "New approaches to improve the performance of thin-film radial junction solar cells built over silicon nanowire arrays," IEEE Journal of Photovoltaics **5**(1), 40–45 (2015).

[18] P. K. Singh, R. Kumar, M. Lal, S. Singh, and B. Das, "Effectiveness of anisotropic etching of silicon in aqueous alkaline solutions," Solar Energy Materials and Solar Cells **70**(1), 103–113 (2001).

[19] E. Vazsonyi, K. De Clercq, R. Einhaus, E. Van Kerschaver, K. Said, J. Poortmans, J. Szlufcik, and J. Nijs, "Improved anisotropic etching process for industrial texturing of silicon solar cells," Solar energy materials and solar cells **57**(2), 179–188 (1999).

[20] D. L. King and M. E. Buck, "Experimental optimization of an anisotropic etching process for random texturization of silicon solar cells," in Photovoltaic Specialists Conference, 1991., Conference Record of the Twenty Second IEEE, pp. 303–308 (IEEE, 1991).

[21] S. C. Baker-Finch and K. R. McIntosh, "Reflection distributions of textured monocrystalline silicon: implications for silicon solar cells," Progress in photovoltaics: Research and Applications **21**(5), 960–971 (2013).

[22] J. Ximello Quiebras, A. Dastgheib-Shirazi, S. Scholz, and G. Hahn, "Influence of pyramid size of chemically textured silicon wafers on the characteristics of industrial solar cells," in 25th European Photovoltaic Solar Energy Conference and Exhibition. 5th World Conference on photovoltaic Energy Conversion, pp. 1761–1764 (2010).

[23] S.-S. Tan, M. Reed, H. Han, and R. Boudreau, "Morphology of etch hillock defects created during anisotropic etching of silicon," Journal of Micromechanics and Microengineering **4**(3), 147 (1994).

[24] Y. Bhatnagar and A. Nathan, "On pyramidal protrusions in anisotropic etching of< 100> silicon," Sensors and Actuators A: Physical **36**(3), 233–240 (1993).

[25] E. Fornies, C. Zaldo, and J. Albella, "Control of random texture of monocrystalline silicon cells by angle-resolved optical reflectance," Solar Energy Materials and Solar Cells **87**(1), 583–593 (2005).

[26] H. Seidel, L. Csepregi, A. Heuberger, and H. Baumgärtel, "Anisotropic etching of crystalline silicon in alkaline solutions I. Orientation dependence and behavior of passivation layers," Journal of the electrochemical society **137**(11), 3612–3626 (1990).

[27] L. M. Landsberger, S. Naseh, M. Kahrizi, and M. Paranjape, "On hillocks generated during anisotropic etching of Si in TMAH," Journal of microelectromechanical systems **5**(2), 106–116 (1996).

[28] J. Thong, P. Luo, W. Choi, and S. Tan, "Evolution of hillocks during silicon etching in TMAH," Journal of Micromechanics and Microengineering **11**(1), 61 (2001).

[29] I. Zubel and M. Kramkowska, "Development of etch hillocks on different Si (hkl) planes in silicon anisotropic etching," Surface Science **602**(9), 1712–1721 (2008).

[30] G. Yun, K. Crabtree, and R. A. Chipman, "Properties of the polarization ray tracing matrix," in Optical Engineering+ Applications, pp. 66,820Z–66,820Z (International Society for Optics and Photonics, 2007).

[31] S. C. Baker-Finch and K. R. McIntosh, "Reflection of normally incident light from silicon solar cells with pyramidal texture," Progress in Photovoltaics: Research and Applications **19**(4), 406–416 (2011).

[32] K. Watanabe, N. Matsuki, and H. Fujiwara, "Ellipsometry characterization of hydrogenated amorphous silicon layers formed on textured crystalline silicon substrates," Applied physics express **3**(11), 116,604 (2010).

[33] N. Matsuki and H. Fujiwara, "Nondestructive characterization of textured a-Si: H/c-Si heterojunction solar cell structures with nanometer-scale a-Si: H and In2O3: Sn layers by spectroscopic ellipsometry," Journal of Applied Physics **114**(4), 043,101 (2013).

[34] S. Kumar, B. Drevillon, and C. Godet, "I nsitu spectroscopic ellipsometry study of the growth of microcrystalline silicon," Journal of applied physics **60**(4), 1542–1544 (1986).

[35] N. Layadi, P. Roca i Cabarrocas, B. Drévillon, and I. Solomon, "Real-time spectroscopic ellipsometry study of the growth of amorphous and microcrystalline silicon thin films prepared by alternating silicon deposition and hydrogen plasma treatment," Physical Review B **52**(7), 5136 (1995).

[36] R. Collins, A. Ferlauto, G. Ferreira, C. Chen, J. Koh, R. Koval, Y. Lee, J. Pearce, and C. Wronski, "Evolution of microstructure and phase in amorphous, protocrystalline, and microcrystalline silicon studied by real time spectroscopic ellipsometry," Solar Energy Materials and Solar Cells **78**(1), 143–180 (2003).

[37] H. Fujiwara and M. Kondo, "Real-time control and characterization of a-Si: H growth in a-Si: H/c-Si heterojunction solar cells by spectroscopic ellipsometry and infrared spectroscopy," in Photovoltaic Specialists Conference, 2005. Conference Record of the Thirty-first IEEE, pp. 1285–1288 (IEEE, 2005).

[38] Z. Mrázková, A. Torres-Rios, R. Ruggeri, M. Foldyna, K. Postava, J. Pištora, and P. Roca i Cabarrocas, "In-situ spectroscopic ellipsometry of microcrystalline silicon deposited by plasma-enhanced chemical vapor deposition on flexible Fe–Ni alloy substrate for photovoltaic applications," Thin Solid Films **571**, 749–755 (2014).

[39] L. Yu, B. O'Donnell, P.-J. Alet, and P. Roca i Cabarrocas, "All-in-situ fabrication and characterization of silicon nanowires on TCO/glass substrates for photovoltaic application," Solar Energy Materials and Solar Cells **94**(11), 1855–1859 (2010).

[40] S. Sivaram, Chemical Vapor Deposition: Thermal and Plasma Deposition of Electronic Materials (Springer US, 2013).

[41] H. Nalwa, Handbook of Nanostructured Materials and Nanotechnology (Academic Press, 1999).

[42] A. Torres-Rios, Y. Djeridane, M. Nath, P. Reydet, J. Reyal, and P. Roca i Cabarrocas, "Epitaxial growth of crystalline silicon on N42 alloys by PECVD at 175 C for low cost and high efficiency solar cells," Proceeding 27th EU PVSEC (2011).

[43] I. P. Sobkowicz, "Study and optimization of the growth of a-Si: H on wet-chemically textured c-Si substrates for the enhancement of a-Si: H/c-Si heterojunction solar cells," Ph.D. thesis, Ecole Doctorale Polytechnique (2014).

[44] I. P. Sobkowicz, "Solar cell and method of manufacturing thereof," (2016). WO Patent App. PCT/EP2015/076,835.

[45] H. Seidel, L. Csepregi, A. Heuberger, and H. Baumgärtel, "Anisotropic etching of crystalline silicon in alkaline solutions I. Orientation dependence and behavior of passivation layers," Journal of the electrochemical society **137**(11), 3612–3626 (1990).

[46] J. Červenka, M. Ledinskỳ, J. Stuchlík, H. Stuchlíková, S. Bakardjieva, K. Hruška, A. Fejfar, and J. Kočka, "The structure and growth mechanism of Si nanoneedles prepared by plasma-enhanced chemical vapor deposition," Nanotechnology **21**(41), 415,604 (2010).

[47] X. Xie, X. Zeng, P. Yang, C. Wang, and Q. Wang, "In situ formation of indium catalysts to synthesize crystalline silicon nanowires on flexible stainless steel substrates by PECVD," Journal of Crystal Growth **347**(1), 7–10 (2012).

[48] M. K. Sunkara, S. Sharma, R. Miranda, G. Lian, and E. Dickey, "Bulk synthesis of silicon nanowires using a low-temperature vapor–liquid–solid method," Applied Physics Letters **79**(10), 1546–1548 (2001).

[49] S. Misra, "Single and tandem radial junction silicon thin film solar cells based on PECVD grown crystalline silicon nanowire arrays," Ph.D. thesis, Ecole Doctorale Polytechnique (2015).

[50] V. Schmidt, J. V. Wittemann, S. Senz, and U. Gösele, "Silicon nanowires: a review on aspects of their growth and their electrical properties," Advanced Materials **21**(25-26), 2681–2702 (2009).

[51] O. Gunawan and S. Guha, "Characteristics of vapor–liquid–solid grown silicon nanowire solar cells," Solar Energy Materials and Solar Cells **93**(8), 1388–1393 (2009).

[52] W. Shockley and W. Read Jr, "Statistics of the recombinations of holes and electrons," Physical review **87**(5), 835 (1952).

[53] B. Drevillon and A. De Martino, "Liquid crystal based polarimetric system, a process for the calibration of this polarimetric system, and a polarimetric measurement process," (2007). US Patent 7196792.

[54] E. Compain, S. Poirier, and B. Drevillon, "General and self-consistent method for the calibration of polarization modulators, polarimeters, and Mueller-matrix ellipsometers," Applied optics **38**(16), 3490–3502 (1999).

[55] S. Ben Hatit, M. Foldyna, A. De Martino, and B. Drévillon, "Angle-resolved Mueller polarimeter using a microscope objective," physica status solidi (a) **205**(4), 743–747 (2008).

[56] B. E. Saleh, M. C. Teich, and B. E. Saleh, Fundamentals of photonics, vol. 22 (Wiley New York, 1991).

[57] M. Born and E. Wolf, Principles of Optics, 5th ed. (Pergamon, Oxford, 1975).

[58] P. Yeh, "Optics of anisotropic layered media: A new 4×4 matrix algebra," Surf. Sci. **96**, 41–53 (1980).

[59] P. Yeh, "Electromagnetic propagation in birefringent layered media," J. Opt. Soc. Am. **69**, 742–755 (1979).

[60] H. Fujiwara, Spectroscopic ellipsometry: principles and applications (John Wiley & Sons, 2007).

[61] E. Garcia-Caurel, A. De Martino, J.-P. Gaston, and L. Yan, "Application of spectroscopic ellipsometry and Mueller ellipsometry to optical characterization," Applied spectroscopy **67**(1), 1–21 (2013).

[62] H. Tompkins and E. A. Irene, Handbook of ellipsometry (William Andrew, 2005).

[63] R. M. A. Azzam and N. M. Bashara, Ellipsometry and Polarized Light, 2nd ed. (North-Holland, Amsterdam, 1987).

[64] K. Kim, L. Mandel, and E. Wolf, "Relationship between Jones and Mueller matrices for random media," JOSA A **4**(3), 433–437 (1987).

[65] G. E. Jellison Jr. and F. A. Modine, "Parameterization of the functions of amorphous materials in the interband region," Appl. Phys. Lett. **69**(3), 371–373 (1996).

[66] G. E. J. Jr. and F. A. Modine, "Erratum: Parameterization of the optical functions of amorphous materials in the interband region [Appl. Phys. Lett. 69, 371 (1996)]," Applied Physics Letters **69**(14), 2137–2137 (1996).

[67] R. Collins, J. Koh, H. Fujiwara, P. Rovira, A. Ferlauto, J. Zapien, C. Wronski, and R. Messier, "Recent progress in thin film growth analysis by multichannel spectroscopic ellipsometry," Applied surface science **154**, 217–228 (2000).

[68] P. Rovira and R. Collins, "Analysis of specular and textured SnO 2: F films by high speed four-parameter Stokes vector spectroscopy," Journal of applied physics **85**(4), 2015–2025 (1999).

[69] H. Fujiwara and M. Kondo, "Effects of carrier concentration on the dielectric function of ZnO: Ga and In 2 O 3: Sn studied by spectroscopic ellipsometry: analysis of free-carrier and band-edge absorption," Physical Review B **71**(7), 075,109 (2005).

[70] J. Tauc, R. Grigorovici, and A. Vancu, "Optical properties and electronic structure of amorphous germanium," physica status solidi (b) **15**(2), 627–637 (1966).

[71] A. Sihvola, Electromagnetic Mixing Formulas and Applications, IEE Publication Series (Institution of Engineering and Technology (IET), 2000).

[72] D. Aspnes, J. Theeten, and F. Hottier, "Investigation of effective-medium models of microscopic surface roughness by spectroscopic ellipsometry," Physical Review B **20**(8), 3292 (1979).

[73] D. E. Aspnes, "Local-field effects and effective-medium theory: A microscopic perspective," American Journal of Physics **50**(8), 704–709 (1982). URL `http://dx.doi.org/10.1119/1.12734`.

[74] D. Franta and I. Ohlídal, "Comparison of effective medium approximation and Rayleigh–Rice theory concerning ellipsometric characterization of rough surfaces," Optics communications **248**(4), 459–467 (2005).

[75] E. D. Palik, ed., Handbook of Optical Constants of Solids I, II, III (Academic Press, 1991).

[76] S. Olibet, C. Monachon, A. Hessler-Wyser, E. Vallat-Sauvain, L. Fesquet, J. Damon-Lacoste, S. De-Wolf, and C. Ballif, "Textured silicon heterojunction solar cells with over 700mV open-circuit voltage studied by transmission electron microscopy," in 23 EUPVSEC, PV-LAB-CONF-2010-032 (2008).

[77] S. Olibet, E. Vallat-Sauvain, L. Fesquet, C. Monachon, A. Hessler-Wyser, J. Damon-Lacoste, S. De Wolf, and C. Ballif, "Properties of interfaces in amorphous/crystalline silicon heterojunctions," physica status solidi (a) **207**(3), 651–656 (2010).

[78] T. Kohut, K. Postava, Z. Mrázková, M. Foldyna, P. Roca i Cabarrocas, M. Mičica, and J. Pištora, "Modeling of Mueller matrix response from diffracting structures," Journal of Nanoscience and Nanotechnology **16**(8), 7805–7809 (2016).

[79] C. Herzinger, B. Johs, W. McGahan, J. Woollam, and W. Paulson, "Ellipsometric determination of optical constants for silicon and thermally grown silicon dioxide via a multi-sample, multi-wavelength, multi-angle investigation," Journal of Applied Physics **83**(6), 3323–3336 (1998).

[80] G. E. Jellison Jr., "Spectroscopic ellipsometry data analysis: measured versus calculated quantities," Thin Solid Films **313-314**, 33–39 (1998).

[81] G. E. Jellison, Jr. and F. A. Modine, "Two-modulator generalized ellipsometery: theory," Appl. Opt. **36**(31), 8190–8189, (1997).

[82] G. E. Jellison, Jr. and F. A. Modine, "Two-modulator generalized ellipsometery: theory – erratum," Appl. Opt. **42**(19), 3765 (2003).

[83] P. Drude, "Zur elektronentheorie der metalle," Annalen der Physik **306**(3), 566–613 (1900).

[84] C. Gueymard, D. Myers, and K. Emery, "Proposed reference irradiance spectra for solar energy systems testing," Solar energy **73**(6), 443–467 (2002).

[85] Z. Mrazkova, I. Sobkowicz, M. Foldyna, K. Postava, I. Florea, J. Pištora, and P. Roca i Cabarrocas, "Influence of pyramidal surface morphology on optimization and optical performance enhancement of silicon heterojunction solar cells," Progress in Photovoltaics: Research and Applications (under review 2017).

[86] J. Tang, J.-L. Maurice, W. Chen, S. Misra, M. Foldyna, E. V. Johnson, and P. Roca i Cabarrocas, "Plasma-Assisted Growth of Silicon Nanowires by Sn Catalyst: Step-by-Step Observation," Nanoscale research letters **11**(1), 455 (2016).

[87] S. Misra, L. Yu, W. Chen, and P. Roca i Cabarrocas, "Wetting layer: the key player in plasma-assisted silicon nanowire growth mediated by tin," The Journal of Physical Chemistry C **117**(34), 17,786–17,790 (2013).

université PARIS-SACLAY
ÉCOLE DOCTORALE
INTERFACES
Approches Interdisciplinaires : Fondements, Applications et Innovation

Titre : Modélisation et caractérisation de matériaux et nanostructures pour les applications photovoltaïques

Mots clés : ellipsométrie spectroscopique, polarimétrie matricielle Mueller in-situ, modèles optiques multi-couches, cellules solaires, textures pyramidales, nanofils de silicium

Résumé : La recherche sur le photovoltaïque vise à réduire le prix par watt de puissance électrique générée. Des efforts considérables sont menés pour rechercher de nouveaux matériaux et des conceptions qui repoussent les limites des cellules solaires existantes. Le développement récent de matériaux et nanostructures complexes pour les cellules solaires nécessite des efforts plus importants pour mener à bien leur caractérisation et leur modélisation. Cette thèse porte sur la caractérisation optique, la modélisation et l'optimisation de la conception d'architectures de cellules solaires de pointe.
Premièrement, nous nous sommes concentrés sur l'étude optique de diverses surfaces pyramidales et de leur impact sur les performances des cellules silicium à hétérojonction. Nous avons constaté que les angles au sommet des pyramides, préparées à l'aide de différentes conditions de texturation, diffèrent de la valeur théorique de $70.52°$ attendue pour le silicium cristallin. Cette modification de l'angle au sommet est expliquée par la présence, sur les facettes pyramidales, de terrasses monoatomiques régulières, observées par microscopie électronique à transmission de résolution atomique. L'impact d'une variation de l'angle au sommet sur les épaisseurs des couches minces déposées est étudié et les conséquences sur l'efficacité des cellules solaires résultantes sont discutées. Un modèle optique développé pour le calcul de la réflectance et de l'absorption des couches minces en multicouches sur surfaces pyramidales a permis l'optimisation de la conception de la cellule solaire pour un angle au sommet pyramidal donné.
L'ellipsométrie matricielle Mueller a été utilisée in-situ pour caractéiser le processus de croissance - par méthode vapeur-liquide-solide activée par plasma - des nanofils de silicium. Nous avons développé un modèle optique facile à utiliser, qui, à notre connaissance, est le premier modèle utilisant des données ellipsométriques expérimentales pour contrôler le procédé de croissance, en phase vapeur-liquide-solide assisté par plasma, des nanofils. La dépendance linéaire observée du dépôt de matériau de silicium avec le temps de dépôt nous permet de suivre le processus de fabrication in situ et de contrôler la qualité du matériau.

Title : Modeling and characterization of materials and nanostructures for photovoltaic applications

Keywords : spectroscopic ellipsometry, in-situ Mueller matrix polarimetry, multi-layer optical models, solar cells, pyramidal texture, silicon nanowires

Abstract : Research in photovoltaics aims at lowering the price per watt of generated electrical power. Substantial efforts aim at searching for new materials and designs which can push the limits of existing solar cells. The recent development of complex materials and nanostructures for solar cells requires more effort to be put into their characterization and modeling. This thesis focuses on optical characterization, modeling, and design optimization of advanced solar cell architectures.
At first, we focused on the optical study of various pyramidal surfaces and their impact on the silicon heterojunction solar cell performance. We have found that vertex angles of pyramids prepared using various texturing conditions vary from the theoretical value of $70.52°$ expected from crystalline silicon. This change of the vertex angle is explained by regular monoatomic terraces, which are present on pyramid facets and are observed by atomic resolution transmission electron microscopy. The impact of a vertex angle variation on the thicknesses of deposited thin films is studied and the consequences for resulting solar cell efficiency are discussed. A developed optical model for calculation of the reflectance and absorptance of thin film multi-layers on pyramidal surfaces enabled a solar cell design optimization, with respect to a given pyramid vertex angle.
In-situ Mueller matrix ellipsometry has been applied for monitoring the silicon nanowire growth process by plasma-enhanced vapor-liquid-solid method. We have developed an easy-to-use optical model, which is to our knowledge a first model fitting the experimental ellipsometric data for process control of plasma-assisted vapor-liquid-solid grown nanowires. The observed linear dependence of the silicon material deposition on the deposition time enables us to trace the fabrication process in-situ and to control material quality.

Université Paris-Saclay
Espace Technologique / Immeuble Discovery
Route de l'Orme aux Merisiers RD 128 / 91190 Saint-Aubin, France